

UC Riverside

UC Riverside Electronic Theses and Dissertations

Title

Electrospun Nanofibers for Applications in Energy Harvesting and Generation

Permalink

<https://escholarship.org/uc/item/01h168q7>

Author

Yu, Sooyoun

Publication Date

2020

Peer reviewed|Thesis/dissertation

UNIVERSITY OF CALIFORNIA
RIVERSIDE

Electrospun Nanofibers for Applications in Energy Harvesting and Generation

A Dissertation submitted in partial satisfaction
of the requirements for the degree of

Doctor of Philosophy

in

Chemical and Environmental Engineering

by

Sooyoun Yu

September 2020

Dissertation Committee:

Dr. Nosang Vincent Myung, Chairperson

Dr. Juchen Guo

Dr. Ian Wheeldon

Copyright by
Sooyoun Yu
2020

The Dissertation of Sooyoun Yu is approved:

Committee Chairperson

University of California, Riverside

ACKNOWLEDGEMENTS

I would like to dedicate this great honor to a handful of people. First and foremost, I give my greatest gratitude to my principal investigator, Professor Nosang Vincent Myung. He has been my rock, my teacher, my mentor, my friend. Throughout these years, he has been one of the most consistent aspects of my life, during which I had my fair share of struggles and stressful days. My five years at UC Riverside would not have been so fruitful and nothing short of a blessing had it not been for his guidance and support. He truly lives up to his “nickname” of my academic father. I am so grateful to have him on my side and excited that I still have more to learn from him.

Secondly, my family. My parents, who live in South Korea, have more than made up for the physical distance that keeps us apart; their unconditional love, support, and faith in me, their countless prayers, advice, virtual hugs and kisses I received made me more confident in myself. My “American parents”, Minah and Youngho. All of the memories we shared over the years not only helped me through some difficult times, but also will be some of my most cherished memories of my life in California. My beloved husband, Riki, who has always been there for me, through thick and thin, long or short straw – you showed me time and again I can and should be proud of myself. I love you and would not trade you for anything in the world – not even if I were to get a freebie Ph.D. And finally, Yuri – the pure bundle of joy who decided to come to me and Riki during what seemed like the darkest time of 2020. You kept me company and helped me in ways that you didn’t even know, and your father and I cannot wait to greet you into the world.

Last, but of course not least, all of my friends and colleagues who have cheered me on, supported me in their own unique ways, parted their wisdom, shared their struggles, lifted me up and pushed me forward. I thank all of you.

Of course, my work would not have been possible without:

- Previously published works

Yu, S. & Myung, N. V. Minimizing the Diameter of Electrospun Polyacrylonitrile (PAN) Nanofibers by Design of Experiments for Electrochemical Application. *Electroanalysis* **30**, (2018)

Chen, Q., Yu, S., Myung, N. & Chen, W. DNA-guided assembly of a five-component enzyme cascade for enhanced conversion of cellulose to gluconic acid and H₂O₂. *J. Biotechnol.* **263**, 30–35 (2017)

- Funding from National Science Foundation (Award number 1263818)

- Access to the field-emission scanning electron microscope (ThermoFisher Scientific NNS450) granted by the Central Facility for Advanced Microscopy and Microanalysis at University of California, Riverside

ABSTRACT OF THE DISSERTATION

Electrospun Nanofibers for Applications in Energy Harvesting and Generation

by

Sooyoun Yu

Doctor of Philosophy, Chemical and Environmental Engineering
University of California, Riverside, September 2020
Dr. Nosang Vincent Myung, Chairperson

Electrospun nanofibers have gained great research interest for decades as attractive nanomaterial for various applications due to their ultra-high specific surface area, flexibility in materials, and ease of fabrication. Furthermore, fine tuning of electrospinning or post-electrospinning process conditions can allow for precise control of morphology, composition, physical, electrical, and electrochemical properties to tailor the nanofibers for a specific application. In this work, the effect of various electrospinning-related conditions on properties of polyacrylonitrile (PAN)-derived nanofibers was elucidated by series of systematic variation of parameters called design of experiment (DOE). Analyses on the DOE revealed solution viscosity, mainly controlled by polymer concentration, was the predominant factor for nanofiber morphology, while the addition of composite materials such as multi-walled carbon nanotubes and zinc acetate also strongly affected the nanofiber dimensions.

To study the suitability of the PAN nanofibers with controlled properties for applications in energy harvesting and generation, piezoelectric and electrochemical properties of PAN-derived as-spun and heat-treated nanofibers were characterized. For the first time, size-dependent piezoelectric properties for PAN nanofibers was carefully investigated, which showed the voltage generated perpendicular to the direction of the fiber (V_{33}) increased as a function of decreasing fiber dimensions, similar to more commonly studied piezoelectric polymers. Electroanalytical methods such as cyclic voltammetry, linear polarization and electrochemical impedance spectroscopy were employed to investigate the feasibility of various carbonaceous nanofibers as electrode material.

Enzymatic fuel cell was chosen as the device of interest for energy generation application in this work. In an attempt to utilize the naturally abundant yet complex cellulose as fuel, a multienzyme cascade complex in nature called cellulosome was biomimetically fabricated by site-specific immobilization of 5 enzymes on customized DNA scaffold for sequential hydrolysis of cellulose followed by catalytic oxidation of glucose for electricity generation. With successful demonstration of the synergistic effect of enzyme immobilization on DNA scaffold, similar system was functionalized onto an electrode for preliminary electrochemical studies, which exhibited great promise as multienzyme cascade-based bioanode for cellulolytic fuel cell.

TABLE OF CONTENTS

Chapter 1: Recent Advances in the Direct Electron Transfer-Enabled Enzymatic Fuel Cells.....	1
1.1 Abstract	1
1.2 Introduction	1
1.3 Biocatalyst engineering	4
1.3.1 Mutated enzymes.....	4
1.3.2 Orientation of enzymes.....	8
1.4 Biocatalyst immobilization methods.....	10
1.4.1 Physisorption	12
1.4.2 Entrapment and conducting polymers	13
1.4.3 DNA as scaffolds or electron acceptors	15
1.5 Nanomaterial-based electrodes.....	17
1.5.1 Carbonaceous materials	17
1.5.2 Porous nanostructure	18
1.5.3 Gold nanoparticles	20
1.6 Recent progress in biomedical application of DET-enabled EFC	22
1.7 Conclusions and outlook	25
1.8 References	26
Chapter 2: Electrospun Polyacrylonitrile-Derived Nanofibers and Their Controlled Physical, Piezoelectric, and Electrochemical Properties via Design of Experiment..	38
2.1 Abstract	38
2.2 Introduction	39
2.2.1 Electrospun nanofibers	39
2.2.2 Piezoelectric energy harvesting.....	43
2.2.3 Nanofibers for fuel cells	53
2.3 Materials and Methods	55
2.4 Results and Discussion.....	63
2.4.1 PAN nanofibers	63
2.4.2 PAN/MWNT nanofibers	86

2.4.3 PAN/MWNT/ZnAC nanofibers	100
2.5 Conclusion.....	114
2.6 References	116
Chapter 3: DNA-Guided Assembly of a Five-Component Enzyme Cascade for Enhanced Conversion of Cellulose to Gluconic Acid and Hydrogen Peroxide.....	128
3.1 Abstract	128
3.2 Introduction	129
3.3 Materials and Methods	132
3.3.1 Protein expression and conjugation with DNA linkers	132
3.3.2 Proteins assembly onto the DNA template	134
3.3.3 Measurements of enzyme activities	134
3.4 Results and Discussion.....	135
3.4.1 Protein conjugation with DNA linkers	135
3.4.2 Enhanced H ₂ O ₂ production by assembled BglA and GOx	138
3.4.3 Conversion of cellulose to H ₂ O ₂ by the five-enzyme assembly	139
3.5 Conclusion.....	141
3.6 References	143
Chapter 4: Development of Bienzymatic Electrode as Concept Demonstration for Cellulolytic Anode with Multienzyme Cascade on DNA Scaffold.....	147
4.1 Abstract	147
4.2 Introduction	148
4.3 Materials and Methods	150
4.4 Results and Discussion.....	154
4.4.1 Design of experiment (DOE) for enzymatic electrode fabrication	154
4.4.2 Bienzymatic system on DNA scaffold	162
4.5 Conclusion.....	170
4.6 References	172
Chapter 5: Summary and Perspective	174

LIST OF FIGURES

Figure 1.1 Schematic of (a) direct and (b) mediated electron transfer in enzymatic electrodes.....	2
Figure 1.2 Schematic of possible DET route between FAD-GDH and individual SWNT...7	7
Figure 1.3 Schematic representing direct bioelectrocatalysis of pyrene-modified laccase immobilized by β -cyclodextrin-modified gold nanoparticles bound to carbon nanotube....9	9
Figure 1.4 Schematic of proposed route of DET for GOx physisorbed with multi-walled carbon nanotubes.....	13
Figure 1.5 Schematic of (a) fabrication of various GOx-functionalized electrodes and their mechanism of immobilization; (b) comparison between native GOx and GOx/PCA composite.....	14
Figure 1.6 Schematic of five-enzyme cascade system for hydrolysis of cellulose and glucose oxidation.....	16
Figure 1.7 Schematics showing (A) curvature effect (B) edge effect (C) electrostatic effect that are taken into account for meso- and microporous structures.....	19
Figure 1.8 Schematic of enzymatic fuel cell using live snail. Figures are from work by Halámková et al.....	23
Figure 1.9 (a-c) Optical images of enzymatic fuel cell based on transparent and flexible electrodes. (d) Schematic of membrane- and mediator-free glucose/oxygen biofuel cell...24	24
Figure 2.1 Schematic illustration of a typical electrospinning process.....	42
Figure 2.2 Schematic illustration of molecular structure of (a) α (b) β and (c) γ phase of poly(vinylidene fluoride).....	44
Figure 2.3 SEM images of electrospun PAN nanofibers from solutions in Table 2.3.....	64
Figure 2.4 DOE analysis of (a) viscosity (b) surface tension (c) electrical conductivity as a function of various solution conditions.....	65
Figure 2.5 DOE analysis of (a) average fiber diameter and (b) bead density as a function of various solution parameters laid out in Table 2.3.....	66
Figure 2.6 SEM images of electrospun PAN nanofibers from solutions shown in Table 2.4.....	68
Figure 2.7 DOE analysis of (a) average fiber diameter and (b) bead density as a function of electrospinning conditions laid out in Table 2.4.....	68

Figure 2.8 Images of PAN solution droplets under varying applied voltage. Inset: SEM image of nanofiber electrospun under the following applied voltage: (a) 5 kV; (b) 15 kV; (c) 25 kV.....	69
Figure 2.9 SEM images of electrospun PAN nanofibers from solutions shown in Table 2.5. DOE code (a) ++ (b) +- (c) -+ (d) --.....	70
Figure 2.10 DOE analysis of (a) average fiber diameter and (b) bead density as a function of environmental conditions laid out in Table 2.5.....	71
Figure 2.11 BET surface area as a function of average fiber diameter.....	72
Figure 2.12 Electrical conductivity adjusted with nanofiber mat porosity as a function of average fiber diameter.....	73
Figure 2.13 Cyclic voltammogram of carbonized nanofiber-based WE in pH 7.4 PBS at various scan rates. Average fiber diameter was 126 nm.....	75
Figure 2.14 Electrochemical impedance spectra of carbonized nanofiber-based WE in pH 7.4 PBS.....	77
Figure 2.15 Gravimetric double-layer capacitance of carbonized nanofiber mats as a function of their fiber diameter.....	78
Figure 2.16 SEM images of (a) 3.25 wt.% (b) 4 wt.% (c) 6 wt.% (d) 8 wt.% (e) 10 wt.% PAN nanofibers electrospun at 2000 RPM.....	80
Figure 2.17 V_{33} of as-spun PAN nanofibers with various diameters. All measurements were taken at room temperature.....	81
Figure 2.18. Effect of annealing temperature on (a) V_{33} and (b) d_{33} of PAN-derived nanofibers of various sizes.....	82
Figure 2.19 FT-IR spectra of as-spun and annealed (cyclized) PAN-derived nanofibers. Cyclization was conducted at 280 °C.....	84
Figure 2.20. (a) V_{13} of as-spun PAN nanofibers with various diameters. (b) Effect of annealing temperature on V_{13} of PAN-derived nanofibers of various sizes.....	86
Figure 2.21. DOE analyses of (a) viscosity; (b) surface tension; and (c) solution electrical conductivity as a function of DOE factors laid out in Table 2.8.....	88
Figure 2.22. DOE analyses of (a) average nanofiber diameter; (b) bead density; and (c) fiber fraction as a function of DOE factors laid out in Table 2.8.....	89

Figure 2.23. (a) 3D scatter plot and (b) contour plot of average diameter of PAN/MWNT nanofibers as a function of PAN wt.% and MWNT-to-PAN ratio by wt.% (c) 3D scatter plot and (d) contour plot of average diameter of PAN/MWNT nanofibers as a function of solution viscosity and electrical conductivity.....	90
Figure 2.24 Effect of annealing temperature on V_{33} of PAN- and PAN/MWNT-derived nanofibers of various sizes.....	91
Figure 2.25 Effect of annealing temperature on V_{13} of PAN- and PAN/MWNT-derived nanofibers of various sizes.....	92
Figure 2.26 Electrical conductivity of carbonized PAN- and PAN/MWNT-derived nanofibers as a function of nanofiber diameter and MWNT-to-PAN ratio by wt.%.....	94
Figure 2.27 Cyclic voltammogram of working electrodes based on carbonized PAN- and PAN/MWNT-derived nanofibers of various MWNT loading. CV was conducted at room temperature.....	96
Figure 2.28 (a) Nyquist (b) Bode magnitude (c) Bode phase plots of MWNT-embedded CNF mat electrodes in deaerated PBS, pH7.4, at room temperature.....	97
Figure 2.29 DOE analyses of (a) viscosity; (b) surface tension; and (c) solution electrical conductivity as a function of DOE factors laid out in Table 2.11.....	101
Figure 2.30 DOE analyses of (a) average nanofiber diameter; (b) bead density; and (c) fiber fraction as a function of DOE factors laid out in Table 2.8.....	102
Figure 2.31. DOE analysis of solution properties of PAN/MWNT/ZnAc: (a) viscosity (b) surface tension (c) electrical conductivity as a function of DOE factors.....	104
Figure 2.32 DOE analysis of nanofiber properties of PAN/MWNT/ZnAc: (a) nanofiber diameter (b) bead density (c) fiber fraction as a function of DOE factors.....	105
Figure 2.33. SEM images of 8 wt.% PAN, 3.33 wt.% MWNT, 0.67 wt.% ZnAc, 0.1 wt.% BYK nanofibers at various processing steps. (a) as-spun; (b) one-step stabilized; (c) two-step stabilized; (d) carbonized after one-step stabilization; (e) carbonized after two-step stabilization; (f) acid treated in 20 vol.% HCl in DI water for 60 s.....	107
Figure 2.34. EDS mapping for Zn in PAN/MWNT/ZnAc-derived nanofibers at the following processing steps: (a) as-spun; (b) one-step stabilized; (c) carbonized after one-step stabilization; (d) carbonized after two-step stabilization; (e) acid treated after step (c); and (f) acid treated after step (d).....	108
Figure 2.35. Cyclic voltammetry at 200, 150, 100, 50, 25, 10, 1 mV/s for PAN/MWNT/ZnAc-derived porous C/MWNT nanofibers with DOE code (a) ++ (b) +- (c) 00 (d) -+ (e) - in pH7.4 PBS at room temperature.....	109

Figure 2.36 Tafel plots of carbonized PAN/MWNT/ZnAc-derived nanofiber mat electrodes in deaerated PBS, pH7.4, at room temperature.....	110
Figure 2.37 (a) Nyquist plot and (b,c) Bode plots of porous C/MWNT nanofibers derived from PAN/MWNT/ZnAc nanofibers.....	112
Figure 2.38 DOE analyses of (a) R_1 and (b) R_2 as a function of DOE factors for tri-composite nanofibers. R_1 and R_2 refer to the parameters calculated from EIS fitting.....	114
Figure 3.1 Schematic of a DNA-guided five-enzyme cascade for direct conversion of cellulose to gluconic acid and H_2O_2	131
Figure 3.2 Protein conjugation with DNA linkers. (a) Conjugation of a DNA linker onto each cellulosomal component using the N-terminus HaloTag. (b) Expression and purification of each cellulosomal component. CL: cell lysate, P: purified protein. (c) Confirmation of DNA conjugation onto the cellulosomal components by 10% SDS-PAGE. Presence of a slower mobility band confirmed the successful conjugation. (d) Conjugation of a DNA linker to GOx using the well-known EDC chemistry. (e) Confirmation of GOx conjugation with a DNA linker by 10% native acrylamide gel.....	136
Figure 3.3 (a) Production of gluconic acid and H_2O_2 by BglA and GOx. (b) Confirmation of BglA and GOx assembly on agarose gel. (c) H_2O_2 production for either assembled or unassembled BglA and GOx. (d) The rate of H_2O_2 production for either assembled or unassembled BglA and GOx.....	137
Figure 3.4 Effect of temperature (a) and pH (b) on glucose production by either unassembled (blue) or assembled (red) CelA, CBM, CelE and BglA.....	139
Figure 3.5 Enhanced H_2O_2 production from cellulose using an assembled five-enzyme cascade. (A) Confirmation of five-enzyme assembly by agarose gel. (B) Comparison of H_2O_2 production using either the assembled or unassembled five-enzyme system.....	141
Figure 4.1 Cyclic voltammogram of electrode before and after modification with GOx and MWNT.....	155
Figure 4.2 Scan rate-dependent cyclic voltammogram of electrode modified with GOx and MWNT.....	157
Figure 4.3 Cyclic voltammogram of electrode modified with GOx and MWNT in deaerated and aerated PBS, pH7.4.....	158
Figure 4.4 DOE analysis of (a) cathodic peak current density and (b) slope of i_{pc} vs. $v^{1/2}$ curve as a function of DOE1 factors.....	160
Figure 4.5 (a) Cyclic voltammogram of electrodes fabricated according to DOE2 (shown in inset table). CV was conducted in deaerated PBS, pH7.4, at 50 mV/s. (b) DOE analysis of cathodic peak height.....	161

Figure 4.6 Cyclic voltammogram of electrodes with one or two enzymes immobilized by either physisorption or DNA conjugation.....	164
Figure 4.7 Cyclic voltammogram of electrode with GOx-BglA system immobilized by DNA conjugation in deaerated and aerated PBS, pH7.4.....	165
Figure 4.8 [Cellobiose]-dependent cyclic voltammogram of electrode with GOx-BglA system immobilized by DNA conjugation. DNA-immobilized enzyme cascade was anchored down onto the electrode with (a) 10-nm and (b) 100-nm gold nanoparticles. CV was conducted in aerated PBS, pH7.4, with scan rate of 50 mV/s. Arrows indicate increasing cellobiose concentration. (c) Change in cathodic current at E=-0.7 V as a function of glucose concentration.....	167
Figure 4.9 (a) Time-dependent absorbance and (b) specific production rate of GOx-BglA system immobilized by DNA conjugation over time.....	169
Figure 4.10 Cyclic voltammogram of electrode with GOx-BglA system immobilized by DNA conjugation over time. DNA-immobilized enzyme cascade was anchored down onto the electrode with (a) 10-nm and (b) 100-nm gold nanoparticles.....	170

LIST OF TABLES

Table 1.1 Overview of enzyme immobilization methods.....	11
Table 2.1 Overview of synthesis methods for nanofibers.....	40
Table 2.2. Overview of piezoelectric materials.....	47
Table 2.3 Design of experiment varying solution parameters and their effects on solution and fiber properties.....	63
Table 2.4 Design of experiment varying electrospinning conditions and their effects on fiber properties.....	67
Table 2.5 Design of experiment varying environmental conditions and their effects on fiber properties.....	70
Table 2.6 Solution and nanofiber properties of various electrospun samples.....	79
Table 2.7 Peak assignment from FT-IR for as-spun and stabilized PAN-derived nanofibers.....	85
Table 2.8. Solution and nanofiber properties of various PAN/MWNT samples.....	86
Table 2.9. SEM images of PAN/MWNT/BYK nanofibers fabricated according to DOE.....	87
Table 2.10 Parameters calculated from various electroanalytical methods for PAN- and PAN/MWNT-derived carbon nanofiber mat electrodes.....	98
Table 2.11. Solution and nanofiber properties of various PAN/ZnAc samples.....	101
Table 2.12. SEM images of PAN/ZnAc/BYK nanofibers fabricated according to DOE conditions laid out in Table 2.11.....	102
Table 2.13. Solution and nanofiber properties of various PAN/MWNT/ZnAc samples.....	103
Table 2.14 Parameters calculated from Tafel plots of carbonized PAN/MWNT/ZnAc-derived nanofiber mat electrodes.....	111
Table 2.15 Parameters calculated from various electroanalytical methods conducted with porous C/MWNT nanofiber mat electrodes derived from PAN/MWNT/ZnAc nanofibers.....	113
Table 3.1 List of DNA sequences used in this study.....	134
Table 4.1 Sequence of DNA template and linkers used.....	153

Table 4.2 Summary of resulting parameters from cyclic voltammetry using working electrodes fabricated with conditions laid out by design of experiment 1 (DOE1).....159

1 Recent Advances in the Direct Electron Transfer-Enabled Enzymatic Fuel Cells

1.1 Abstract

Direct electron transfer (DET), which requires no mediator to shuttle electrons from enzyme active site to the electrode surface, minimizes complexity caused by the mediator and can further enable miniaturization for biocompatible and implantable devices. However, because the redox cofactors are typically deeply embedded in the protein matrix of the enzymes, electrons generated from oxidation reaction cannot easily transfer to the electrode surface. In this review, methods to improve the DET rate for enhancement of enzymatic fuel cell performances are summarized, with a focus on the more recent works (past 10 years). Finally, progress on the application of DET-enabled EFC to some biomedical and implantable devices are reported.

1.2 Introduction

Since its first demonstration of concept by Yahiro et al.,¹ enzymatic fuel cell (EFC) has gained much research interest as one of the environmentally friendly and renewable source of power generation. Utilizing isolated enzymes from microorganisms as biocatalysts at either or both of electrodes, the substrate specificity of the biocatalysts essentially removes the need for compartmentalization of each electrode, allowing for wider applications via miniaturization. EFC is known to generate electricity via two electron transport mechanisms: direct electron transfer (DET) and mediated electron

transfer (MET). (Figure 1.1) When an electron generated from oxidation catalyzed by the redox center of a bioanodic enzyme travels directly to the electrode surface and is collected as current, the enzyme is known to undergo DET; when an additional component is utilized between the enzymatic catalyst and electrode surface to act as a mediator to shuttle the electron, it is referred to as MET. Early works with EFC typically involved electron mediators, such as hydroquinone, benzoquinone, and ferricyanide salt to obtain current.^{2,3} Though first report of DET may date back to as early as 1972,⁴ it was not until 1978 when works by Berezin et al. pioneered the DET mechanism to collect current with a laccase (Lc) directly adsorbed onto graphite electrodes.⁵

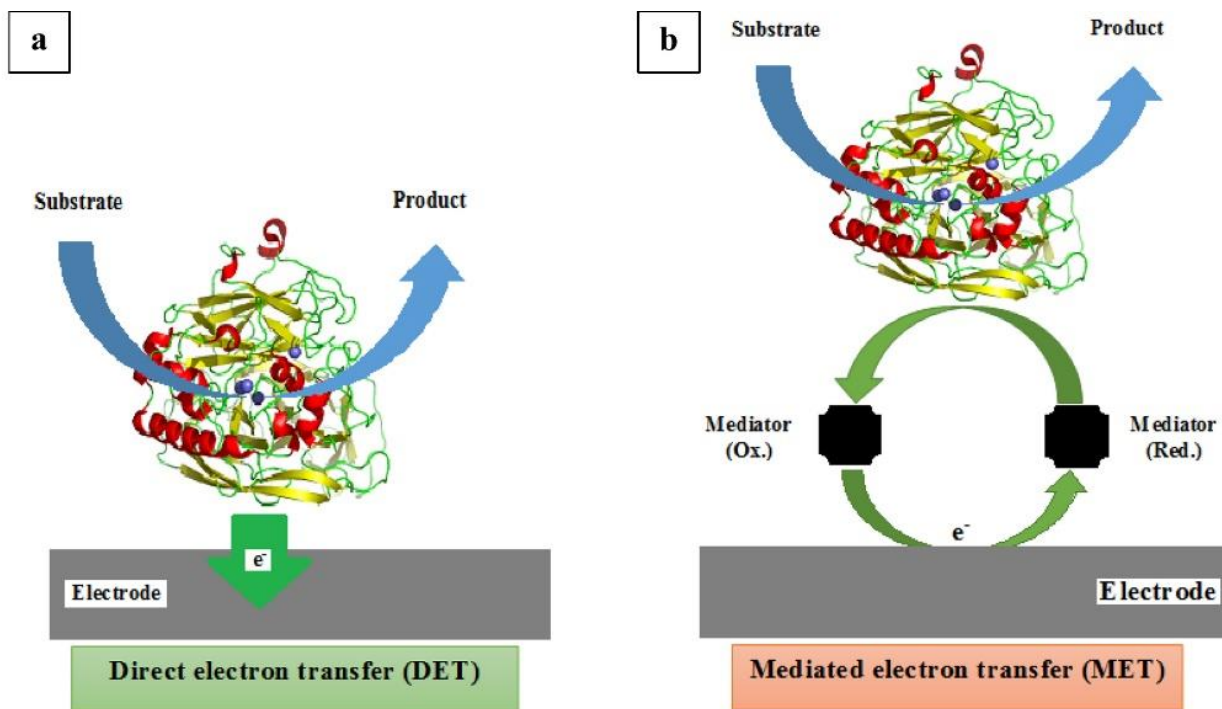


Figure 1.1 Schematic of (a) direct and (b) mediated electron transfer in enzymatic electrodes.⁶

Despite over a half of a century worth of research, there is yet to be a consensus on whether DET or MET surpasses one another in terms of EFC performance. On one hand,

MET-enabled EFC theoretically provides higher current and power density as the mediator would minimize the number of electrons that fail to reach the electrode due to its small tunneling distance ($\sim 10\text{-}20 \text{ \AA}$); on the other hand, DET-enabled EFC offers simpler configuration and can bypass potential toxicity or low stability of some mediators.^{7,8} Furthermore, not using a mediator means the redox enzymes can operate at a potential close to their natural standard redox potentials, leading to lower chances of interfering reactions as well as higher open-circuit potential and thus higher power density.⁹

When evaluating the performance of EFC, several properties are commonly characterized or quantified: power density, current density, the amount of decay in power density over time, and open-circuit potential (OCP). The power and current density and the OCP correlate to the overall power output by the EFC, while the time-dependent decay of the power density can be translated into the stability of the EFC. While DET seems like a more favorable method of electron transfer to optimize the EFC performance, the small electron tunneling distance greatly limits the type of oxidoreductases that can be used for this configuration. Typically, the redox center is deeply embedded within a protein matrix, the size of which often exceeds 10 \AA . In fact, only about a 100 of 1700 known oxidoreductase enzymes can facilitate DET.¹⁰ In an effort to not only increase this number but also enhance the fuel cell performance utilizing DET, a number of components of EFC could be improved: protein engineering to increase the efficiency of the direct electron transfer; immobilization of the biocatalysts on the electrode to decrease the tunneling distance and enhance the stability; and use of functional nanomaterials as electrodes to

maximize enzyme loading while minimizing IR drop and tunneling distance for efficient charge transfer.

Herein, methods to enhance the performance of DET-enabled EFC that have recently been popular are summarized, and the outlook on these EFCs, including their applications, are presented.

1.3 Biocatalyst engineering

One of the major drawbacks of using native enzymes as biocatalysts for EFCs is that some redox cofactors, molecules that change their oxidation state during catalytic redox reaction of the substrate, are deeply embedded inside the enzyme, and thus it is difficult for the electrons generated from the oxidation reaction to transfer successfully to the electrode surface. For many enzymes, this means the electrons must be able to travel far beyond their 10-Å limit to reach the electrode, and most, if not all, of the electrons are not collected as current without any modification on the enzymes.

1.3.1 Mutated enzymes

Glucose oxidase (GOx), one of the most extensively studied oxidoreductase enzyme for catalysis of glucose oxidation, is well known for its flavin adenine dinucleotide (FAD) cofactor embedded within the protein matrix as far as 15-26 Å from the surface.¹¹ Due to the large depth in which the FAD is located, some works have claimed that native GOx does not undergo DET at all.^{12,13} In these works, the redox peaks at $E^0 = -0.46$ V (vs. Ag/AgCl) famously known to represent the GOx activity by the redox of FAD/FADH₂

cofactor were argued to be inaccurate, as their electroanalytical methods with various control experiments suggested the redox peaks were due to the enzymatic activity of the FAD cofactors that have denatured from GOx itself, rather than the electroactivity.

Despite these claims, efforts towards DET-enabled GOx-based EFC have continued. Furthermore, other enzyme catalysts for both anode and cathode have been engineered and utilized for enhancement of EFC performance. This section describes various methods to modify or engineer enzymes for increasing the stability of enzyme immobilization and decreasing enzyme-to-electrode distance, thereby increasing the chance of DET for higher power density.

Use of native GOx as the anodic enzyme often leads to its sensitivity to oxygen. In addition to its primary substrate, glucose, GOx also interacts with oxygen as a natural electron acceptor and catalyzes its reduction to hydrogen peroxide. This can result in not only a lower coulombic efficiency, but also affecting the cathode by depleting the available oxygen to be reduced.¹⁴

As one of the alternatives, FAD-dependent glucose dehydrogenase (referred to as GAD-GDH) has been suggested as a promising enzyme. GDH is available with three different cofactors – pyrroloquinoline quinone (PQQ), nicotinic adenine dinucleotide (NAD), and FAD. Though GDH based on all three cofactors have been utilized as anodic enzyme catalyst for EFC applications,¹⁵⁻¹⁷ the low substrate selectivity and poor thermal stability of PQQ-dependent GDH¹⁸ and denaturing of NAD cofactor suggest there are room for improvement for them to be stronger candidates for glucose-oxidizing enzyme for

EFCs. FAD-GDH, on the other hand, have been steadily used as an oxygen-insensitive alternative, immobilized in various EFC setups. Desriani et al. demonstrated FAD-GDH-based enzymatic fuel cell by casting FAD-GDH/carbon ink mixture on carbon cloth to fabricate the bioanode.¹⁹ Combined with the cathode functionalized with bilirubin oxidase (BOD), the EFC produced up to $9.3 \mu\text{W}/\text{cm}^2$ power density with cellobiose as substrate. Muguruma et al. employed debundled single-walled carbon nanotubes (SWNTs), which were small enough in diameter (1.2 nm) to be plugged into the grooves of FAD-GDH to minimize the distance between enzyme cofactor and the electrode. Glucose concentration-dependent current response was only observed when debundled SWNTs were utilized as opposed to SWNT aggregates or multi-walled carbon nanotubes (MWNTs), despite the oxygen insensitivity of FAD-GDH.²⁰ Lee et al. studied the electrochemical behavior of FAD-GDH via chronoamperometry. Not only was DET achieved with the mutated enzyme, but also the distance between enzyme cofactor and electrode surface was controlled by different self-assembly monolayers (SAM) to show its significance in enhancing the current response.²¹ Furthermore, the chemisorption between the thiol residue of SAM and gold electrode, combined with the covalent bond between the amino groups of the FAD-GDH and succinimide groups of SAM, strengthened the stability of enzyme immobilization on the electrode surface for more efficient DET.

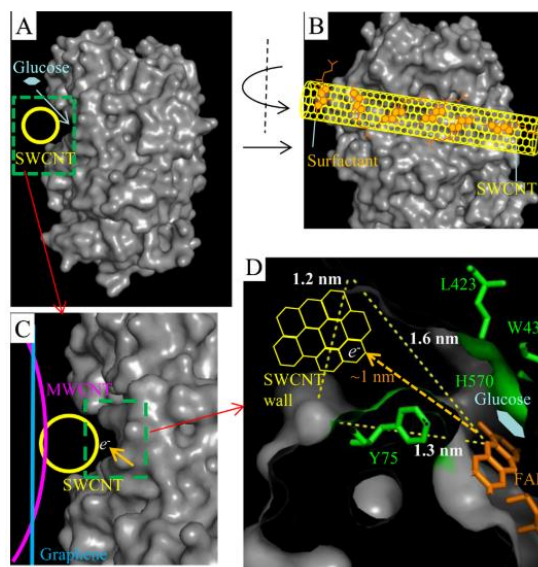


Figure 1.2 Schematic of possible DET route between FAD-GDH and individual SWNT. Between SWNT, MWNT, and graphene, debundled SWNT is the only one small enough to fit into the indentations of FAD-GDH, reducing the distance for electrons to travel from the FAD cofactor.²⁰

Another method to overcome the weak DET rate by GOx is genetic modification for ready functionalization with metallic nanomaterials or more intricate structure with supporting materials. PrévotEAU *et al.* demonstrated that deglycosylated glucose oxidase exhibited more negative surface charge than native GOx, which allowed for stronger electrostatic interaction with positively charged hydrogels used to immobilize the enzymes.²² Electrodes functionalized with deglycosylated GOx showed higher current density to fixed amount of glucose than native GOx, which was attributed to the smaller enzyme-electrode distance and higher enzyme loading due to stronger attraction towards the hydrogel and thus the electrode surface. Holland *et al.* made direct mutations at various locations of GOx to add a cysteine side chain, which revealed a thiol group at a distance from 14 to 29 Å from the FAD cofactor. The thiol group attached to the GOx readily bound to gold nanoparticles, which facilitated direct electron transfer when functionalized onto

electrode surface.²³ Electroanalytical methods on electrodes modified with 5 mutated GOx showed only the enzyme with the thiol group closest to the FAD exhibited electroactivity, reinforcing the significance of minimizing enzyme-to-electrode distance for efficient DET. Other enzymatic catalysts such as fructose dehydrogenase,^{24,25} laccase,²⁶ and pyranose 2-oxidase²⁷ have been modified for more stable immobilization as well as enhanced enzymatic activity.

1.3.2 Orientation of enzymes

Oxidoreductase enzymes are relatively large and measure few nanometers in diameter; the redox center is typically embedded within the protein matrix, at times tens of angstroms from the surface of the enzyme, which is well over the maximum electron tunneling distance of up to 20 Å.²⁸ Because of this, it is essential to achieve favorable orientation of the enzyme when immobilizing on the electrode; that is, in a way that the redox cofactor is closest to the electrode surface.²⁹ The difficulties associated with obtaining such orientation, parameters that affect the orientation, and the enzymatic electrode properties that are in turn affected by the enzyme orientation are reviewed in great detail by Hitaishi *et al.*³⁰ Thus, in this review, several recent works demonstrating fine tuning of enzyme orientation by protein and electrode engineering to improve the direct electron transfer are covered.

The general idea behind achieving good orientation for DET is to promote electrostatic interaction or covalent binding between the enzyme and the electrode surface so that the cofactor is located at a compatible distance from the electrode for electron

transfer. For example, gold nanoparticles immobilized on highly oriented graphite electrode were functionalized with aminophenyl groups, which allowed for covalent binding between the nanoparticles and laccase enzyme. Two-step immobilization was proposed for this work: (i) the amino groups on the gold nanoparticles reacted with the oxidized sugar residues on the Lc, while (ii) amide bonds were formed between carboxylic groups of the enzyme and amino groups on the graphite electrode.³¹ Lalaoui *et al.* modified a specific location of laccase (Lc) with a pyrene molecule near the T1 copper redox center of the enzyme, so that when the pyrene group on the Lc bound to the CNT-bound gold nanoparticle, the redox center was closest to the electrode surface to maximize the current density output.³²

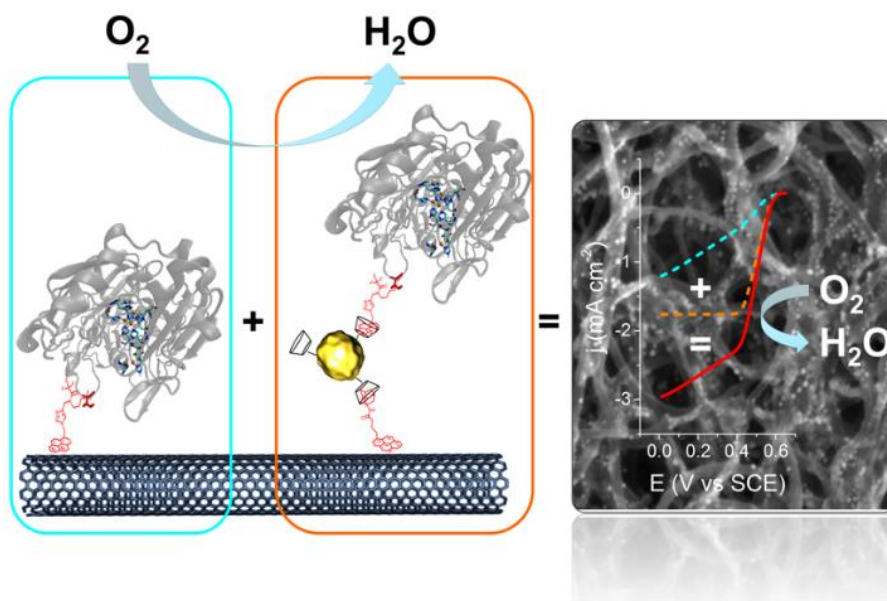


Figure 1.3 Schematic representing direct bioelectrocatalysis of pyrene-modified laccase immobilized by β -cyclodextrin-modified gold nanoparticles bound to carbon nanotube.³²

Ma *et al.* engineered seven different mutants of cellobiose dehydrogenase to vary the orientation at which the enzyme was immobilized on the electrode surface. All enzymes

but the wild type one were covalently bound to either gold or glassy carbon electrode, which was confirmed by surface plasmon resonance and cyclic voltammetry; furthermore, the distance of the cytochrome domain from the electrode greatly affected the DET/MET ratio.³³

1.4 Biocatalyst immobilization methods

Stability of enzymatic fuel cells can also be enhanced by securely immobilizing the catalyst on the electrode surface. Without proper anchoring down or protection, biocatalysts could easily denature and lose their activity or desorb from the electrode surface. Several immobilization methods have been developed and studied, which are summarized in Table 1.1 below. With the ample potential for miniaturization for applications in biomedical, biocompatible, and even implantable devices, it is critical to maximize the stability of the biocatalysts and thus of the device performance.

Table 1.1 Overview of enzyme immobilization methods.

	Mechanism	Reversibility	Advantages	Disadvantages	Ref.	
	Physisorption	Hydrophobic-hydrophilic, van der Waals	Reversible	Low cost, simple	Long time, leaching	34
	Covalent bonding	Functional groups on protein binds to surface	Irreversible	Little leakage, mild conditions	Low loading, enzymes denature	35
	Entrapment	Caging by covalent or non-covalent bonds within gels or fibers	Irreversible	No chemical interaction with enzymes, improved stability	Low loading, enzymes denature	36
	Cross-linking	Intermolecular linkages between enzymes	Irreversible	Higher activity, very little desorption	Potential changes in active sites	37
	Affinity	Utilizes specificity of enzymes under different physiological conditions	Reversible	High retention of activity	High cost	38
≡	DNA conjugation	ssDNA linked to enzymes hybridized to ssDNA template	Irreversible	Site-specific immobilization to organize multiple enzymes, very little desorption	Long time, high cost	39

1.4.1 Physisorption

Physisorption, typically done by dropcasting an enzyme solution onto the electrode surface followed by air-drying, is by far the simplest and cheapest method to fabricate enzyme electrodes. However, because the enzymes are immobilized by weak van der Waals forces or hydrophobic-hydrophilic interactions, they can easily desorb or leach off the electrode surface.^{40,41} Because of this, physisorption is often avoided, and rather, novel methods of enzyme immobilization or development of composite electrode materials are sought, and thus physisorption is only briefly described in this review. However, there are still recent efforts to improve the stability of physisorbed enzyme catalysts, including composite materials to co-deposit with the enzyme solution. Das *et al.* utilized composite electrode consisting of reduced graphene oxide (rGO) and gold nanoparticles (AuNPs) to immobilize GOx, which showed higher electron transfer rate than when rGO or AuNPs were used individually. The improved performance of laboratory scale fuel cell built from this bioanode was attributed to the increase specific surface area and electronic conductivity of rGO combined with better attachment between GOx and AuNPs via sulfur-containing amino acids of the enzyme.⁴² Liu *et al.* studied the effect of MWNTs on the DET and electroactivity of GOx by co-depositing carbon nanotubes of various numbers of layers for various electroanalytical methods, which suggested that the electrons generated from GOx was shuttled from outer to inner wall of the MWNTs.⁴³

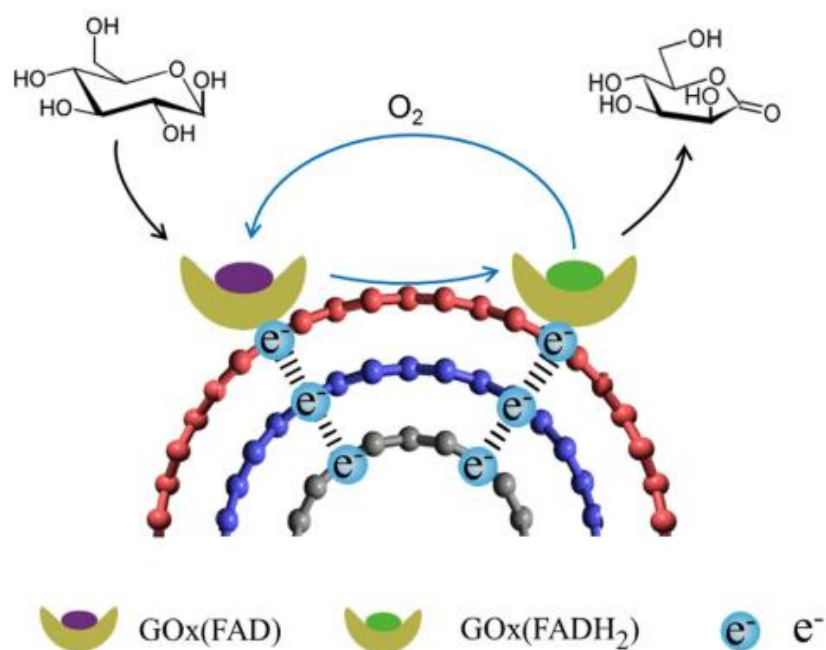


Figure 1.4 Schematic of proposed route of DET for GOx physisorbed with multi-walled carbon nanotubes.⁴³

1.4.2 Entrapment and conducting polymers

Organic molecules with metallic or semiconducting electrical properties called conducting polymers can be an effective agent to entrap the enzyme catalysts and help transfer electrons to the electrodes. In addition to these benefits, polypyrrole (Ppy) helps prevent some undesired reactions, explaining its continued use since its implementation in EFC setups in 1986.⁴⁴ Recently, more complex bioanode setups with single- or multiwalled carbon nanotubes, nanocellulose, graphene, or various Ppy nanostructures, immobilizing a wide range of enzymes such as fructose dehydrogenase,^{45,46} glucose oxidase,⁴⁷⁻⁴⁹ and alcohol dehydrogenase⁵⁰. Many works suggested the enhanced power density was owed to the conductive polymer matrix allowing for proper orientation of the enzymes, good mass transport rates, and improved stability.

Polyethyleneimine (PEI) is also widely used to immobilize enzymes while exhibiting water miscibility and high biocompatibility as well as offering various surface chemistries for stable binding to electrode surfaces or other nanomaterials.^{51–53} PEI is typically used along with carbon nanotubes^{51,54} or metallic nanoparticles^{55–57} to increase the stability of enzyme immobilization.

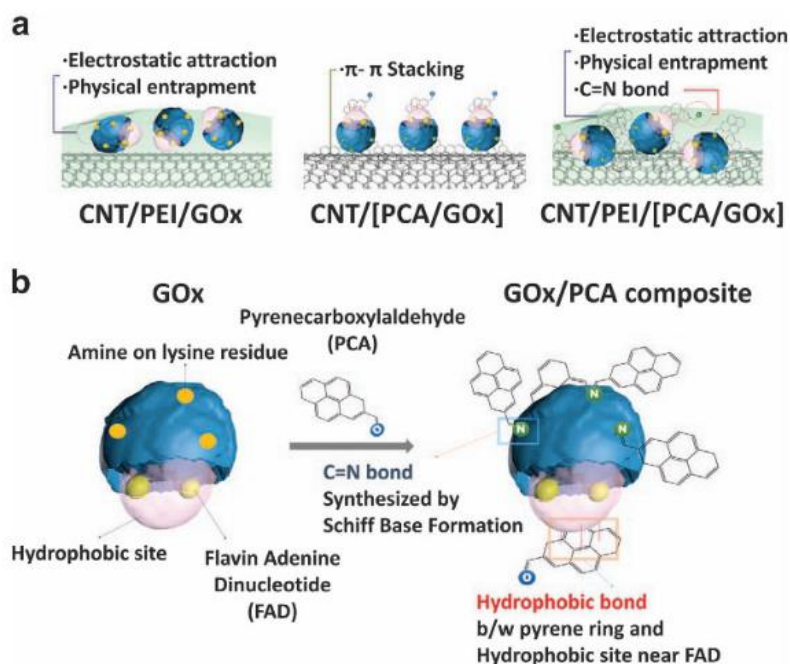


Figure 1.5 Schematic of (a) fabrication of various GOx-functionalized electrodes and their mechanism of immobilization; (b) comparison between native GOx and GOx/PCA composite.⁵¹

Polyaniline (PANI), discovered over 150 years ago, only started gaining research interest until 1980s due to its high electrical conductivity, and was first demonstrated for its utility as enzymatic electrode in 1999 by immobilizing lactate dehydrogenase on electrochemically prepared PANI film.⁵⁸ Since then, PANI has been utilized as composite materials or prepared as nanofibers,^{59–61} mainly due to its multifaceted functionality and

biocompatibility.⁶² PANI can be directly electrochemically polymerized or functionalized onto various carbonaceous nanomaterials including graphene, graphene oxide, or carbon nanotubes for enhanced electrical conductivity and enzymatic activity.^{17,63–65}

1.4.3 DNA as scaffolds or electron acceptors

DNA has been employed as an effective method to immobilize single or multiple enzymes in a specific order for efficient cascade reactions. The terminals of the DNA can be modified for strong covalent bonds onto the electrode surface for stable anchoring of the enzyme catalysts. Xia et al. demonstrated a fully assembled methanol enzymatic fuel cell by immobilizing alcohol dehydrogenase and aldehyde dehydrogenase using zinc-finger protein.⁶⁶ The cascade reaction catalyzed by the two enzyme catalysts successfully hydrolyzed methanol to produce power density of $24.5 \mu\text{W}/\text{cm}^2$. DNA nanostructures have also been used to couple synergistic enzymatic reactions into a cascade system,^{67–69} up to five enzymes for sequential hydrolysis of cellulose.⁷⁰

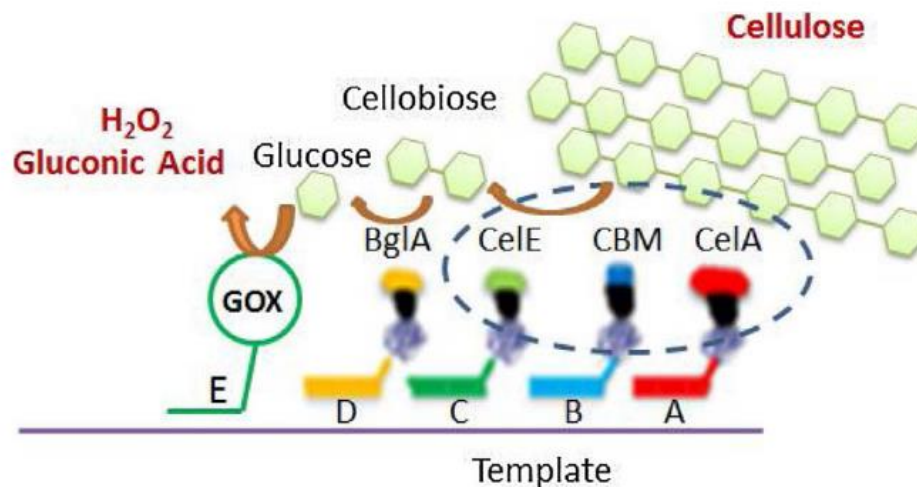


Figure 1.6 Schematic of five-enzyme cascade system for hydrolysis of cellulose and glucose oxidation.⁷⁰

Other 3D structures utilizing DNA such as nano-chambers⁷¹ and nanocages⁷² were fabricated for self-assembly of enzyme cascades by GOx and horseradish peroxidase (HRP), which showed enhanced activity compared to when the two enzymes were freely in solution. Chakraborty et al. studied an oxygen-reducing cathode catalyzed by bilirubin oxidase (BOD).⁷³ They used DNA as a template to fabricate gold nanoclusters (AuNC), which enhanced the electron transfer, shown by 15 mV lower overpotential as well as 5.5 times higher current than when typical plasmonic gold nanoparticle was used in the same configuration. Furthermore, rolling circle amplification was utilized to assemble multiple copies of the enzyme catalysts for enhanced catalytic activity toward reactions that are otherwise impossible to achieve with a single enzyme.^{74,75} Though some of these examples were not readily applied to EFC setups, it is worth noting their potential for future applications in EFC with enhanced catalytic activity and stability.

1.5 Nanomaterial-based electrodes

The high surface area-to-volume ratio and variability of physical and chemical properties by precise control of morphologies have made nanomaterials attractive and superior to their bulk counterparts in numerous applications. Taking advantage of such properties to increase not only the enzyme loading but also protection around the enzyme catalysts can allow the nanomaterial-based EFC electrodes to increase stability and decrease the enzyme-to-electrode distance for more efficient direct electron transfer.

1.5.1 Carbonaceous materials

Carbon-based nanomaterials exhibit high electrical conductivity and good mechanical properties, as well as various physical and electrical properties depending on the control of their morphologies. Various carbonaceous materials such as carbon fibers or papers,⁷⁶⁻⁷⁸ carbon black,⁷⁹⁻⁸³ carbon nanoparticles,⁸⁴ graphene,⁸⁵⁻⁸⁷ and carbon nanotubes^{43,88-91} have been employed as EFC electrode materials.

First discovered by Ijima et al. in 1991,⁹² carbon nanotubes (CNTs) now are one of the most widely used nanomaterials for fabrication of enzyme electrodes, largely due to high surface area-to-volume ratio and flexibility towards surface chemistry manipulation to enhance enzyme immobilization.^{93,94} Carbon nanotubes are typically physisorbed or compressed with enzyme catalyst of choice, followed by coating of semi-permeable polymer like Nafion to prevent desorption or leaching of the enzymes. Recently, however, more complex setups have been reported to enhance the immobilization of the enzyme as

well as electron transfer by using electrode materials of higher surface area and electrical conductivity. Carbon-based electrode materials were chemically modified or doped for increased enzyme loading and stability of enzyme immobilization,^{83,95–98} decorated with metallic nanomaterials for covalent bonding of enzymes and enhanced electron transfer,^{26,99} or combined with various carbonaceous nanomaterials to form composite electrodes.^{64,85,100,101}

1.5.2 Porous nanostructure

The ultra-large surface area-to-volume ratio with fine-tunable pore size, density, and overall nanostructure dimensions, porous nanostructures have shown to be excellent candidates for EFC electrode materials. Though enzymeless, catalytic glucose oxidation by Rong et al. described the high porosity of the polymer matrix employed around the gold nanoparticle catalyst provided size-selective protection against larger molecules.¹⁰² Similar to this work, enzymatic electrodes are also fabricated based on porous structures in order to protect the enzyme catalysts, while allowing more contact area to enhance the DET rate. The significance of mesoporous electrodes (i.e. containing pores of diameter between 2 and 50 nm) is supported by (i) the curvature effect,^{103,104} in which the current density largely increases as pore diameter approaches that of a single enzyme; as well as (ii) the electrostatic interaction between the enzyme and the electrode, where the surface charge of the electrodes can promote the preferred orientation of the enzymes so that the distance between the enzyme active site and the electrode is minimized.^{105–108} With these in mind, meso- and microporous electrodes were fabricated based on glassy carbon electrodes modified with Ketjen Black and gold nanoparticles to improve the direct electron transfer

kinetics of several redox enzymes such as bilirubin oxidase, hydrogenase and formate dehydrogenase.¹⁰⁹ Based on the electrochemical behavior of these electrodes characterized by cyclic voltammetry, combined with electrostatic charge distribution visualized by PyMOL, it was suggested that electrodes with controlled morphology such as mesoporous structure was a predominant factor in facilitating DET of the three enzymes. The mechanism of DET based on porous electrodes and the optimum porous nanomaterial for DET were mathematically modelled and experimentally validated by Do et al. and Mazurenko et al., respectively.^{110,111}

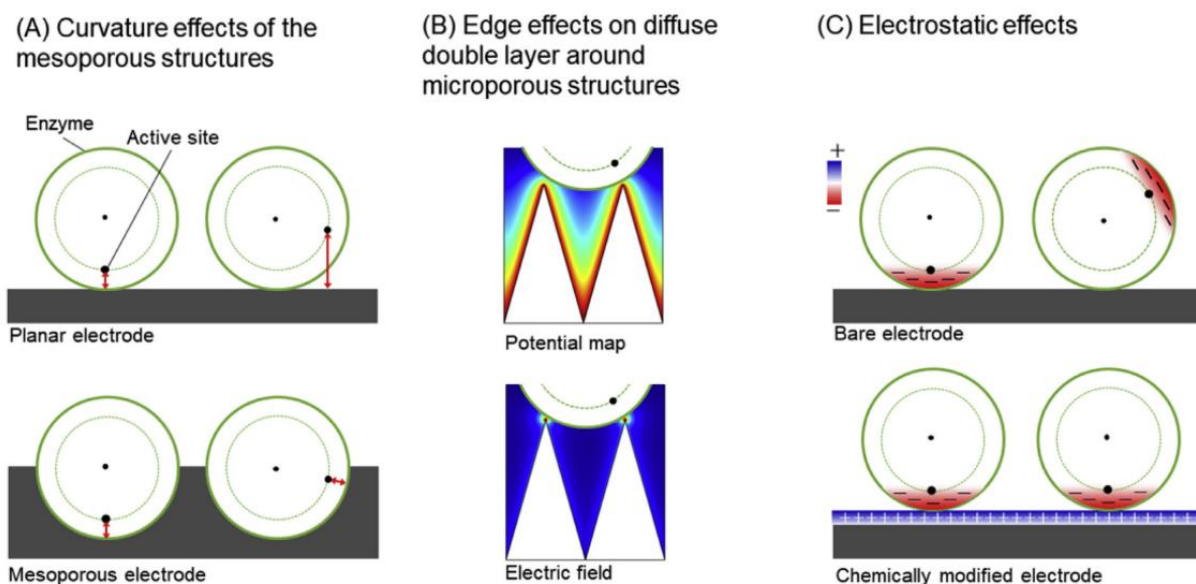


Figure 1.7 Schematics showing (A) curvature effect (B) edge effect (C) electrostatic effect that are taken into account for meso- and microporous structures.¹⁰⁹

Various porous materials were utilized as electrodes to be functionalized with enzyme catalysts. Wang *et al.* deposited single-walled carbon nanotube on gold-coated porous silicon substrates, onto which GOx and Lc were electrochemically immobilized to fabricate bioanode and biocathode, respectively. Enzymatic fuel cell built with these

electrodes produced peak power density of $1.38 \mu\text{W}/\text{cm}^2$ for up to 24 hours.¹¹² Though the power density output was not as high compared to similar works, it was important to note that both membrane- and mediator-free enzymatic fuel cell was demonstrated with glucose at a near-physiological concentration for potential in biomedical application. Improved peak power density and stability of up to $12 \mu\text{W}/\text{cm}^2$ and 48 hours, respectively, were later demonstrated by the same setup and group later that year.¹¹³ A work by du Toit and Di Lorenzo demonstrated the feasibility of highly porous gold electrodes for use in biofuel cell with GOx and and laccase as anodic and cathodic catalysts, respectively, producing peak power density of $6 \mu\text{W}/\text{cm}^2$,¹¹⁴ a comparable value to other miniature EFCs.^{115,116} Their effort continued to develop a flow-through glucose/oxygen fuel cell based on highly porous gold electrodes for continuous power generation for up to 24 hours.¹¹⁷ Salaj-Kosla *et al.* also utilized nanoporous gold electrodes to immobilize bilirubin oxidase by physisorption to produce catalytic current density of $0.8 \text{ mA}/\text{cm}^2$.¹¹⁸ More recently, bioelectrocatalysis by bilirubin oxidase was further improved by immobilizing it onto porous gold¹¹⁹ and mesoporous carbon electrodes¹²⁰, which was attributed to the appropriate pore size distribution as well as promotion of favorable orientation of the enzyme for direct electron transfer.

1.5.3 Gold nanoparticles

Due to their unique physical and electrical properties, gold nanoparticles (AuNPs) are among popular materials with which to functionalize EFC electrodes. In addition, the various facile synthesis protocols and size control techniques make AuNPs more attractive in enhancing the enzyme electrode performance. AuNPs themselves can be modified with

functional groups such as thiols to covalently attach to electrode surface, improving the stability when the enzymes are adsorbed onto the AuNP functionalized electrodes, in which the AuNPs act as electronic bridges between the enzyme active site and the electrode surface. Monsalve *et al.* used a thiolated AuNPs of various sizes to covalently bind to a hydrogenase for bioanode fabrication, during which the smallest AuNPs were found to exhibit the highest surface area, leading to a 170-fold increase in current density from DET-based hydrogen oxidation compared to using unmodified bulk gold electrode.¹²¹ Combined with BOD-modified cathode, the as-fabricated EFC produced power density of up to 0.25 mW/cm². Ratautas *et al.* fabricated a bioanode with AuNP modified with 4-aminothiophenol (4-ATP), which contained oxidized derivatives that allowed for stable immobilization of glucose dehydrogenase, and confirmed its mediator-free glucose oxidation electrochemically.¹²² Biocathodes based on AuNPs as electronic bridges for laccase were also fabricated by Kang *et al.*; laccase was immobilized onto naphthalenethiol-modified AuNPs, which promoted the electron transfer to the polyethyleneimine-carbon nanotube electrode.¹²³ The high-surface area electrode also increased the enzyme loading, producing 13 $\mu\text{W}/\text{cm}^2$ power density when put together into EFC. AuNPs were employed in both anode and cathode for sugar/oxygen EFC with cellobiose dehydrogenase and bilirubin oxidase as anodic and cathodic catalyst, respectively; the EFC showed improved performance than previously fabricated EFCs (i.e. power density of 15 $\mu\text{W}/\text{cm}^2$ in buffer and 3 $\mu\text{W}/\text{cm}^2$ in human blood), which was attributed to the use of 3D AuNP-modified electrodes.¹²⁴ AuNPs are also used with other

electrically conductive materials such as conducting polymers and carbon nanotubes to further enhance the electrical properties for more stable DET.^{52,125}

1.6 Recent progress in biomedical application of DET-enabled EFC

Implantable devices powered by EFCs are increasingly attracting research attention since high substrate specificity of enzyme catalysts remove the need for compartments or membranes, allowing for miniaturization. Furthermore, use of biocompatible nanomaterials for electrodes has shown great potential in implantable EFC devices. Though mediated electron transfer-based EFCs have shown potential for implantable device applications earlier and consistently grown,¹²⁶⁻¹²⁹ DET-enabled EFCs closely followed the trend. Starting from those fueled by clams¹³⁰ and lobsters,¹³¹ DET-driven EFCs were surgically implanted on an exposed rat tissue¹³² and finally in the abdominal cavity of a rat to truly show the potential of biocompatible, implantable EFC to power devices, which was demonstrated by the powering of light-emitting diode (LED) and a digital thermometer.¹³³ To accomplish this, Zebda et al. wrapped the enzyme electrodes in silicone bags, followed by a dialysis bag filled with sterile solution and then an autoclaved commercial sleeve to avoid inflammation or toxicity issue with the rat tissue.

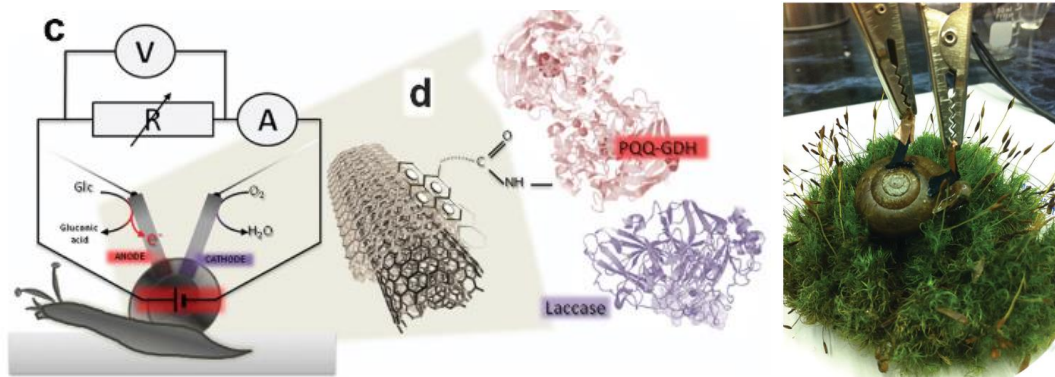


Figure 1.8 Schematic of enzymatic fuel cell using live snail. Figures are from work by Halámková et al.¹³⁴

The effort towards implantable EFC-powered devices for humans have also been consistent. Bollella et al. demonstrated a proof of concept with a FAD-based CDH and Lc as bioanodic and biocathodic enzyme catalyst, respectively, immobilized on a gold nanoparticle-functionalized graphene screen-printed electrode; the EFC with both enzyme catalysts co-immobilized on the same electrode showed power output of $1.10 \mu\text{W}/\text{cm}^2$ and open-circuit voltage of 0.41 V in real human saliva samples, hinting at a potential non-invasive autonomous biodevices.¹³⁵ DET-enabled EFCs also exhibited stable operation in other human liquids such as serum, saliva, and urine, ranging in power density of 12 to $18 \mu\text{W}/\text{cm}^2$.¹³⁶ Operation of mediatorless EFC utilizing various enzymes such as PQQ-GDH and cellobiose dehydrogenase in real or synthetic human tear was observed, giving possibility of EFCs powering “smart” contact lenses.^{137,138}

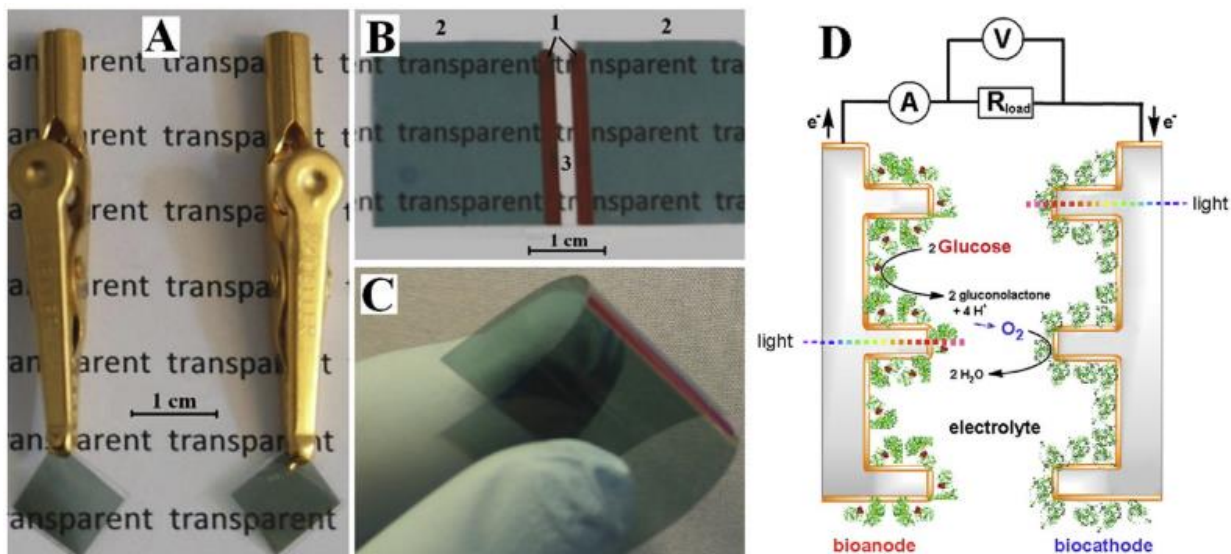


Figure 1.9 (a-c) Optical images of enzymatic fuel cell based on transparent and flexible electrodes. (d) Schematic of membrane- and mediator-free glucose/oxygen biofuel cell.¹³⁹

Pankratov et al. utilized transparent, flexible substrate upon which CDH and BOx were immobilized was used to produce maximum of $0.6 \mu\text{W}/\text{cm}^2$ and maintain $\sim 80\%$ of the initial power density after 12 hours of operation.¹³⁹ The use of the transparent substrate and the minimal impact on the transparency upon enzyme immobilization, combined with relatively stable operation of the EFC, suggests its potential as a power source for smart contact lenses. The low power output of the implantable DET-enabled EFC in human physiological fluids (compared to $\sim 40 \mu\text{W}/\text{cm}^2$ achieved by Milton et al. via mediated glucose oxidation in human serum at 21°C ¹⁴⁰) was primarily attributed to the extremely low glucose concentration, but given that some cases of MET-based EFC was able to show higher power outputs, there are certainly more optimization and improvements needed before implementing DET-based EFCs to power implantable devices.

1.7 Conclusions and outlook

In addition to the method of green energy production, enzymatic fuel cells offer many advantages such as potential for miniaturization and flexibility of fuels. With proper engineering of various components of the EFC, scientific community has come a long way in enhancing the EFC performance including power density and open circuit potential in a push towards real-life applications, especially in the biomedical field. Both biocatalysts and electrodes were engineered to promote higher catalytic activity, more efficient electron transfer, and faster current collection to maximize power generation. Some engineering methods have been employed to prolong the activity of the biocatalysts and therefore the stability of the EFC performance.

Even though many potential applications have been explored, some of which were very promising, EFCs still suffer greatly from lack of long-term stability and low power density with fuel concentrations as low as physiological conditions. However, the ongoing debate on whether or not MET is better than DET or vice versa may be the bottleneck that takes away the focus from realization of EFCs in real-life applications. More research based on fundamentals of enzymatic and electroactivity of the biocatalysts may be necessary to undeniably support or refute the direct electron transfer of some popular enzymes like glucose oxidase.

1.8 References

1. Yahiro, A. T., Lee, S. M. & Kimble, D. O. Bioelectrochemistry. I. Enzyme utilizing bio-fuel cell studies. *BBA - Spec. Sect. Biophys. Subj.* **88**, 375–383 (1964).
2. Davis, J. & Yarbrough, H. Biochemical fuel cell. (1967).
3. Hunger, H., Branch, L. & Perry, J. Biochemical fuel cell. (1966).
4. Betso, S. R., Klapper, M. H. & Anderson, L. B. Electrochemical Studies of Heme Proteins. Coulometric, Polarographic, and Combined Spectroelectrochemical Methods for Reduction of the Heme Prosthetic Group in Cytochrome c. *J. Am. Chem. Soc.* **94**, 8197–8204 (1972).
5. Berezin, I. V., Bogdanovskaya, V. A., Varfolomeev, S. D., Tarasevich, M. R. & Yaropolov, A. I. No Title. *Dokl. Akad. Nauk SSSR* **240**, 615–618 (1978).
6. Jamshidinia, Z. *et al.* Investigation of direct and mediated electron transfer of laccase-based biocathode. *J. Electrochem. Sci. Technol.* **8**, 87–95 (2017).
7. Mani, P., Kumar, V. T. F., Keshavarz, T., Sainathan Chandra, T. & Kyazze, G. The role of natural laccase redox mediators in simultaneous dye decolorization and power production in microbial fuel cells. *Energies* **11**, 1–12 (2018).
8. Mazurenko, I., Wang, X., De Poulpique, A. & Lojou, E. H₂/O₂ enzymatic fuel cells: from proof-of-concept to powerful devices. *Sustain. Energy Fuels* **1**, 1475–1501 (2017).
9. Kawai, S. *et al.* The electron transfer pathway in direct electrochemical communication of fructose dehydrogenase with electrodes. *Electrochem. commun.* **38**, 28–31 (2014).
10. Shleev, S. *et al.* Oxygen Electroreduction versus Bioelectroreduction: Direct Electron Transfer Approach. *Electroanalysis* **28**, 2270–2287 (2016).
11. Luong, J. H. T., Glennon, J. D., Gedanken, A. & Vashist, S. K. Achievement and assessment of direct electron transfer of glucose oxidase in electrochemical biosensing using carbon nanotubes, graphene, and their nanocomposites. *Microchim. Acta* **184**, 369–388 (2017).
12. Bartlett, P. N. & Al-lolage, F. A. There is no evidence to support literature claims of direct electron transfer (DET) for native glucose oxidase (GOx) at carbon nanotubes or graphene. *J. Electroanal. Chem.* **819**, 26–37 (2018).

13. Wilson, G. S. Native glucose oxidase does not undergo direct electron transfer. *Biosensors and Bioelectronics* vol. 82 vii–viii (2016).
14. Navaee, A. & Salimi, A. FAD-based glucose dehydrogenase immobilized on thionine/AuNPs frameworks grafted on amino-CNTs: Development of high power glucose biofuel cell and biosensor. *J. Electroanal. Chem.* **815**, 105–113 (2018).
15. Saleh, F. S., Mao, L. & Ohsaka, T. Development of a dehydrogenase-based glucose anode using a molecular assembly composed of nile blue and functionalized SWCNTs and its applications to a glucose sensor and glucose/O₂ biofuel cell. *Sensors Actuators, B Chem.* **152**, 130–135 (2011).
16. Scherbahn, V. *et al.* Biofuel cells based on direct enzyme-electrode contacts using PQQ-dependent glucose dehydrogenase/bilirubin oxidase and modified carbon nanotube materials. *Biosens. Bioelectron.* **61**, 631–638 (2014).
17. Schubart, I. W., Göbel, G. & Lisdat, F. A pyrroloquinolinequinone-dependent glucose dehydrogenase (PQQ-GDH)-electrode with direct electron transfer based on polyaniline modified carbon nanotubes for biofuel cell application. *Electrochim. Acta* **82**, 224–232 (2012).
18. Aiba, H. *et al.* Characterization of a thermostable glucose dehydrogenase with strict substrate specificity from a hyperthermophilic archaeon *Thermoproteus* sp. GDH-1. *Biosci. Biotechnol. Biochem.* **79**, 1094–1102 (2015).
19. Desriani, Hanashi, T., Yamazaki, T., Tsugawa, W. & Sode, K. Enzyme Fuel Cell for Cellulolytic Sugar Conversion Employing FAD Glucose Dehydrogenase and Carbon Cloth Electrode Based on Direct Electron Transfer Principle. *Open Electrochem. J.* **2**, 6–10 (2010).
20. Muguruma, H., Iwasa, H., Hidaka, H., Hiratsuka, A. & Uzawa, H. Mediatorless Direct Electron Transfer between Flavin Adenine Dinucleotide-Dependent Glucose Dehydrogenase and Single-Walled Carbon Nanotubes. *ACS Catal.* **7**, 725–734 (2017).
21. Lee, I. *et al.* The electrochemical behavior of a FAD dependent glucose dehydrogenase with direct electron transfer subunit by immobilization on self-assembled monolayers. *Bioelectrochemistry* **121**, 1–6 (2018).
22. PrévotEAU, A., Courjean, O. & Mano, N. Deglycosylation of glucose oxidase to improve biosensors and biofuel cells. *Electrochem. commun.* **12**, 213–215 (2010).
23. Holland, J. T., Lau, C., Brozik, S., Atanassov, P. & Banta, S. Engineering of glucose oxidase for direct electron transfer via site-specific gold nanoparticle conjugation. *J. Am. Chem. Soc.* **133**, 19262–19265 (2011).

24. Hibino, Y., Kawai, S., Kitazumi, Y., Shirai, O. & Kano, K. Construction of a protein-engineered variant of D -fructose dehydrogenase for direct electron transfer-type bioelectrocatalysis. *Electrochem. commun.* **77**, 112–115 (2017).
25. Kaida, Y., Hibino, Y., Kitazumi, Y., Shirai, O. & Kano, K. Ultimate downsizing of D -fructose dehydrogenase for improving the performance of direct electron transfer-type bioelectrocatalysis. *Electrochem. commun.* **98**, 101–105 (2019).
26. Lalaoui, N. *et al.* Direct Electron Transfer between a Site-Specific Pyrene-Modified Laccase and Carbon Nanotube/Gold Nanoparticle Supramolecular Assemblies for Bioelectrocatalytic Dioxygen Reduction. *ACS Catal.* **6**, 1894–1900 (2016).
27. Spadiut, O. *et al.* Engineering of pyranose 2-oxidase: Improvement for biofuel cell and food applications through semi-rational protein design. *J. Biotechnol.* **139**, 250–257 (2009).
28. Moser, C. C., Keske, J. M., Warncke, K., Farid, R. S. & Dutton, P. L. Nature of biological electron transfer. *Nature* **355**, 796–802 (1992).
29. Lopez, F. *et al.* Potential pulse-assisted immobilization of *Myrothecium verrucaria* bilirubin oxidase at planar and nanoporous gold electrodes. *J. Electroanal. Chem.* **812**, 194–198 (2018).
30. Hitaishi, V. P. *et al.* Controlling redox enzyme orientation at planar electrodes. *Catalysts* **8**, 1–38 (2018).
31. Gutiérrez-Sánchez, C., Pita, M., Vaz-Domínguez, C., Shleev, S. & De Lacey, A. L. Gold nanoparticles as electronic bridges for laccase-based biocathodes. *J. Am. Chem. Soc.* **134**, 17212–17220 (2012).
32. Lalaoui, N. *et al.* Direct Electron Transfer between a Site-Specific Pyrene-Modified Laccase and Carbon Nanotube/Gold Nanoparticle Supramolecular Assemblies for Bioelectrocatalytic Dioxygen Reduction. *ACS Catal.* **6**, 1894–1900 (2016).
33. Ma, S. *et al.* Direct Electron-Transfer Anisotropy of a Site-Specifically Immobilized Cellobiose Dehydrogenase. (2019) doi:10.1021/acscatal.9b02014.
34. Jesionowski, T., Zdarta, J. & Krajewska, B. Enzyme immobilization by adsorption: A review. *Adsorption* vol. 20 801–821 (2014).
35. Walker, J. M. & Trevan, M. D. Enzyme Immobilization by Covalent Bonding. in *New Protein Techniques* 495–510 (Humana Press, 2003). doi:10.1385/0-89603-126-8:495.

36. Luna, C. *et al.* Biochemical catalytic production of biodiesel. *Handbook of Biofuels Production: Processes and Technologies: Second Edition* vol. 3 (Elsevier Ltd, 2016).
37. Mohamad, N. R., Marzuki, N. H. C., Buang, N. A., Huyop, F. & Wahab, R. A. An overview of technologies for immobilization of enzymes and surface analysis techniques for immobilized enzymes. *Biotechnology and Biotechnological Equipment* vol. 29 205–220 (2015).
38. Andreescu, S., Bucur, B. & Marty, J.-L. Affinity Immobilization of Tagged Enzymes. in 97–106 (Humana Press, 2006). doi:10.1007/978-1-59745-053-9_9.
39. Sun, Q. & Chen, W. HaloTag mediated artificial cellulosome assembly on a rolling circle amplification DNA template for efficient cellulose hydrolysis. *Chem. Commun.* **52**, 6701–6704 (2016).
40. Strack, G. *et al.* Power generation from a hybrid biological fuel cell in seawater. *Bioresour. Technol.* **128**, 222–228 (2013).
41. Narváez Villarrubia, C. W. *et al.* Practical electricity generation from a paper based biofuel cell powered by glucose in ubiquitous liquids. *Electrochem. commun.* **45**, 44–47 (2014).
42. Das, D., Ghosh, S. & Basumallick, I. Electrochemical Studies on Glucose Oxidation in an Enzymatic Fuel Cell with Enzyme Immobilized on to Reduced Graphene Oxide Surface. *Electroanalysis* **26**, 2408–2418 (2014).
43. Liu, Y., Zhang, J., Cheng, Y. & Jiang, S. P. Effect of Carbon Nanotubes on Direct Electron Transfer and Electrocatalytic Activity of Immobilized Glucose Oxidase. *ACS Omega* **3**, 667–676 (2018).
44. Umaña, M. & Waller, J. Protein-Modified Electrodes. The Glucose Oxidase/Polypyrrole System. *Anal. Chem.* **58**, 2979–2983 (1986).
45. Kizling, M. *et al.* Pseudocapacitive polypyrrole-nanocellulose composite for sugar-air enzymatic fuel cells. *Electrochem. commun.* **50**, 55–59 (2015).
46. Kizling, M. *et al.* Bioelectrodes based on pseudocapacitive cellulose/polypyrrole composite improve performance of biofuel cell. *Bioelectrochemistry* **112**, 184–190 (2016).
47. Kim, J., Kim, S. I. & Yoo, K. H. Polypyrrole nanowire-based enzymatic biofuel cells. *Biosens. Bioelectron.* **25**, 350–355 (2009).

48. Min, K., Ryu, J. H. & Yoo, Y. J. Mediator-free glucose/O₂ biofuel cell based on a 3-dimensional glucose oxidase/swnt/polypyrrole composite electrode. *Biotechnol. Bioprocess Eng.* **15**, 371–375 (2010).
49. Liu, C., Chen, Z. & Li, C. Z. Surface engineering of graphene-enzyme nanocomposites for miniaturized biofuel cell. *IEEE Trans. Nanotechnol.* **10**, 59–62 (2011).
50. Gutiérrez-Domínguez, D. E., Pacheco-Catalán, D. E., Patiño-Díaz, R., Canto-Canché, B. & Smit, M. A. Development of alcohol dehydrogenase-polypyrrole electrodes by adsorption and crosslinking for ethanol oxidation. *Int. J. Hydrogen Energy* **38**, 12610–12616 (2013).
51. Christwardana, M., Chung, Y. & Kwon, Y. A new biocatalyst employing pyrenecarboxaldehyde as an anodic catalyst for enhancing the performance and stability of an enzymatic biofuel cell. *NPG Asia Mater.* **9**, 1–9 (2017).
52. Tavahodi, M. *et al.* Direct Electron Transfer of Cellobiose Dehydrogenase on Positively Charged Polyethyleneimine Gold Nanoparticles. *Chempluschem* **82**, 546–552 (2017).
53. Sapountzi, E. *et al.* Gold nanoparticles assembly on electrospun poly(vinyl alcohol)/poly(ethyleneimine)/glucose oxidase nanofibers for ultrasensitive electrochemical glucose biosensing. *Sensors Actuators, B Chem.* **238**, 392–401 (2017).
54. Christwardana, M., Kim, K. J. & Kwon, Y. Fabrication of Mediatorless/Membraneless Glucose/Oxygen Based Biofuel Cell using Biocatalysts Including Glucose Oxidase and Laccase Enzymes. *Sci. Rep.* **6**, 1–10 (2016).
55. Christwardana, M., Kim, D. H., Chung, Y. & Kwon, Y. A hybrid biocatalyst consisting of silver nanoparticle and naphthalenethiol self-assembled monolayer prepared for anchoring glucose oxidase and its use for an enzymatic biofuel cell. *Appl. Surf. Sci.* **429**, 180–186 (2018).
56. Chung, Y., Ahn, Y., Kim, D. H. & Kwon, Y. Amide group anchored glucose oxidase based anodic catalysts for high performance enzymatic biofuel cell. *J. Power Sources* **337**, 152–158 (2017).
57. Zeng, T. *et al.* Miniature direct electron transfer based sulphite / oxygen enzymatic fuel cells. *Biosens. Bioelectron.* **66**, 39–42 (2015).

58. Gerard, M., Ramanathan, K., Chaubey, A. & Malhotra, B. D. Immobilization of Lactate Dehydrogenase on Electrochemically Prepared Polyaniline Films. *Electroanalysis* **11**, 450–452 (1999).
59. Kim, R. E., Hong, S. G., Ha, S. & Kim, J. Enzyme adsorption, precipitation and crosslinking of glucose oxidase and laccase on polyaniline nanofibers for highly stable enzymatic biofuel cells. *Enzyme Microb. Technol.* **66**, 35–41 (2014).
60. Kim, H. *et al.* Immobilization of glucose oxidase into polyaniline nanofiber matrix for biofuel cell applications. *Biosens. Bioelectron.* **26**, 3908–3913 (2011).
61. Mishra, P. *et al.* Electrocatalytic biofuel cell based on highly efficient metal-polymer nano-architected bioelectrodes. *Nano Energy* **39**, 601–607 (2017).
62. Yan, X., Chen, J., Yang, J., Xue, Q. & Miele, P. Fabrication of free-standing, electrochemically active, and biocompatible graphene oxide-polyaniline and graphene-polyaniline hybrid papers. *ACS Appl. Mater. Interfaces* **2**, 2521–2529 (2010).
63. Kang, Z. *et al.* Graphene oxide-supported carbon nanofiber-like network derived from polyaniline: A novel composite for enhanced glucose oxidase bioelectrode performance. *Biosens. Bioelectron.* **96**, 367–372 (2017).
64. Kashyap, D. *et al.* Multi walled carbon nanotube and polyaniline coated pencil graphite based bio-cathode for enzymatic biofuel cell. *Int. J. Hydrogen Energy* **40**, 9515–9522 (2015).
65. Kumar, R., Bhuvana, T., Mishra, G. & Sharma, A. A polyaniline wrapped aminated graphene composite on nickel foam as three-dimensional electrodes for enzymatic microfuel cells. *RSC Adv.* **6**, 73496–73505 (2016).
66. Xia, L. *et al.* Improving the Performance of Methanol Biofuel Cells Utilizing an Enzyme Cascade Bioanode with DNA-Bridged Substrate Channeling. *ACS Energy Lett.* **2**, 1435–1438 (2017).
67. Müller, J. & Niemeyer, C. M. DNA-directed assembly of artificial multienzyme complexes. *Biochem. Biophys. Res. Commun.* **377**, 62–67 (2008).
68. Conrado, R. J. *et al.* DNA-guided assembly of biosynthetic pathways promotes improved catalytic efficiency. *Nucleic Acids Res.* **40**, 1879–1889 (2012).
69. Fu, J., Liu, M., Liu, Y., Woodbury, N. W. & Yan, H. Interenzyme substrate diffusion for an enzyme cascade organized on spatially addressable DNA nanostructures. *J. Am. Chem. Soc.* **134**, 5516–5519 (2012).

70. Chen, Q., Yu, S., Myung, N. & Chen, W. DNA-guided assembly of a five-component enzyme cascade for enhanced conversion of cellulose to gluconic acid and H₂O₂. *J. Biotechnol.* **263**, 30–35 (2017).
71. Linko, V., Eerikäinen, M. & Kostianen, M. A. A modular DNA origami-based enzyme cascade nanoreactor. *Chem. Commun.* **51**, 5351–5354 (2015).
72. Zhao, Z. *et al.* Nanocaged enzymes with enhanced catalytic activity and increased stability against protease digestion. *Nat. Commun.* **7**, (2016).
73. Chakraborty, S. *et al.* A Hybrid DNA-Templated Gold Nanocluster for Enhanced Enzymatic Reduction of Oxygen. *J. Am. Chem. Soc.* **137**, 11678–11687 (2015).
74. Wilner, O. I., Shimron, S., Weizmann, Y., Wang, Z. G. & Willner, I. Self-assembly of enzymes on dna scaffolds: en route to biocatalytic cascades and the synthesis of metallic nanowires. *Nano Lett.* **9**, 2040–2043 (2009).
75. Sun, Q. & Chen, W. HaloTag mediated artificial cellulosome assembly on a rolling circle amplification DNA template for efficient cellulose hydrolysis. *Chem. Commun.* **52**, 6701–6704 (2016).
76. Kuo, C. H. *et al.* Biofuel cells composed by using glucose oxidase on chitosan coated carbon fiber cloth. *Int. J. Electrochem. Sci.* **8**, 9242–9255 (2013).
77. Xu, S. & Minteer, S. D. Enzymatic Biofuel Cell for Oxidation of Glucose to CO₂. *ACS Catal.* **2**, 91–94 (2012).
78. Hussein, L. *et al.* A highly efficient buckypaper-based electrode material for mediatorless laccase-catalyzed dioxygen reduction. *Biosens. Bioelectron.* **26**, 4133–4138 (2011).
79. Filip, J., Šefčovičová, J., Gemeiner, P. & Tkac, J. Electrochemistry of bilirubin oxidase and its use in preparation of a low cost enzymatic biofuel cell based on a renewable composite binder chitosan. *Electrochim. Acta* **87**, 366–374 (2013).
80. Haneda, K., Yoshino, S., Ofuji, T., Miyake, T. & Nishizawa, M. Sheet-shaped biofuel cell constructed from enzyme-modified nanoengineered carbon fabric. *Electrochim. Acta* **82**, 175–178 (2012).
81. Kamitaka, Y., Tsujimura, S., Setoyama, N., Kajino, T. & Kano, K. Fructose/dioxygen biofuel cell based on direct electron transfer-type bioelectrocatalysis. *Phys. Chem. Chem. Phys.* **9**, 1793–1801 (2007).

82. Gupta, G. *et al.* Direct bio-electrocatalysis by multi-copper oxidases : Gas-diffusion laccase-catalyzed cathodes for biofuel cells. *Electrochim. Acta* **56**, 10767–10771 (2011).
83. Xia, H. qi *et al.* Dual gas-diffusion membrane- and mediatorless dihydrogen/air-breathing biofuel cell operating at room temperature. *J. Power Sources* **335**, 105–112 (2016).
84. Selloum, D. *et al.* Optimized electrode arrangement and activation of bioelectrodes activity by carbon nanoparticles for efficient ethanol microfluidic biofuel cells. *J. Power Sources* **269**, 834–840 (2014).
85. Campbell, A. S. *et al.* Membrane/mediator-free rechargeable enzymatic biofuel cell utilizing graphene/single-wall carbon nanotube cogel electrodes. *ACS Appl. Mater. Interfaces* **7**, 4056–4065 (2015).
86. Song, Y., Chen, C. & Wang, C. Graphene/enzyme-encrusted three-dimensional carbon micropillar arrays for mediatorless micro-biofuel cells. *Nanoscale* **7**, 7084–7090 (2015).
87. Chen, J. *et al.* Engineering graphene/carbon nanotube hybrid for direct electron transfer of glucose oxidase and glucose biosensor. *J. Appl. Electrochem.* **42**, 875–881 (2012).
88. Gao, F., Viry, L., Maugey, M., Poulin, P. & Mano, N. Engineering hybrid nanotube wires for high-power biofuel cells. *Nat. Commun.* **1**, (2010).
89. Ciaccafava, A. *et al.* Electrochemistry Communications An innovative powerful and mediatorless H₂ / O₂ biofuel cell based on an outstanding bioanode. *Electrochem. commun.* **23**, 25–28 (2012).
90. Agnès, C., Reuillard, B., Le Goff, A., Holzinger, M. & Cosnier, S. A double-walled carbon nanotube-based glucose/H₂O₂ biofuel cell operating under physiological conditions. *Electrochem. commun.* **34**, 105–108 (2013).
91. Zebda, A. *et al.* Mediatorless high-power glucose biofuel cells based on compressed carbon nanotube-enzyme electrodes. *Nat. Commun.* **2**, (2011).
92. Iijima, S. Helical microtubules of graphitic carbon. *Nature* **354**, 56–58 (1991).
93. Liu, X. *et al.* Optimization of surface chemistry on single-walled carbon nanotubes for in vivo photothermal ablation of tumors. *Biomaterials* **32**, 144–151 (2011).

94. Yan, L., Zhao, F., Li, S., Hu, Z. & Zhao, Y. Low-toxic and safe nanomaterials by surface-chemical design, carbon nanotubes, fullerenes, metallofullerenes, and graphenes. *Nanoscale* **3**, 362–382 (2011).
95. Meredith, M. T. *et al.* Anthracene-modified multi-walled carbon nanotubes as direct electron transfer scaffolds for enzymatic oxygen reduction. *ACS Catal.* **1**, 1683–1690 (2011).
96. Karaśkiewicz, M. *et al.* Fully enzymatic mediatorless fuel cell with efficient naphthylated carbon nanotube-laccase composite cathodes. *Electrochem. commun.* **20**, 124–127 (2012).
97. Wei, W., Li, P., Li, Y., Cao, X. & Liu, S. Nitrogen-doped carbon nanotubes enhanced laccase enzymatic reactivity towards oxygen reduction and its application in biofuel cell. *Electrochem. commun.* **22**, 181–184 (2012).
98. Giroud, F. & Minteer, S. D. Anthracene-modified pyrenes immobilized on carbon nanotubes for direct electroreduction of O₂ by laccase. *Electrochem. commun.* **34**, 157–160 (2013).
99. Naruse, J. *et al.* Development of biofuel cells based on gold nanoparticle decorated multi-walled carbon nanotubes. *Biosens. Bioelectron.* **30**, 204–210 (2011).
100. Escalona-Villalpando, R. A. *et al.* Evaluation of hybrid and enzymatic nanofluidic fuel cells using 3D carbon structures. *Int. J. Hydrogen Energy* **43**, 11847–11852 (2018).
101. Wu, X. E., Guo, Y. Z., Chen, M. Y. & Chen, X. D. Fabrication of flexible and disposable enzymatic biofuel cells. *Electrochim. Acta* **98**, 20–24 (2013).
102. Rong, Y. *et al.* Intrinsically porous polymer protects catalytic gold particles for enzymeless glucose oxidation. *Electroanalysis* **26**, 904–909 (2014).
103. Sugimoto, Y., Kitazumi, Y., Shirai, O. & Kano, K. Effects of mesoporous structures on direct electron transfer-Type bioelectrocatalysis: Facts and simulation on a three-dimensional model of random orientation of enzymes. *Electrochemistry* **85**, 82–87 (2017).
104. Sugimoto, Y., Takeuchi, R., Kitazumi, Y., Shirai, O. & Kano, K. Significance of mesoporous electrodes for noncatalytic faradaic process of randomly oriented redox proteins. *J. Phys. Chem. C* **120**, 26270–26277 (2016).

105. Lalaoui, N., Holzinger, M., Le Goff, A. & Cosnier, S. Diazonium Functionalisation of Carbon Nanotubes for Specific Orientation of Multicopper Oxidases: Controlling Electron Entry Points and Oxygen Diffusion to the Enzyme. *Chem. - A Eur. J.* **22**, 10494–10500 (2016).
106. Sugimoto, Y. *et al.* Electrostatic interaction between an enzyme and electrodes in the electric double layer examined in a view of direct electron transfer-type bioelectrocatalysis. *Biosens. Bioelectron.* **63**, 138–144 (2015).
107. Xia, H. Q., Kitazumi, Y., Shirai, O. & Kano, K. Enhanced direct electron transfer-type bioelectrocatalysis of bilirubin oxidase on negatively charged aromatic compound-modified carbon electrode. *J. Electroanal. Chem.* **763**, 104–109 (2016).
108. Xia, H. *qi et al.* Factors affecting the interaction between carbon nanotubes and redox enzymes in direct electron transfer-type bioelectrocatalysis. *Bioelectrochemistry* **118**, 70–74 (2017).
109. Sakai, K., Xia, H., Kitazumi, Y., Shirai, O. & Kano, K. Assembly of direct-electron-transfer-type bioelectrodes with high performance. *Electrochim. Acta* **271**, 305–311 (2018).
110. Do, T. Q. N., Varničić, M., Hanke-Rauschenbach, R., Vidaković-Koch, T. & Sundmacher, K. Mathematical Modeling of a Porous Enzymatic Electrode with Direct Electron Transfer Mechanism. *Electrochim. Acta* **137**, 616–626 (2014).
111. Mazurenko, I. *et al.* Impact of substrate diffusion and enzyme distribution in 3D-porous electrodes: A combined electrochemical and modelling study of a thermostable H₂/O₂ enzymatic fuel cell. *Energy Environ. Sci.* **10**, 1966–1982 (2017).
112. Wang, S. C. *et al.* Membrane-less and mediator-free enzymatic biofuel cell using carbon nanotube/porous silicon electrodes. *Electrochem. commun.* **11**, 34–37 (2009).
113. Wang, S., Patlolla, A. & Iqbal, Z. Carbon Nanotube-based, Membrane-less and Mediator-free Enzymatic Biofuel Cells. in *ECS* vol. 19 55–60 (2009).
114. Du Toit, H. & Di Lorenzo, M. Glucose oxidase directly immobilized onto highly porous gold electrodes for sensing and fuel cell applications. *Electrochim. Acta* **138**, 86–92 (2014).
115. Falk, M., Andoralov, V., Silow, M., Toscano, M. D. & Shleev, S. Miniature biofuel cell as a potential power source for glucose-sensing contact lenses. *Anal. Chem.* **85**, 6342–6348 (2013).

116. Beneyton, T., Wijaya, I. P. M., Salem, C. Ben, Griffiths, A. D. & Taly, V. Membraneless glucose/O₂ microfluidic biofuel cells using covalently bound enzymes. *Chem. Commun.* **49**, 1094–1096 (2013).
117. du Toit, H. & Di Lorenzo, M. Continuous power generation from glucose with two different miniature flow-through enzymatic biofuel cells. *Biosens. Bioelectron.* **69**, 199–205 (2015).
118. Salaj-kosla, U. *et al.* Direct electron transfer of bilirubin oxidase (*Myrothecium verrucaria*) at an unmodified nanoporous gold biocathode. *Electrochem. commun.* **16**, 92–95 (2012).
119. Takahashi, Y., Wanibuchi, M., Kitazumi, Y., Shirai, O. & Kano, K. Improved direct electron transfer-type bioelectrocatalysis of bilirubin oxidase using porous gold electrodes. *J. Electroanal. Chem.* **843**, 47–53 (2019).
120. Takahashi, Y., Kitazumi, Y., Shirai, O. & Kano, K. Improved direct electron transfer-type bioelectrocatalysis of bilirubin oxidase using thiol-modified gold nanoparticles on mesoporous carbon electrode. *J. Electroanal. Chem.* **832**, 158–164 (2019).
121. Monsalve, K. *et al.* Hydrogen bioelectrooxidation on gold nanoparticle-based electrodes modified by *Aquifex aeolicus* hydrogenase: Application to hydrogen/oxygen enzymatic biofuel cells. *Bioelectrochemistry* **106**, 47–55 (2015).
122. Ratautas, D. *et al.* High current, low redox potential mediatorless bioanode based on gold nanoparticles and glucose dehydrogenase from *Ewingella americana*. *Electrochim. Acta* **199**, 254–260 (2016).
123. Kang, S., Yoo, K. S., Chung, Y. & Kwon, Y. Cathodic biocatalyst consisting of laccase and gold nanoparticle for improving oxygen reduction reaction rate and enzymatic biofuel cell performance. *J. Ind. Eng. Chem.* **62**, 329–332 (2018).
124. Wang, X. *et al.* Mediatorless sugar/oxygen enzymatic fuel cells based on gold nanoparticle-modified electrodes. *Biosens. Bioelectron.* **31**, 219–225 (2012).
125. Krikstolaityte, V. *et al.* Mediatorless carbohydrate/oxygen biofuel cells with improved cellobiose dehydrogenase based bioanode. *Fuel Cells* **14**, 792–800 (2014).
126. Mano, N., Mao, F. & Heller, A. Characteristics of a miniature compartment-less glucose-O₂ biofuel cell and its operation in a living plant. *J. Am. Chem. Soc.* **125**, 6588–6594 (2003).

127. Mano, N., Mao, F. & Heller, A. A miniature membrane-less biofuel cell operating at +0.60 V under physiological conditions. *ChemBioChem* **5**, 1703–1705 (2004).
128. Sales, F. C. P. F., Iost, R. M., Martins, M. V. A., Almeida, M. C. & Crespilho, F. N. An intravenous implantable glucose/dioxygen biofuel cell with modified flexible carbon fiber electrodes. *Lab Chip* **13**, 468–474 (2013).
129. Miyake, T. *et al.* Enzymatic biofuel cells designed for direct power generation from biofluids in living organisms. *Energy Environ. Sci.* **4**, 5008–5012 (2011).
130. Szczupak, A. *et al.* Living battery - Biofuel cells operating in vivo in clams. *Energy Environ. Sci.* **5**, 8891–8895 (2012).
131. MacVittie, K. *et al.* From ‘cyborg’ lobsters to a pacemaker powered by implantable biofuel cells. *Energy Environ. Sci.* **6**, 81–86 (2013).
132. Castorena-Gonzalez, J. A. *et al.* Biofuel Cell Operating in Vivo in Rat. *Electroanalysis* **25**, 1579–1584 (2013).
133. Zebda, A. *et al.* Single glucose biofuel cells implanted in rats power electronic devices. *Sci. Rep.* **3**, 1–5 (2013).
134. Halámková, L. *et al.* Implanted biofuel cell operating in a living snail. *J. Am. Chem. Soc.* **134**, 5040–5043 (2012).
135. Bollella, P. *et al.* A Glucose/Oxygen Enzymatic Fuel Cell based on Gold Nanoparticles modified Graphene Screen-Printed Electrode. Proof-of-Concept in Human Saliva. *Sensors Actuators, B Chem.* **256**, 921–930 (2018).
136. Göbel, G. *et al.* Operation of a carbon nanotube-based glucose / oxygen biofuel cell in human body liquids — Performance factors and characteristics. *Electrochim. Acta* **218**, 278–284 (2016).
137. Reid, R. C., Minter, S. D. & Gale, B. K. Contact lens biofuel cell tested in a synthetic tear solution. *Biosens. Bioelectron.* **68**, 142–148 (2015).
138. Falk, M. *et al.* Biofuel cell as a power source for electronic contact lenses. *Biosens. Bioelectron.* **37**, 38–45 (2012).
139. Pankratov, D. *et al.* Transparent and flexible, nanostructured and mediatorless glucose/oxygen enzymatic fuel cells. *J. Power Sources* **294**, 501–506 (2015).
140. Milton, R. D., Lim, K., Hickey, D. P. & Minter, S. D. Employing FAD-dependent glucose dehydrogenase within a glucose / oxygen enzymatic fuel cell operating in human serum. *Bioelectrochemistry* **106**, 56–63 (2015).

2 Electrospun Polyacrylonitrile-Derived Nanofibers and Their Controlled Physical, Piezoelectric, and Electrochemical Properties via Design of Experiment

A part of this chapter is based on: Yu, S. & Myung, N. V. Minimizing the Diameter of Electrospun Polyacrylonitrile (PAN) Nanofibers by Design of Experiments for Electrochemical Application. *Electroanalysis* **30**, (2018).

2.1 Abstract

Pristine and composite nanofibers based on polyacrylonitrile (PAN) were electrospun with solution, electrospinning and environmental conditions systematically varied via a series of design of experiments (DOE). Analyses on the DOEs revealed the effect of the operating conditions on resulting nanofiber properties, including physical, electrical piezoelectric and electrochemical. Regardless of the composite materials, PAN concentration by wt.% was the predominant factor for solution viscosity, which controlled the nanofiber dimensions. Size-dependent piezoelectric properties and voltage output were studied in detail for the first time. Effect of multi-walled carbon nanotube on the piezoelectric properties of PAN was investigated. Electrochemical properties such as double-layer capacitance and polarization resistance were detailed via electroanalytical methods including cyclic voltammetry (CV), linear sweep voltammetry (LSV) and electrochemical impedance spectroscopy (EIS). The effect of DOE factors on the parameters calculated from EIS fitting was analyzed, which showed polarization resistance increased with mesopores created by removing zinc oxide with acid.

2.2 Introduction

2.2.1 Electrospun nanofibers

Nanofibers have long been exploited as a versatile, attractive material compared to their bulk counterparts due to their exceptionally high specific surface area and aspect ratio, highly porous structure, and wide range of materials that can be used for synthesis. Such unique properties helped exhibit their potential in a variety of applications in areas of energy, healthcare, and environment; extensive studies have been conducted using nanofibers in thermoelectrics, piezoelectrics, sensors, scaffold for tissue engineering, drug delivery, filtration, electrode materials for batteries, supercapacitors, fuel cells and solar cells, catalytic support, and smart textiles.

Synthesis methods for nanofibers include sonochemical^{1,2}, polymerization^{3,4}, template-based⁵, self-assembly^{6,7}, electrospinning⁸, and some relatively novel methods such as electrohydrodynamic direct writing^{9,10}, centrifugal jet spinning¹¹⁻¹³, plasma-induced^{14,15}, solution blow spinning^{16,17}, and carbon dioxide laser supersonic drawing¹⁸. A brief overview of the synthesis methods is presented in Table 2.1.

Table 2.1 Overview of synthesis methods for nanofibers.

Method	Principle	Advantages	Disadvantages	Ref.
Sonochemical	High-frequency ultrasound radiation to induce chemical reaction	Prevents unwanted growth and agglomeration	Low throughput	1,2
Polymerization	Precursor solutions mixed often in presence of ultrasonic vibrations	Simple, can prevent unwanted growth	Long time	3,4
Template-based	Nanofibers form through reaction, nucleation, and growth within fixed guides	Uniform dimensions	Catalyst often required; additional step to remove/etch template	5
Self-assembly	Precursors spontaneously combine by various driving forces (i.e. hydrophobic, electrostatic attraction, hydrogen bonding, van der Waals, etc)	Works with biomolecules	Long time; undesired nanostructure growth; low stability of product	6,7
Electrospinning	High electric field charges and pulls precursor solution into jet of nanofibers	Simple, cost-effective; virtually no limit on materials; scalable	High voltage; organic solvents	8
Electrohydrodynamic direct writing	Voltage is applied to pull solution into nanofibers; collected at short distance	Ordered, aligned nanofibers with high precision; can accommodate solid, liquid, gas phase	High voltage	9,10
Centrifugal jet spinning	DC motor spins hollow chamber containing precursor solution, where nanofibers are ejected by centrifugal force	High production rate; low cost	Disordered nanofibers; high temperature	11-13
Plasma-induced	Energetic radicals generated by plasma bombard into clusters, which grow into nanofibers	Rapid reaction	Complex; unwanted growth	14,15
Solution blow spinning	Solution is injected through a nozzle, around which high-velocity gas is injected	High production rate compared to electrospinning; in situ deposition	High-pressure gas	16,17
CO ₂ laser supersonic drawing	CO ₂ laser irradiates fiber supply into nanofibers as it is pulled towards the collector	Can accommodate materials with high melting point; no additional solutions or processes	Requires vacuum; costly	18

Of these methods, electrospinning is widely chosen as it not only is simple and cost-effective but also allows for fine tuning of composition and morphology via process control as well as post-electrospinning treatments. The principle behind electrospinning involves electrostatic repulsion in a high electrical field between a nozzle at which the electrospinning solution is ejected and a collector that is typically grounded. (Figure 2.1) As large amount of voltage is applied to a small droplet of the electrospinning solution, the droplet is charged and pulled into a cone shape, known as the Taylor cone, due to the potential difference. As the applied voltage passes a critical threshold, the droplet accelerates towards the grounded collector as the solvent evaporates, forming a jet of nanofibers. For this relatively simple process, various solution, electrospinning, and environmental conditions can be tuned to control the dimensions and morphology of the resulting nanofibers, and thus fine tune the nanofiber properties to be suitable for specific applications.

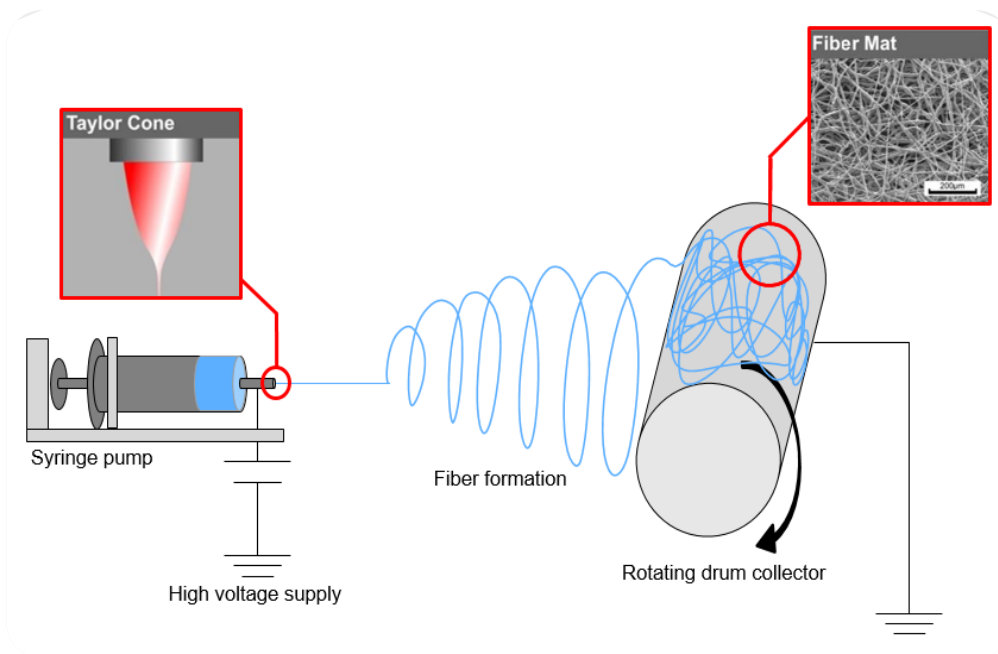


Figure 2.1 Schematic illustration of a typical electrospinning process.

Applications in an area of energy are widely studied, especially because of the global need for a greener source of energy and method of energy production that is alternative to the combustion of fossil fuels. It is well known that this method, while convenient and inexpensive, presents many environmental drawbacks such as greenhouse gas emissions, sulfur dioxide (SO_2) and nitrogen oxide (NO_x) gas emission contributing to acid rain, particulate matter and smog, which ultimately lead to adverse health effects on humans. To bypass the use of fossil fuels, renewable sources such as wind, hydro, geothermal, and solar energy have been introduced; devices that take advantage of alternative sources of energy such as nanogenerators, fuel cells, and thermoelectric generators have been developed.

One of the most attractive benefits of electrospinning is that it not only easily accommodates practically any mixture of components, but also allows for modification via

post-electrospinning processes such as thermal or chemical treatment to produce functional materials securely embedded in polymeric nanofibrous supports. Herein, electrospun polymeric and hybrid nanofibers synthesized for some applications in energy harvesting and generation are reviewed, focusing on the more recent advances (i.e. dating back up to 10 years).

2.2.2 Piezoelectric energy harvesting

With increasing demand for alternative source of energy, ambient sources (i.e. light, thermal gradient, motion) have been explored to harvest energy that would otherwise be wasted. Piezoelectric effect, which describes a phenomenon where electric charge is generated in response to applied mechanical stress or vice versa, has thus been heavily utilized in the field of energy harvesting. Since the first discovery of piezoelectricity in 1880, ceramic piezoelectric materials such as lead zirconate titanate (PZT) and barium titanate (BaTiO_3) made a breakthrough in 1950s.¹⁹ However, the high toxicity of the lead as well as brittleness and inflexibility of many of these ceramic materials deemed them unsuitable for some energy harvesting applications. To bypass these drawbacks, piezoelectricity of polymers such as polyvinylidene fluoride (PVDF) has been extensively investigated since its discovery in the 1960s.²⁰ PVDF is a semi-crystalline polymer with three main polymorph phases: α , β , and γ . (Figure 2.2) The α -phase is the thermodynamically stable crystalline phase at room temperature, with fluorine atoms evenly distributed on either side of the polymer chain and is thus electrically inactive. The polar β -phase consists of fluorine atoms on only one side of the polymer chain and is known

as the electroactive phase, showing the strongest ferroelectric and piezoelectric properties.

Finally, γ -phase is also polar and electroactive, but not as much as the β -phase.

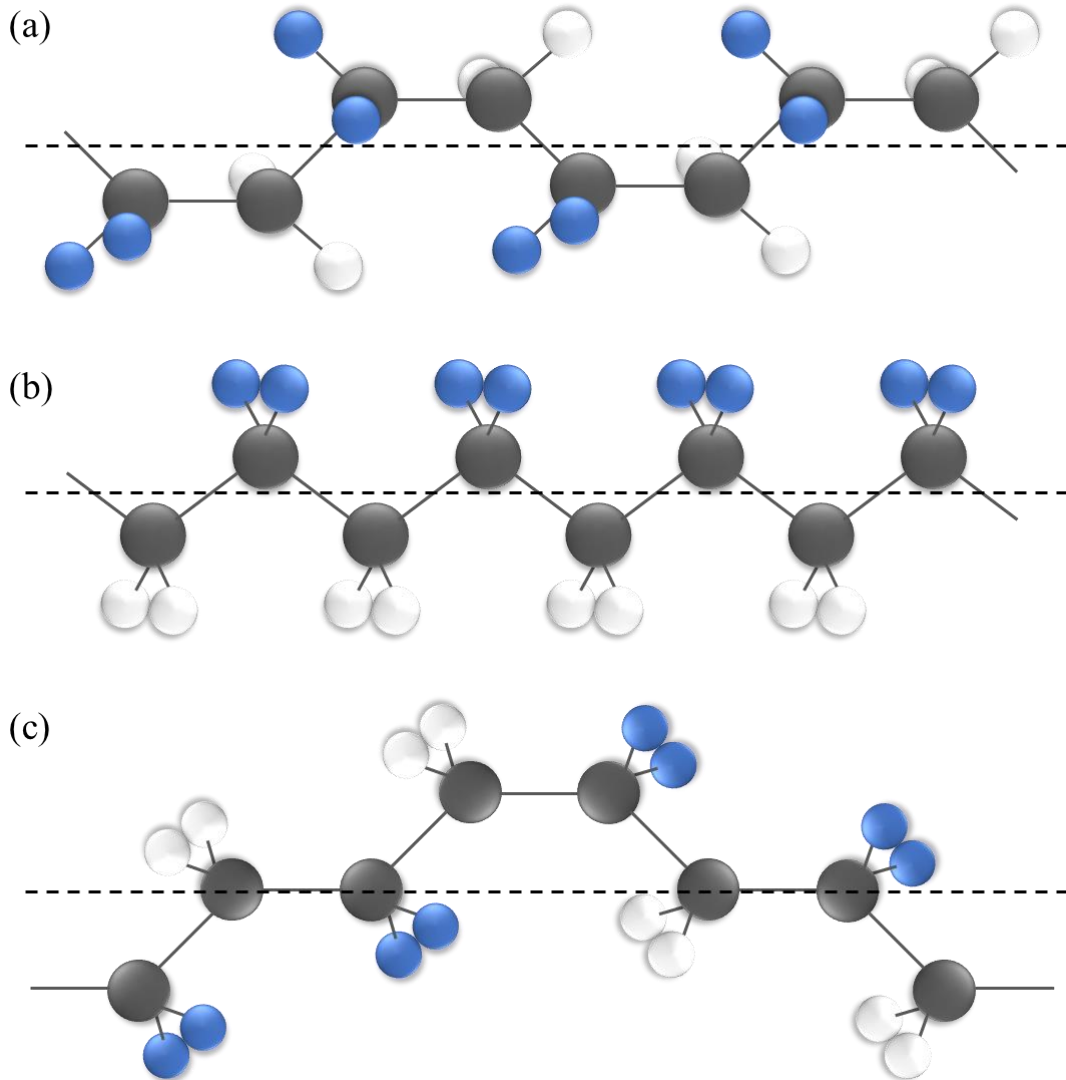


Figure 2.2 Schematic illustration of molecular structure of (a) α (b) β and (c) γ phase of poly(vinylidene fluoride).

As piezoelectric materials are employed as nanogenerators for potentials in self-powered wearable devices, nanofiber structure has been greatly favored due to its flexibility, in addition to that a wide range of materials can be incorporated within the

nanofiber as the support matrix. Furthermore, as more piezoelectric polymers are discovered, piezoelectric inorganic-organic hybrid nanofibers are fabricated for enhanced piezoelectric properties and output.

2.2.2.1 Nanofibers as support matrix for piezoelectric nanomaterials

While ceramics like barium titanate and PZT exhibit significantly higher piezoelectric constants compared to organic materials, many suffer from poor mechanical properties and toxicity issues. In an effort to apply piezoelectric materials to biocompatible applications such as wearable sensors and human kinematics energy harvesters, several methods have been developed. Lead-free nanomaterials have been synthesized to overcome the toxicity of PZT; ceramic nanomaterials are embedded in polymeric nanofibers that act as a support matrix²¹; and either precursors or already-prepared ceramics could be mixed with the polymer solution to fabricate nanofibers via electrospinning followed by calcination to burn off the polymer support. This poses multiple advantages to using freestanding bulk ceramics, including high surface area-to-volume ratio and enhanced mechanical properties.

2.2.2.2 Piezoelectric polymeric nanofibers as freestanding or organic-inorganic hybrid

Due to their biocompatibility and high flexibility, polymer-derived piezoelectric nanofibers are great alternatives to some toxic or brittle ceramic-based piezoelectric materials. They can not only act as a freestanding piezoelectric material but also be combined with other piezoelectric inorganics to fabricate hybrid nanofibers of superior piezoelectric properties. In addition to the extensively studied PVDF and P(VDF-TrFE),

other polymers like poly(l-lactic acid) (PLLA)^{22–27} and polyacrylonitrile (PAN)^{28–31} have been explored for their piezoelectric properties. A common denominator for the piezoelectricity of these electrospun polymeric nanofibers is the dipoles that are typically perpendicular to the polymer chain are aligned transversely along the fiber axis, along which the polymer chains are aligned during the electrospinning process as the polymer solution is mechanically stretched.³² The high electric field applied during the process can also induce piezoelectricity without a separate poling process that is typically required.³³

Local piezoelectric response of a single PVDF nanofiber was demonstrated without any post-electrospinning processing, attributing to ~70% presence of the electroactive β -phase.³⁴ P(VDF-TrFE) nanofibers were twisted into yarn and coil structure to enhance its mechanical properties, exhibited by the strain to failure of up to 740% and energy to failure up to 98 J/g; the as-prepared P(VDF-TrFE) coil showed output voltage of 20 mV with bending.³⁵

Such piezoelectric polymeric nanofibers were employed to fabricate nanogenerator and flexible sensors for potential applications in smart textiles and wearable electronics. For example, Gheibi et al. demonstrated one-step fabrication of PVDF nanofiber-based nanogenerator that outputted peak-to-peak voltage of 1.8 V by finger tapping, while Park et al. reported flexible, skin-attachable sensor using P(VDF-TrFE) nanofiber mat to detect pulse and pulse waveforms at various body conditions (i.e. relaxed vs. after exercise).^{36,37}

Table 2.2. Overview of piezoelectric materials.

Category	Material	Representative piezoelectric mode	Piezoelectric charge constant [pC/N]	References
Ceramics	PZT-5H	d_{33}	680	38
	AlN	d_{33}	2-5	39,40
	Quartz	d_{33}	2	41
	ZnO	d_{33}	12.3	42
	BaTiO ₃	d_{33}	350	43
	LiNbO ₃	d_{33}	9.5	44
	PMN-PT	d_{33}	>1500	45
Polymers	PVDF	d_{33}	15	46
	P(VDF-TrFE)	d_{33}	>20	47
	PLLA	d_{14}	10	48
	PHBV	d_{33}	0.43	49
	Cellulose	d_{14}	4.7-6.4	50
	Collagen	d_{33}	2.5	51
	PAN	d_{33}	2	52

Despite the exceptional mechanical properties and biocompatibility, polymer-derived piezoelectric nanofibers have yet been exploited in some applications due to their relatively poor piezoelectric properties, often indicated by lower piezoelectric charge constants (See Table 2.2). While efforts in optimizing piezoelectric properties of purely polymeric nanofibers have been consistently made (See Section 2.2.2.3), incorporation with other composite materials as hybrid nanofibers is another popular approach to enhance not only the piezoelectric properties itself but also the overall performance and versatility by combining additional electric properties (e.g. triboelectric, ferroelectric, pyroelectric). For example, ferroelectric salt crystal, dabcoHReO_4 , was embedded in polyvinyl alcohol nanofibers, which exhibited peak-to-peak voltage (V_{pp}) of approximately 200 mV at 5 Hz of compression.⁵³ PVDF and thermoplastic polyurethane nanofiber mats were stacked to fabricate pressure sensors to monitor human walking with higher sensitivity than commercially available sensors,⁵⁴ while PVDF nanofibers sandwiched between a pair of conducting fabric electrodes as triboelectric-piezoelectric nanogenerator was used to harvest energy from human walking, exhibiting output voltage, current, and instantaneous power of 210 V, 45 μA , and 2.1 mW, respectively.⁵⁵ This triboelectric-piezoelectric mechanism has been consistently used to enhance the performance of nanofiber-based nanogenerators: P(VDF-TrFE) nanofiber mats have been combined with conductive layers like poly(dimethylsiloxane)/multi-walled carbon nanotube (PDMS/MWNT), Kapton film, or silver nanowire (NW)/carbon nanotube (CNT)-embedded polyurethane nanofiber mat, and PVDF nanofibers with silk nanofibers on conductive fabrics, MWNT/graphene/PDMS layer, or silver NW network-based transparent electrodes.⁵⁶⁻⁶¹

Another approach of achieving hybrid nanofibers for piezoelectric energy harvesting is combination of organic and inorganic piezoelectric materials in nanofiber form. By utilizing polymeric nanofiber with decent piezoelectric properties as the support, organic-inorganic hybrids can overcome the poor mechanical properties of inorganic materials like BaTiO₃, while retaining or even enhancing its piezoelectric properties. Piezoelectric response of BaTiO₃-embedded PVDF nanofibers as a function of BaTiO₃ loading was studied by Lee et al.⁶² Furthermore, Dhakras et al. demonstrated that the high density of interfaces between the organic and inorganic component in BaTiO₃-embedded P(VDF-TrFE) nanofibers led to the enhancement in the dielectric response and thus the power output of the nanogenerator.⁶³ Similarly, BaTiO₃-embedded PVDF composite nanofibers were fabricated into nanogenerators for human kinematics energy harvesting via synergistic piezoelectric effect between the organic and inorganic components, generating up to 112 V of peak-to-peak voltage (V_{pp}) with finger tapping motion⁶⁴ and 10.1 V of open-circuit voltage (V_{oc}) when placed over a knee cap of a human subject while walking.⁶⁵ Zinc oxide (ZnO) is another piezoelectric inorganic material commonly employed in nanofibers, a hybrid of which showed 3 times higher output voltage compared to purely polymeric piezoelectric nanofibers.⁶⁶⁻⁶⁹ Fakhri et al. reported of PVDF nanofibers electrospun directly onto vertically grown ZnO nanorods (NRs), outputting V_{pp} of ~800 mV; they attributed the enhancement of the piezoelectric response compared to the individual components to the alignment of the dipole orientation of ZnO nanorods and PVDF nanofibers, which led to positive addition of piezopotential drop generated from the two components.⁷⁰ Furthermore, the semiconducting properties of the ZnO NRs can

enhance the deformation of the nanofibers they are embedded within, leading to more separation of ionic charges and thus an increase in the electric potential generated by the piezoelectric effect.⁷¹

Other methods include cell-based⁷², doping^{73,74}, and decoration with conductive carbon nanomaterials^{75,76} to enhance the biocompatibility, crystallinity, and electrical conductivity, respectively, which are important features to increase the potential for application in wearable, self-powered electronics, or even incorporation of magnetic nanomaterials to demonstrate piezoelectric energy harvesting from non-mechanical source, i.e. magnetic field-induced microscopic motion.⁷⁷

2.2.2.3 Understanding and optimization of piezoelectric properties in polymeric nanofibers

Many properties that are critical to enhancing the piezoelectric properties have to do with the morphology of electrospun nanofibers, such as the nanofiber diameter, grain size, crystallinity, and the presence of the electroactive phase. This section describes a few methods to not only control these morphological properties but also investigate their effect on the piezoelectric properties of the resulting nanofibers.

One of the most popular approach is to increase the amount of the electroactive phase of the polymer nanofiber. As discussed above, PVDF can exist in three crystalline forms: α , β , and γ , where the polar β -phase is the only one that exhibits piezoelectric properties. Various composite materials are mixed with polymer solutions prior to electrospinning to act as “nanofillers” which apparently interact with the polymer matrix and increase the electroactive phases, especially if the composite material with higher

dipole is incorporated.⁷⁸ Some of these materials include carbonaceous nanomaterials like MWNT⁷⁹⁻⁸¹ and graphene oxide^{78,82}, nanoclay templates and other nanoparticles⁸³⁻⁸⁶. Thermal treatment can also increase the piezoelectric constant by allowing the material to change its crystal phase to more thermodynamically stable one as it is heated. In fact, Mao et al. reported that annealing of P(VDF-TrFE) thin films at or slightly above its Curie temperature, above which materials lose their ferroelectric and piezoelectric behavior, achieved maximum polarization, high crystallinity of β -phase, and low leakage current.⁸⁷ More recently, Baniasadi et al. reported of ~70% increase in crystallinity of P(VDF-TrFE) nanofibers when annealed at temperature between Curie and melting temperature, which translated to an approximately 3-fold increase in the Young's modulus and ~55% increase in the piezoelectric constant.³² Much effort has been focused on improving the crystallinity and the amount of the electroactive phase present in the nanofibers by annealing.^{32,88-90}

Even though nanofiber diameter is considered one of the main morphological properties of electrospun nanofibers, it was not until 2010 that the effect of fiber dimensions on piezoelectric properties was demonstrated.⁹¹ PVDF nanofiber produced by near-field electrospinning exhibited higher energy conversion efficiency via piezoelectric effect compared to thin film counterparts, which was attributed to several possible reasons including reduction of domain wall motion, increase in degree of crystallinity and chain orientation, and size-dependent flexoelectricity.⁹¹ Since then, several attempts have been made to understand the effect of various working parameters involved in the electrospinning process on the fiber morphology and the piezoelectric properties as a result. Shao et al. varied PVDF concentration, applied voltage, and tip-to-collector distance and

observed a trend of increase in β -phase PVDF with decreasing fiber diameter while the polymer concentration was high enough to produce smooth, uniform fibers.⁹² A. Gheibi et al. varied tip-to-collector distance, feed rate, and applied voltage at various PVDF concentration and solvent composition to optimize the electrospinning conditions to fabricate smooth, defect-free PVDF nanofibers for nanogenerator applications.⁹³ While their work was able to suggest possible mechanism for the formation of the electroactive β -phase PVDF during electrospinning, the optimization could have been done more efficiently. The variation of the electrospinning condition was not only a one-factor-at-a-time approach, but also inconsistent for each solution condition. Though some conclusion could be drawn from the trend observed in this case, some might be premature as this approach did not elucidate the effect of each condition. On the other hand, Ico et al. used a systematic variation of factors via a method called a design of experiment (DOE) to quantitatively determine the effect of solution conditions on P(VDF-TrFE) nanofiber dimensions and morphology, which were proven to affect its piezoelectric properties.⁹⁴ Optimization of nanofiber diameter based on the DOE showed exponential increase in peak-to-peak output voltage (V_{pp}) with decrease in nanofiber diameter, which also exhibited higher d_{33} coefficient and Young's modulus. Similar approach was used in fabrication of BaTiO₃ nanofibers to control the dimension and crystal grain size based on DOE of solution, electrospinning, environmental and annealing conditions.⁹⁵ This work reported an increase of d_{33} coefficient as a function of fiber diameter and annealing conditions, exhibiting up to 76 pm/V, while a nanogenerator fabricated with the BaTiO₃ nanofiber embedded in PDMS produced maximum power density of 1.95 $\mu\text{W}/\text{cm}^2$.

2.2.3 Nanofibers for fuel cells

Nanofibers are a favorable structure for applications such as supercapacitors, batteries, and fuel cells due to their high specific surface area, which allows for enhanced charge transport as well as high catalyst loading compared to its bulk counterparts. Furthermore, facile control of morphology, composition and crystal structure of the nanofibers allow for fine tuning of physical, electrical and electrochemical properties for enhanced performance in these applications. For fuel cells, in particular, nanofibers have been used as a means to push for higher power density and stability, taking advantage of the ultra-high specific surface area to increase catalyst loading, various materials that exhibit high electrical conductivity for low IR drop, and functional materials or post-electrospinning processes to enhance properties that affect the fuel cell performance such as proton conductivity, ion permittivity and electron transfer rate.

2.2.3.1 Nanofiber mat electrodes

Fuel cell is a device that converts chemical energy from a fuel into electricity through a chemical reaction. A fuel is catalytically oxidized at the anode to release a number of electrons, which transfer to the electrode surface and travel through the circuit to be consumed at the cathode during a reduction reaction. Meanwhile, in some fuel cell types, positively charged ions travel to the cathode through a membrane to also be consumed in a reduction reaction, typically to produce water as byproduct. During this process, the electrodes and the membrane play a critical role in determining the fuel cell performance. The activity, loading, and stability of the catalyst at the anode and/or the

cathode, as well as the electron transport could be affected by the morphology, composition, and porosity of the nanofiber mat electrodes; the ability of the membrane to provide facile pathways for protons while effectively blocking other ions would improve the power density of the fuel cell.

High specific surface area is one of the intrinsic benefits nanofibers offer as electrode material.^{96,97} Activated carbon nanofibers (ACNFs) were suggested as one of the promising materials for fuel cell electrodes. The porous interconnected structure as well as high specific surface area reduced transport limitations while increasing available surface area to catalysts, even in microbial fuel cell applications for biofilm growth.^{98,99} Furthermore, ACNFs showed great potential as an alternative to platinum-based cathodes; a study by Santoro et al found that although ACNF electrode showed slightly lower activity than platinum-carbon (Pt/C) electrode, it maintained its performance under conditions that would typically lead to poisoning of platinum catalysts, especially in real wastewater environment.¹⁰⁰ Conditions for post-electrospinning processes such as sintering could be controlled to further increase specific surface area and enhance catalytic activity.¹⁰¹

Nanofiber mat electrodes are also used as catalyst supports. Non-precious metal-based catalysts such as silver¹⁰², nickel/cadmium¹⁰³ and cobalt/cerium oxide¹⁰⁴ decorated on electrically conductive nanofibers have been reported as potential alternative to overcome the high cost and poisoning susceptibility of Pt. Multiple materials have been incorporated at once to combine their various functionalities, such as high catalytic activity and durability to harsher conditions, while the 1D nanofiber structure provided stable support and high electrical conductivity.¹⁰⁵ The nanofiber skeleton typically derived from

polymer could also be chemically modified to generate pores across the nanofibers for enhanced gas and/or charge transport.¹⁰⁶⁻¹⁰⁸ Recently, such methods have been combined with coaxial electrospinning to fabricate heterostructured composite nanofibers with excellent oxygen reduction reaction activity and stability in a push for commercial use of solid oxide fuel cells.¹⁰⁹

2.2.3.2 Nanofibers as proton exchange membranes

As a popularly used type of fuel cell, proton exchange membrane fuel cell (PEMFC) typically output kilo-Watt range power and have been commercialized for transport applications. In research, there has also been a push to enhance its performance, typically by employing a proton exchange membrane that exhibits superior properties to that of commercial ones like Nafion. Functional groups in various materials were taken advantage of to increase the proton conductivity, water retention, oxygen permittivity and ion barrier properties.¹¹⁰ Much of these enhanced properties were attributed to the functional groups providing facile proton-conducting pathways.^{111,112} Furthermore, the high electrical field applied during the electrospinning aligned the polymer chains, enhancing thermal and hydrolytic stability.¹¹³ Electrospun nanofibers are typically impregnated with commercial Nafion to fabricate a dense membrane, producing a synergistic effect in which the aggregation of Nafion chains on the nanofiber leads to providing the proton-conducting pathways, while the nanofibers alter the crystalline domain of the Nafion to reduce fuel permeability.^{114,115} Post-electrospinning process such as crosslinking with functional materials can even enhance mechanical properties and

solvent resistance, expanding the range of conditions the nanofiber membranes can be used in fuel cells.^{116,117}

Electrospinning, though a simple process, is a method that allows for a wide range of modifications via control of composition, operating conditions, and post-electrospinning processes for fine tuning of nanofiber properties for specific applications. Herein, electrospun nanofibers derived from polyacrylonitrile (PAN) and other composite materials were fabricated with systematic variation of conditions based on a series of design of experiments, and their effects on morphology, electrical, piezoelectric and electrochemical properties were elucidated.

2.3 Materials and Methods

2.3.1 Materials

Polyacrylonitrile (PAN, MW=150,000 g/mol) and pyridinium formate (PF, 1% v/v) were purchased from Sigma-Aldrich. N,N-dimethylformamide (DMF), hydrochloric acid (HCl, 36.5-38.0% w/w) were purchased from Fisher. Zinc acetate (ZnAc) was purchased from Baker & Adamson. BYK®-377 (hereafter referred to as BYK) surfactant was obtained from BYK Additives and Instrumentation. Short COOH functionalized multi-walled carbon nanotubes (MWNT-COOH, hereafter referred to as MWNT, OD 8-15 nm, length 0.5-2.0 μm) were purchased from Cheap Tubes. All materials were used without further treatment.

2.3.2 Methods

2.3.2.1 Solution preparation

Electrospinning solutions were prepared by mixing various amounts of PAN, MWNT, ZnAc, BYK, and PF in DMF. For solutions containing MWNT, MWNT was first dispersed in DMF with BYK in a chilled water bath by probe sonicator (Branson) at 30% amplitude for 2 h with 15 minutes of cooling between each hour. Solid PAN powder was added directly to the MWNT dispersion, while ZnAc was first dissolved in small amount of DMF before mixing into the solution. After mixing in all components, the solution was vigorously stirred at 45 °C overnight to achieve homogeneity. All solutions were allowed to reach room temperature before the next step.

2.3.2.2 Solution characterization

The solution viscosity, surface tension, and electrical conductivity were measured using a viscometer (Brookfield DV-I Prime), automatic surface tensiometer (Shanghai Fangrui Instrument, QBZY-1), and a glass-body electrical conductivity probe (K=0.1, Oakton) paired with an embedded conductivity circuit (Atlas Scientific, EZO-EC™) and an Arduino Uno Rev3 board, respectively. All solution properties measurements were taken at room temperature immediately before or after electrospinning to most closely correlate them to resulting nanofiber properties.

2.3.2.3 Electrospinning

The prepared solution was drawn into a 5-mL BD Luer Lok syringe with a 25- or 20-gauge needle, which was loaded onto a syringe pump (New Era, NE-100). As the solution was ejected, negative voltage was applied to the needle tip, and the resulting nanofibers were collected at a grounded drum collector wrapped with aluminum foil rotating at 400 RPM. Applied voltage and feed rate were varied from 15-25 kV and 0.5-1.0 mL/h, respectively, while temperature and absolute humidity were varied from 23-40 °C and 0.0105-0.0140 kg H₂O/kg dry air (DA), respectively. Hereafter, nanofiber samples were referred to as “xPAN”, “xPAN/yMWNT” or “xPAN/yMWNT/zZnAc”, where x, y, z denoted PAN, MWNT, ZnAc loadings by wt.% with respect to the total mass of the solution, respectively. BYK loadings were assumed as 0.1 wt.% unless otherwise specified.

To prepare nanofibers for piezoelectric properties characterization, various PAN and PAN/MWNT solutions were prepared and electrospun according to the same protocol mentioned above, with slight modifications. Briefly, a thin strip of aluminum foil was wrapped tightly around a disc with diameter and width of 13 and 2.5 cm, respectively. The disc was immobilized onto a metal rod at its center and then loaded onto a mechanical lathe (Central Machinery 93799). During electrospinning, the rotation of the lathe was set at approximately 2000 rpm to align the nanofibers collecting on the foil. A New Era single-channel syringe pump was used to eject 5 mL of prepared solution, and the needle was placed 8-9 cm from the bottom of the disc to minimize the amount of nanofibers lost due to air turbulence. Negative 16 kV voltage was applied to the needle tip, while positive 1

kV voltage was applied to the tip of a banana plug, which was placed behind the grounded disc collector.

2.3.2.4 Post-electrospinning processes

Heat treatment of as-spun nanofiber samples involved 2 steps: stabilization and carbonization. Stabilization was conducted using a box furnace (Thermo Scientific Thermolyne F47925-80 Muffle Furnace) at 280 °C for 1 h at a ramp rate of 5 °C/min in air, while carbonization was conducted using a tube furnace (Thermo Scientific Lindberg/Blue M and Carbolite Gero EHA12/150) at 1000 °C for 1 h at a ramp rate of 5 °C/min in ultra-high purity nitrogen (UHP N₂, 99.999%). In the case of PAN/MWNT/ZnAc nanofibers, stabilization step was slightly modified to a two-step stabilization: the first step of stabilization was kept consistent (280 °C, 5 °C/min, 1 h in air), and then the temperature was increased again to 400 °C with the same ramp rate and held for 1 h in air before natural cooling to room temperature.

During the acid treatment, carbonized nanofiber samples were submerged in HCl diluted at 10% v/v in DI water for 60 s. The sample was gently shaken under the HCl solution to allow for uniform acid treatment, then submerged in 2 separate DI water baths to rinse and then air-dried overnight.

2.3.2.5 Nanofiber characterization

2.3.2.5.1 Physical properties

Morphology of the nanofiber samples was observed with a scanning electron microscope (SEM, Tescan Vega3) and field-emission scanning electron microscope (FESEM, FEI Nova NanoSEM450) with energy dispersive spectroscopy detector (EDS, Aztec, Oxford Instruments) attached for elemental detection. A thin layer of gold was sputtered (Electron Microscopy Sciences 575X) over the nanofiber samples at 20 mA for 30 seconds to minimize the charging before SEM. The obtained SEM image was imported to ImageJ software to measure the nanofiber diameter, which was calculated by averaging thirty unique measurements. The molecular and crystal structure were observed with a Thermo Scientific Nicolet iS10 FT-IR spectrometer and a PANalytical Empyrean X-ray diffractometer, respectively. Electrical conductivity of nanofiber mats was measured using a 4-point probe method with a Hewlett Packard 34401A multimeter to first measure the resistance (R in Ω). Four gold contact pads were sputtered onto a flat piece of nanofiber mat using a shadow mask. The sheet resistance, R_s , in Ω/sq , and electrical conductivity, σ , in S/cm , were then calculated using the following equations:

$$R = R_s \frac{L}{W} = \rho \frac{L}{Wt} \quad (\text{Equation 1})$$

$$\sigma = \frac{1}{\rho} \quad (\text{Equation 2})$$

Where ρ is the resistivity in Ωm ; L is the length between two adjacent contact pads in m ; W is the width of the entire nanofiber mat in m ; and t is the thickness of the nanofiber mat

in m. The L, W, and t of the nanofiber mat was measured using a digital caliper (General Tools 1433).

Specific surface area of pure PAN-derived carbon nanofibers was measured by BET method (Micromeritics ASAP 2020 Plus). Samples were degassed for 120 min at 200 °C to remove excess water, and nitrogen adsorption was used to determine the BET surface area.

2.3.2.5.2 Piezoelectric properties

Nanofiber samples were prepared similarly to work by Ico *et al.*⁹⁴ Briefly, As-spun PAN-derived pristine and composite nanofibers were cut from 35- μm nanofiber mat into 4 x 1.2 cm² strip. Two electrodes were made for each nanofiber sample to measure the voltage vertical to the direction of fiber length (V_{33}) and one parallel (V_{13}). A 7.2 x 1.6 x 0.01 cm³ brass substrate covered on both sides with polyimide tape was prepared as the cantilever. For electrodes to measure V_{33} , nanofiber sample was fixed to the center of the cantilever with double-sided copper tape, which served as the bottom-contact electrode, while the other side of the nanofiber was insulated with polyimide tape. For V_{13} samples, the nanofiber strip was fixed to the center of the cantilever, and the top and bottom edge of the nanofiber sample was electrically connected to two separate brass substrates with silver paste. A pair of 24-gauge wires were fixed to the contact, sealed with polyimide tape, then connected to a breadboard with inputs to a Picoscope 2204A™ (Pico Technology Ltd) to measure the absolute output voltage from the nanofiber mats.

The d_{33} coefficient was calculated using piezoelectric response from piezoelectric force microscopy (PFM) using the following equation:

$$d_{33} = \frac{A}{VQ} f \quad (\text{Equation 3})$$

Where A is the amplitude of the response; V is the applied voltage in V; Q is the quality factor of the AFM cantilever; and f is the correctional factor taken from the standard.

2.3.2.5.3 Electrochemical properties

All PAN-derived carbon nanofiber mats were cut into approximately 2 x 2 cm, onto which a Kapton washer tape with a 4-mm inner diameter was placed to reveal a working electrode area of 0.126 cm². Double-sided copper tape and conductive silver paste were used to extend the electrical contact from the nanofiber mat, and the entire electrode except for the working electrode area was covered with waterproof tape and microshield. Platinum-coated titanium strip was used as the counter electrode, Ag/AgCl (1 M KCl) as the reference electrode, and 0.1 M phosphate buffer saline (pH7.4) as the electrolyte. Multi-channel potentiostat (BioLogic/Princeton Applied Research VMP2) was used for all electroanalytical methods. UHP N₂ and air were supplied at 250 sccm into the electrolyte for deaeration and aeration, respectively. Each gas was bubbled into the electrolyte for at least 30 minutes before conducting the experiment, and a dissolved oxygen (DO) meter (Oakton WD-35643-12) was used to confirm the deaeration/aeration by measuring the concentration of DO in the electrolyte.

2.4 Results and Discussion

2.4.1 PAN nanofibers

2.4.1.1 Effect of DOE parameters on physical properties of nanofibers

2.4.1.1.1 Effect of solution conditions on solution and nanofiber properties

The solution conditions laid out by the 3-factor DOE are shown in Table 2.3. The small variation in the PAN wt.% stemmed from an established theory that viscosity of the solution majorly affects the nanofiber diameter.

The SEM images of collected PAN nanofibers shown in Figure 2.3 visually confirmed that sample 1, with 3.25 wt.% PAN and 0.1 wt.% BYK, was electrospun into the most consistent, smoothest nanofibers out of the 8 samples.

Table 2.3 Design of experiment varying solution parameters and their effects on solution and fiber properties. Electrospinning and environmental conditions were fixed at 15 kV, 1 mL/h, 23 °C, and 0.0105 kg H₂O/kg DA.

Sample	Code	Design factors			Solution properties			Fiber properties	
		PAN wt.%	PAN MW	BYK wt.%	Viscosity [cP]	Surface tension [dynes/cm]	Electrical conductivity [μ S/cm]	Average fiber diameter [nm]	Bead density [bead/ μ m ²]
1	+++	3.25	150,000	0.1	16.5	27	1.7	38 \pm 8	0.40
2	++-	3.25	150,000	0	16.5	41	1.7	53 \pm 13	0.99
3	+ - +	3.25	70,000	0.1	16.5	27	1.7	67 \pm 8	0.83
4	+ - -	3.25	70,000	0	16.5	41	1.7	59 \pm 7	1.3
5	- + +	3	150,000	0.1	15	27	1.7	64 \pm 11	0.52
6	- + -	3	150,000	0	15	41	1.7	54 \pm 7	0.72
7	- - +	3	70,000	0.1	15	27	1.7	x	x
8	- - -	3	70,000	0	15	41	1.7	x	x

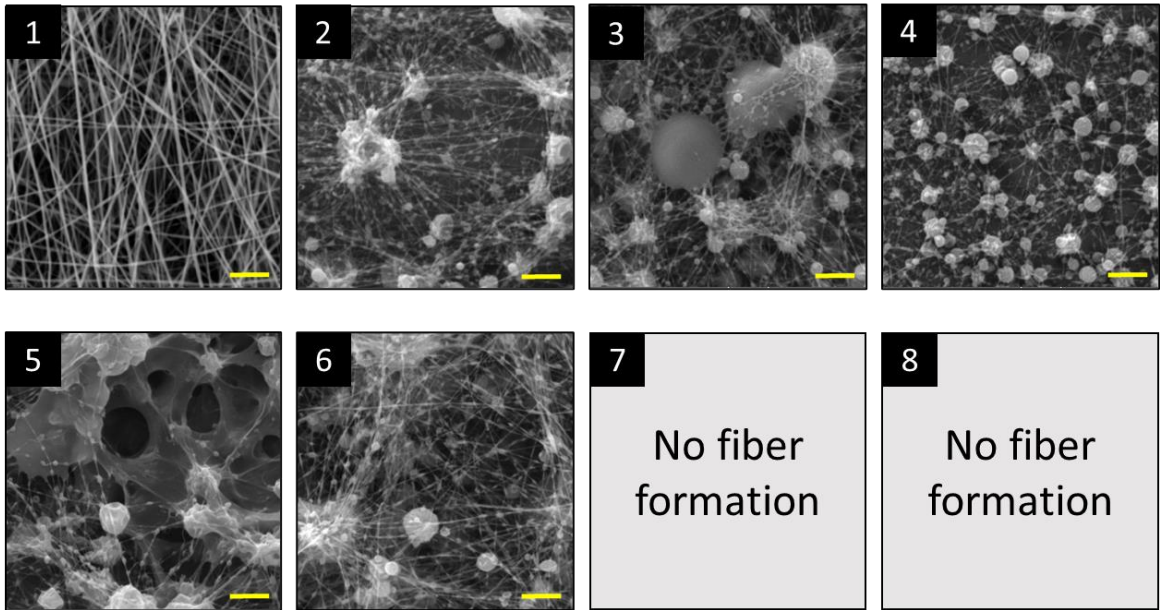


Figure 2.3 SEM images of electrospun PAN nanofibers from solutions in Table 2.3. Solutions that did not produce any quantifiable nanofibers are omitted. Scale bar 2 μm .

The measured solution properties, as well as fiber properties after electrospinning are shown in Table 2.3. Based on these properties, the effect of each parameter on the outgoing nanofiber dimensions and morphology were identified. DOE analyses shown in Figure 2.4 concluded that the three solution properties, viscosity, surface tension and electrical conductivity, were predominantly controlled by the PAN type – including concentration and molecular weight –, BYK concentration, and PF buffer concentration, respectively. This allowed for easy manipulation of the solution properties to study their effect on fiber properties.

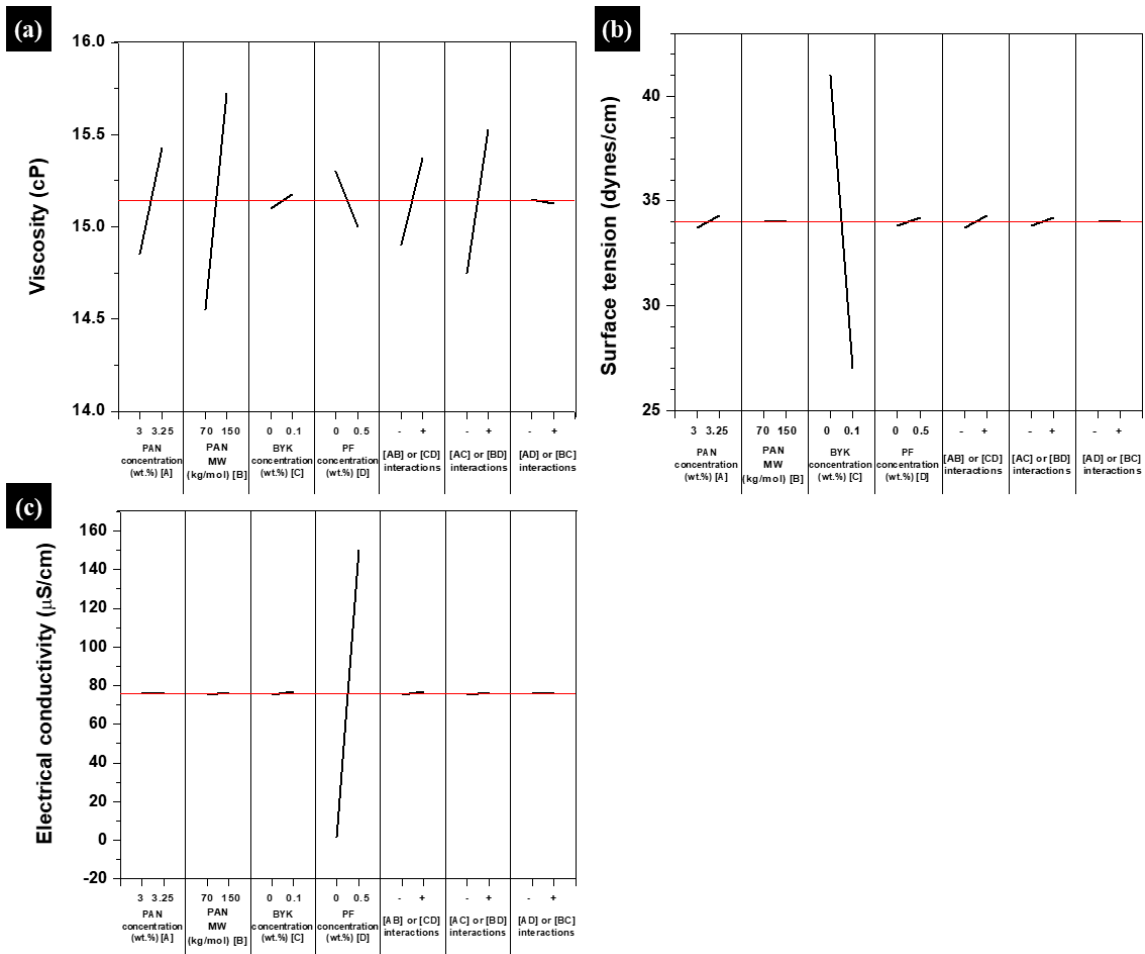


Figure 2.4 DOE analysis of (a) viscosity (b) surface tension (c) electrical conductivity as a function of various solution conditions.

DOE analysis on the effect of solution conditions on the average fiber diameter (Figure 2.5(a)) suggested that the choice of the PAN precursor, both concentration and molecular weight, was critical to the outgoing nanofiber diameter, while the surfactant concentration had negligible effect. Even the small 8% increase in PAN concentration would increase the viscosity of the solution, thereby resulting in a larger fiber diameter. The bead density, on the other hand, were shown to be mostly affected by the BYK concentration. (Figure 2.5(b)) The reduced surface tension by the presence of the surfactant

allowed for smoother and more stable stretching under the electric field, which produced less beads or other defects.

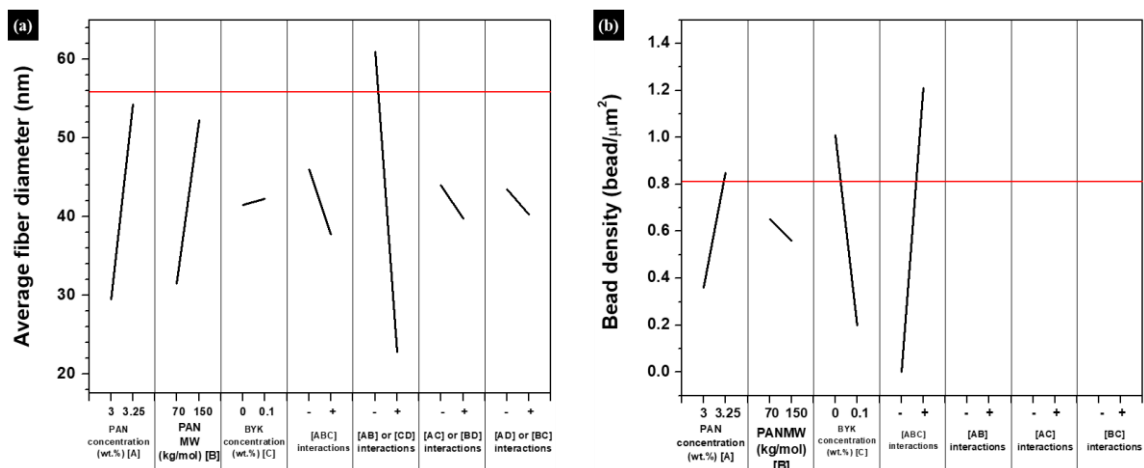


Figure 2.5 DOE analysis of (a) average fiber diameter and (b) bead density as a function of various solution parameters laid out in Table 2.3. Electrospinning conditions were fixed at 15 kV and 1 mL/h, and environmental conditions were fixed at 23 °C and 0.0105 kg H₂O/kg DA.

However, there seemed to be a certain threshold of PAN concentration in terms of stable formation of nanofibers. Even though 3 wt.% PAN solution had a lower viscosity than 3.25 wt.% PAN solution, it did not exhibit smaller fiber diameter. The nanofibers produced from sample 5 and 6 not only had high bead density, but also had clumping phenomenon. Furthermore, sample 7 and 8 did not produce any quantifiable nanofibers, suggesting that working parameters other than the solution conditions could affect the nanofiber formation process.

From the 3-factor solution condition DOE, it was concluded that 3.25 wt.% PAN, 0.1 wt.% BYK solution was the optimal recipe for producing smooth, bead-less nanofibers with minimum diameter. 2- factor electrospinning condition DOE was then employed

(Table 2.4) on this solution to further investigate the effect of working parameters on the electrospinning process.

2.4.1.1.2 Effect of electrospinning conditions on nanofiber properties

Table 2.4 Design of experiment varying electrospinning conditions and their effects on fiber properties. Solution conditions were fixed at 3.25 wt.% PAN (MW 150 kg/mol) and 0.1 wt.% BYK in DMF, and environmental conditions were fixed at 23 °C, 0.0105 kg H₂O/kg DA.

Sample	Code	Design factors		Fiber properties	
		Applied voltage [kV]	Feed rate [mL/h]	Average fiber diameter [nm]	Bead density [bead/ μm^2]
1	++	20	1	72 \pm 12	0.37
2	+-	20	0.75	76 \pm 14	0.54
3	-+	15	1	38 \pm 8	0.40
4	--	15	0.75	62 \pm 11	0.46

From the SEM images shown in Figure 2.6, it was not clear which electrospinning condition was optimal, since all four samples showed moderate beading effect, even though sample 3 exhibited significantly smaller fiber diameter compared to other three samples. DOE analyses of average fiber diameter and bead density (Figure 2.7) as a function of the electrospinning conditions showed that both applied voltage and feed rate had comparable effect on the fiber dimensions and morphology.

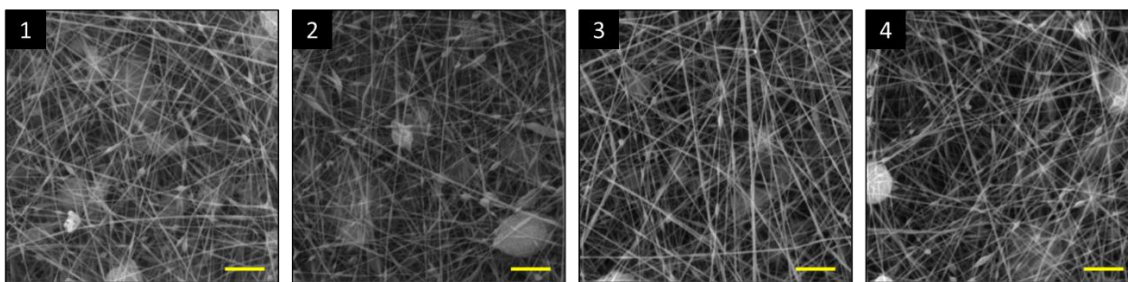


Figure 2.6 SEM images of electrospun PAN nanofibers from solutions shown in Table 2.4. Solution conditions were fixed on 3.25 wt.% PAN (MW 150,000) and 0.1 wt.% BYK in DMF, and environmental conditions were fixed at 23 °C, 0.0105 kg H₂O/kg DA. Scale bar 2 μm.

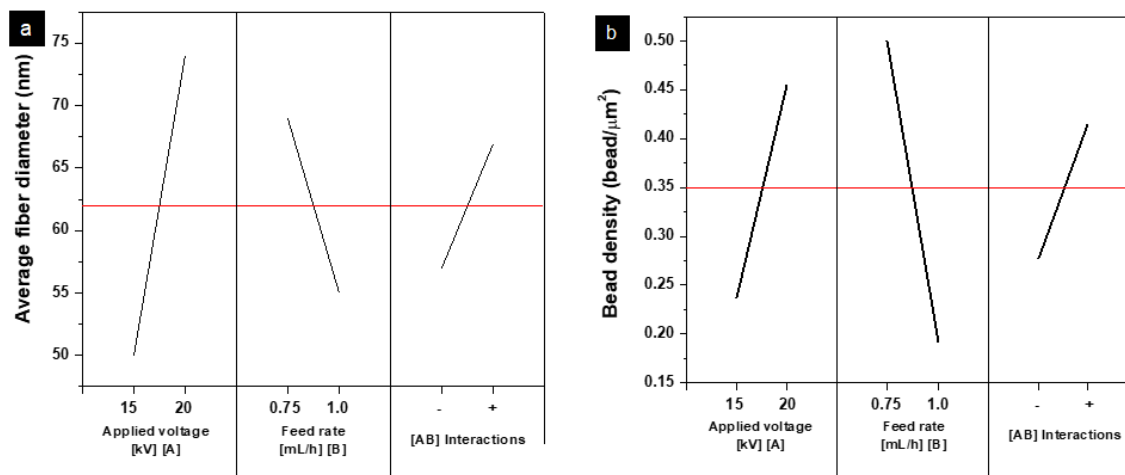


Figure 2.7 DOE analysis of (a) average fiber diameter and (b) bead density as a function of electrospinning conditions laid out in Table 2.4. Solution conditions were fixed at 3.25 wt.% PAN (MW 150,000) and 0.1 wt.% BYK in DMF, and environmental conditions were fixed at 23 °C and 0.0105 kg H₂O/kg DA.

2.4.1.1.3 Effect of applied voltage on nanofiber properties via Taylor cone formation

The applied voltage was varied in smaller increments to monitor its effect more closely. The strength of the electrical field created by the applied voltage controlled the degree of stretching of the solution into nanofibers. This phenomenon is described by the formation of a Taylor cone, which can only be achieved at a voltage slightly higher than the threshold voltage required to shape the round droplet at the end of the needle to a cone,

emitting a stable jet of nanofibers. If the applied voltage was too low (Figure 2.8(a)), the rate at which the solution is ejected exceeded the rate at which it was pulled into nanofibers, causing the solution to drip. If the voltage was too high (Figure 2.8(c)), the force by which the solution was stretched was too strong, which led to either unstable formation of Taylor cone, causing a high bead density, or drying up of the solution, clogging the needles. At an applied voltage of 15 kV and feed rate of 1 mL/h, the ejecting and stretching of the solution were at a stable equilibrium, forming smooth and consistent fibers. (Figure 2.8(b))

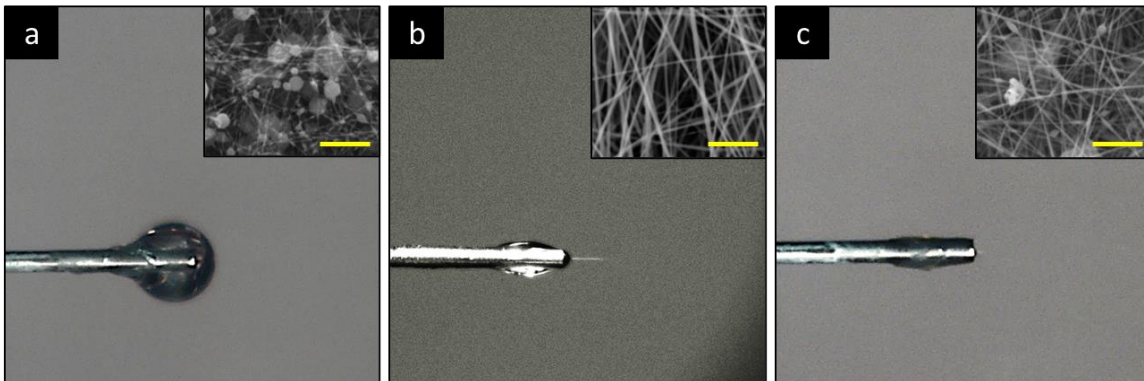


Figure 2.8 Images of PAN solution droplets under varying applied voltage. Inset: SEM image of nanofiber electrospun under the following applied voltage: (a) 5 kV; (b) 15 kV; (c) 25 kV. Shown in the image is of solution containing 3.25 wt.% PAN, 0.1 wt.% BYK in DMF, electrospun at 23 °C, 0.0105 kg H₂O/kg DA. Inset scale bar 2 μm.

2.4.1.1.4 Effect of environmental conditions on nanofiber properties

Another 2-factor DOE varying the environmental conditions was utilized for finer tuning of the working parameters. (Table 2.5) SEM images of the nanofibers collected at different temperatures and moisture content are shown in Figure 2.9.

Table 2.5 Design of experiment varying environmental conditions and their effects on fiber properties. Solution conditions were fixed on 3.25 wt.% PAN (MW 150,000), 0.1 wt.% BYK, and electrospinning conditions were fixed at 15 kV and 1 mL/h.

Sample	Code	Design factors		Fiber properties	
		Temperature [°C]	Absolute humidity [kg H ₂ O/kg DA]	Average fiber diameter [nm]	Bead density [bead/μm ²]
1	++	40	0.0140	72 ± 12	0.37
2	+-	40	0.0105	76 ± 14	0.54
3	-+	23	0.0140	38 ± 8	0.40
4	--	23	0.0105	62 ± 11	0.46

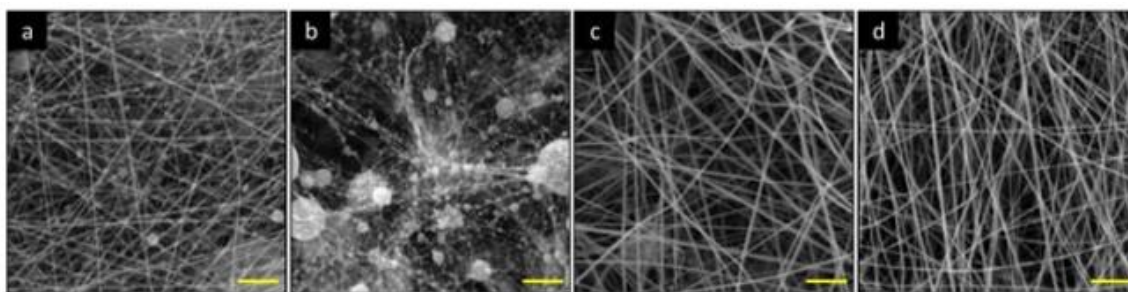


Figure 2.9 SEM images of electrospun PAN nanofibers from solutions shown in Table 2.5. DOE code (a) ++ (b) +- (c) -+ (d) --. Solution conditions were fixed on 3.25 wt.% PAN, 0.1 wt.% BYK, and electrospinning conditions were fixed at 15 kV and 1 mL/h. Scale bar 2 μm.

While the fiber diameter did not change significantly from 427 nm to 518 nm with increase in temperature, the bead density increased substantially. The high temperature possibly dried up the solution at the needle too quickly, resulting in unstable cone-jet formation. Also, lack of moisture at higher temperature accelerated the solvent evaporation, preventing sufficient stretching of the solution into smooth nanofibers. At 40 °C, the degree of bead formation subsided at higher moisture content of 0.0140 kg H₂O/kg DA, but the temperature was still too high for completely smooth nanofibers to form. DOE analysis in Figure 2.10 showed that both temperature and absolute humidity had a competing effect on the fiber diameter and bead density. Even though higher temperature

would lead to lower average fiber diameter, the dramatic increase in bead density as a function of temperature suggested that optimal environmental conditions were in between the upper and lower limits set by the DOE.

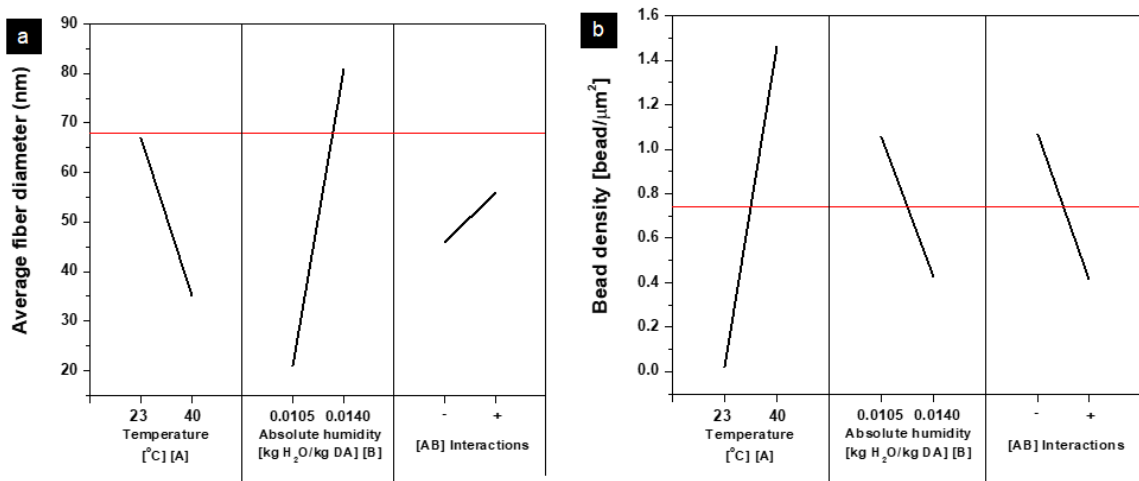


Figure 2.10 DOE analysis of (a) average fiber diameter and (b) bead density as a function of environmental conditions laid out in Table 2.5. Solution conditions were fixed on 3.25 wt.% PAN (MW 150,000), 0.1 wt.% BYK, and electrospinning conditions were fixed at 15 kV and 1 mL/h.

2.4.1.1.5 Electrical conductivity and BET surface area of PAN-based carbon nanofibers

Electrospun PAN nanofibers of various fiber diameters were heat treated in a two-step process: stabilization in air followed by carbonization in ultra-high purity nitrogen. Completion of each step was easily monitored by the color change of the nanofiber samples: white as-spun nanofibers turned to brown then black after each step of the heat treatment process.

Assuming that the nanofibers are solid cylinders, a simple inversely proportional relationship between the BET surface area and the nanofiber diameter can be established.¹¹⁸

Despite the initial hypothesis based on this relationship, the BET surface area shown in

Figure 2.11 revealed that it increased as a function of diameter instead. Compared to the literature values obtained for further insight, the data from this work followed the general trend.¹¹⁸⁻¹²⁰

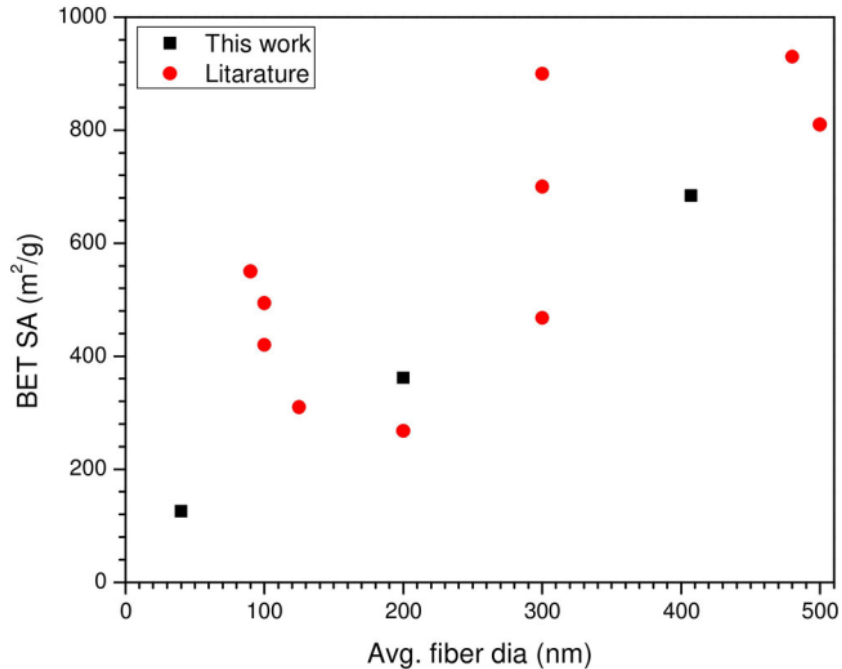


Figure 2.11 BET surface area as a function of average fiber diameter.

After the resistance was measured by the 4-point probe method, electrical conductivity was first calculated assuming no porosity using Equation 1 and 2. In order to account for the voids within the nanofiber mats, average void fraction was calculated. Based on the average void fraction of several unique samples, it was determined that the value ranged from 0.733 to 0.790 with less than 3% standard deviation for all average fiber diameters. Therefore, it was assumed that the average void fraction for all of the carbon nanofiber mats was 0.760 ± 003 , which was applied to all electrical conductivity values. As shown in Figure 2.12, the adjusted electrical conductivity of carbon nanofibers decreased with increasing fiber diameter. This trend was expected as the electrical

conductivity is inversely proportional to the cross-sectional area of the material, which increased as a function of average fiber diameter. Under the assumption that the resistivity and temperature were consistent for all carbonaceous samples, geometry would be the only factor affecting the electrical conductivity.

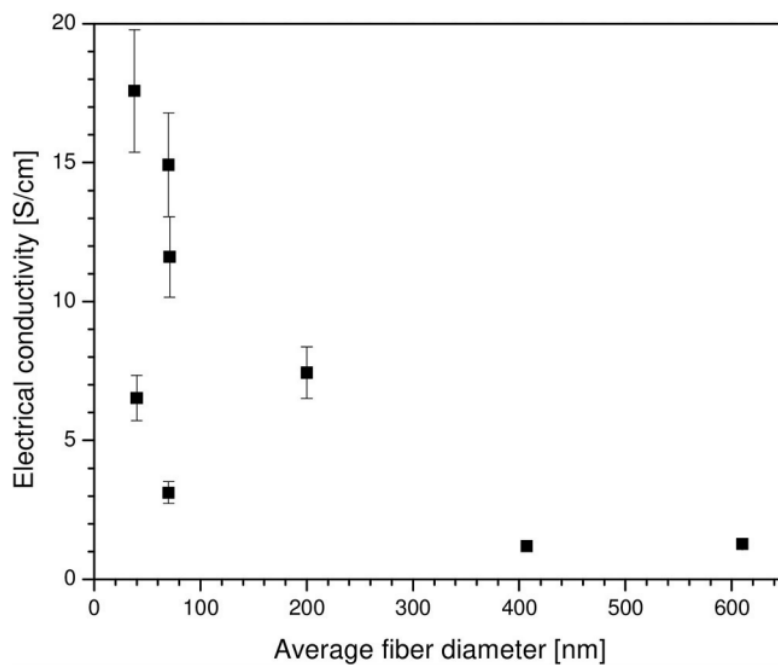


Figure 2.12 Electrical conductivity adjusted with nanofiber mat porosity as a function of average fiber diameter.

2.4.1.2 Electrochemical characterization of carbonized nanofibers

Carbonaceous nanofibers exhibit electrical conductivity orders of magnitude higher than that of polymeric nanofibers. Electrochemical performance of these nanofiber mats was characterized to further investigate their potential for electrode applications.

2.4.1.2.1 Cyclic voltammetry

Carbonized nanofibers were cut to create a circular working electrode (WE) with an exposed surface area of 0.13 cm^2 (diameter=0.2 cm). Cyclic voltammograms of prepared WEs in Figure 2.13 showed that the maximum value of both cathodic and anodic current increased as a function of scan rate, as expected. This phenomenon can be explained by the increase in diffusion layer thickness at the electrode-electrolyte with lower scan rate. The flux to the electrode surface is smaller when the size of the diffusion layer grows larger with slower scan rate. As current is proportional to flux, maximum current is thus the smallest at 1 mV/s, and largest at 100 mV/s. Furthermore, the voltammograms approached a rectangular shape at lower scan rates, suggesting an ideally capacitive behavior of the nanofiber mats.

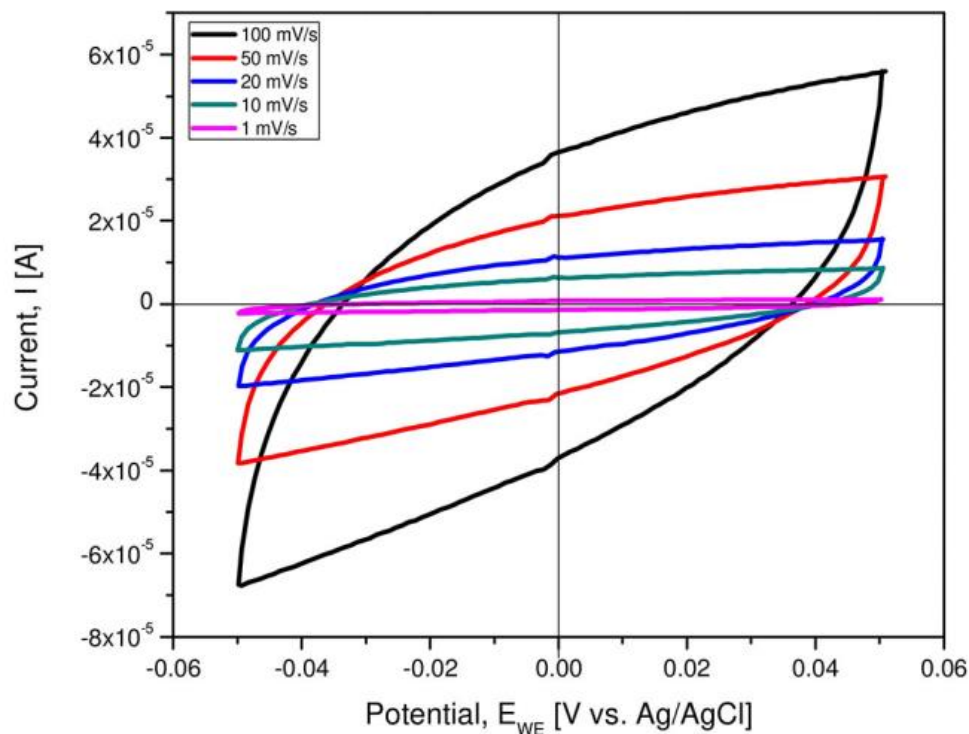


Figure 2.13 Cyclic voltammogram of carbonized nanofiber-based WE in pH 7.4 PBS at various scan rates. Average fiber diameter was 126 nm.

Gravimetric double-layer capacitance (C_g) of the WEs with different fiber diameters were calculated using the following equation:

$$C_g = \frac{A}{v \cdot m} \quad \text{(Equation 4)}$$

Where A is the area under the CV in $A \cdot V$, v is the scan rate in V/s , and m is the mass of the nanofiber mat WE in g.

The potential range of -0.05 to 0.05 V vs. Ag/AgCl was chosen after testing several different potential windows to find a suitable range for studying the capacitive behavior of the nanofiber mat WEs without any faradaic processes. Furthermore, this potential window

avoided hydrogen and oxygen gas evolution reactions, which would cause bubbling of these gases that interfere with the electrolyte-electrode interface.

2.4.1.2.2 Electrochemical impedance spectroscopy and double-layer capacitance of carbonaceous nanofiber mat electrodes

Electrochemical impedance spectra were obtained with the same three-electrode setup as the CV. (Figure 2.14) The solution resistance indicated by the x-intercept of the spectra was consistent at approximately 109Ω for all three carbonaceous nanofiber mat WEs. All three of the carbonized nanofiber mat electrodes exhibited no semicircle, which suggested negligible charge transfer resistance.¹²¹ The slope of the spectra increased as a function of average fiber diameter, which could be attributed to the increasing BET surface area of larger nanofibers, resulting in higher double-layer capacitance effect. As ideal capacitor would exhibit a vertical line in an EIS, it can be concluded precise control of the nanofiber diameter could yield a suitable nanofiber mat for electrode applications.

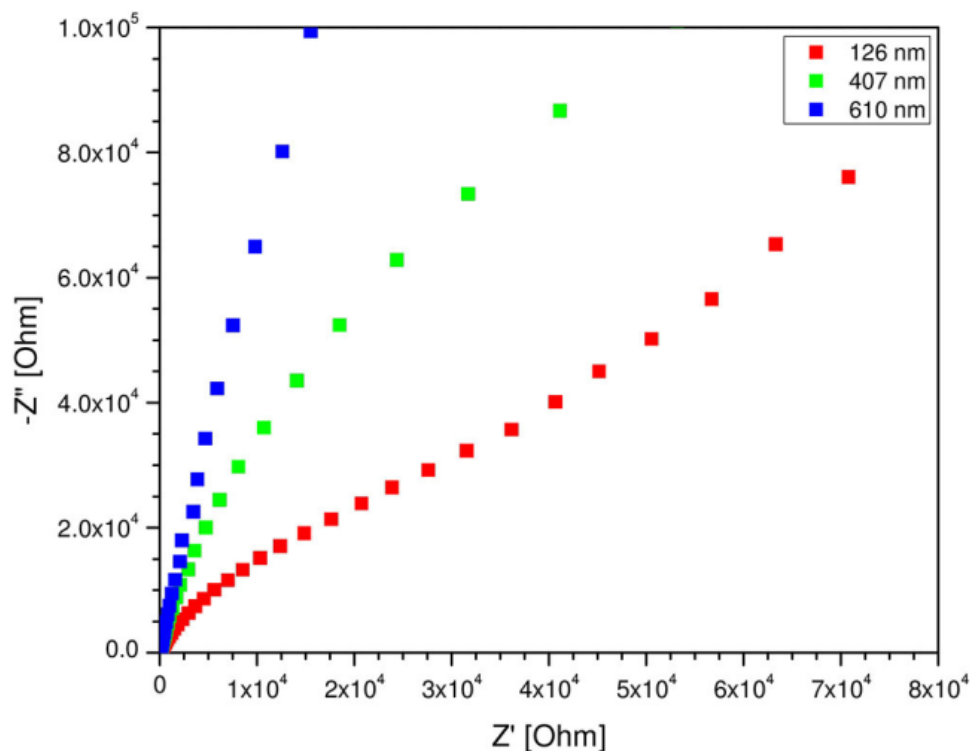


Figure 2.14 Electrochemical impedance spectra of carbonized nanofiber-based WE in pH 7.4 PBS.

At a fixed scan rate of 10 mV/s, C_g of the carbonaceous nanofiber mat WE increased by four orders of magnitude as the average nanofiber diameter decreased from 610 to 126 nm, as shown in Figure 2.14. While the BET data has shown that the specific surface area decreased with lower nanofiber diameter, it is possible that there was a larger void in between the nanofibers available for 126-nm nanofiber WE than for 610-nm nanofiber WE, which would increase the access for the electrode-electrolyte interaction and thus allow for larger capacity to hold charges.

C_g of the same carbonaceous nanofiber mat electrodes was calculated using EIS method. By fitting the Nyquist plot of each spectrum to a simple circuit consisting of capacitor (electrode) and resistor (solution resistance), parameters required to calculate the

capacitance were obtained. The gravimetric capacitance calculated by both methods were comparable, and the trend in which the capacitance increased as the nanofiber diameter was reduced was consistent, as shown in Figure 2.15. However, multiple use of the same WE in aqueous systems resulted in disintegration of the nanofiber mat, suggesting the durability and other mechanical properties of the carbonaceous nanofiber mats would require further modification for optimal application in real life.

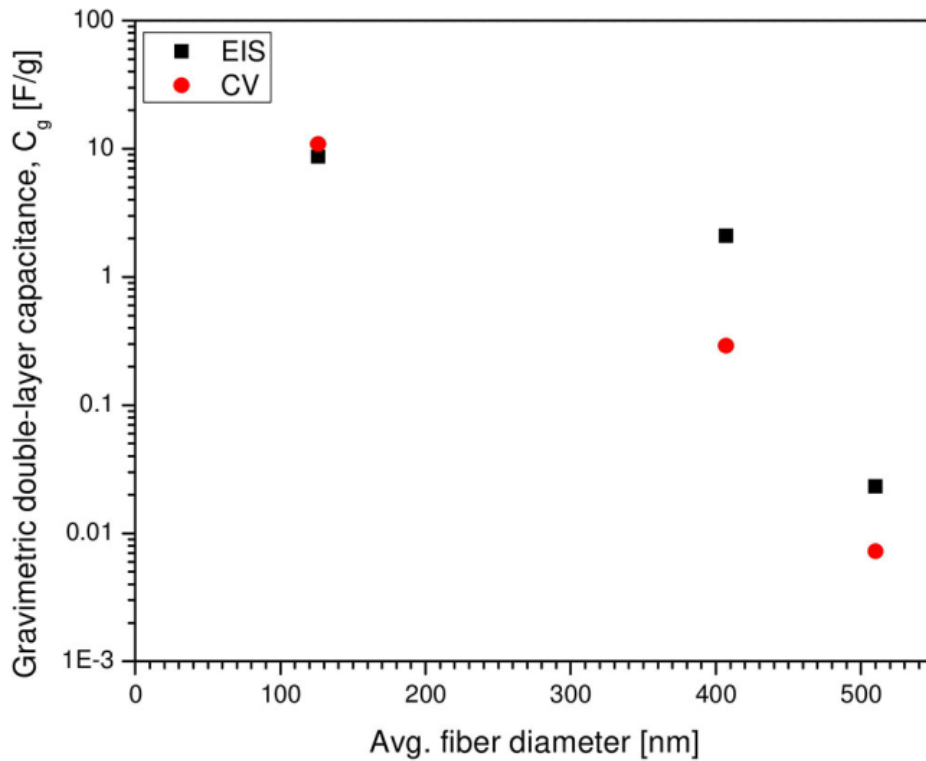


Figure 2.15 Gravimetric double-layer capacitance of carbonized nanofiber mats as a function of their fiber diameter.

2.4.1.3 Piezoelectric characterization of PAN nanofibers

Since the discovery of polyvinylidene fluoride (PVDF) in the 1960s, piezoelectric polymers have gained much research interest as a lead-free, flexible alternative to ceramics

such as lead zirconate titanate (PZT).²⁰ Piezoelectric properties of polyacrylonitrile (PAN) was also studied¹²², but its research effort lacked heavily compared to PVDF and PVDF-TrFE due to difficulty of poling, which was proposed to be related to the strong dipole-dipole interaction of the nitrile groups between the same molecule.¹²³ However, it was shown that stretching the PAN polymer to multiple times its length could enhance the polarization by facilitating the polymer chains to pack via the intermolecular dipole.¹²⁴ With the help of electrospinning, polymer solutions can be stretched into nanofibers, which are known to have ultra-high aspect ratios. In addition, the high electric field applied during the electrospinning process eliminates the need for post-poling. Even so, there has yet been a study elucidating the piezoelectric properties of PAN nor its enhancement, and only a handful of publications were found showcasing the feasibility of piezoelectric energy harvesting with PAN.^{29,30,52,125} Though these works have shown some type of voltage output by applying pressure to randomly oriented PAN nanofiber mats, no clear correlation between the piezoelectric properties of PAN to the voltage was made.

Table 2.6 Solution and nanofiber properties of various electrospun samples. 0.1 wt.% BYK was added to every solution. All electrospinning and environmental conditions were fixed.

PAN wt. %	Solution properties			Nanofiber properties			
	Viscosity [cP]	Surface tension [dynes/cm]	Electrical conductivity [μ S/cm]	Average nanofiber diameter [nm]	Bead density [bead/ μ m ²]	Fiber fraction [μ m ² / μ m ²]	Alignment fraction [%]
3.25	16.5	27.0	1.70	36 \pm 20	0.38	0.864	40
4	46	27.0	1.70	61 \pm 24	0.48	0.901	40
6	97.6	26.8	1.70	200 \pm 30	0	1.00	52
8	195.2	27	1.69	298 \pm 38	0	1.00	60
10	330	27.3	1.70	521 \pm 98	0	1.00	64

Solution and nanofiber properties of as-spun, aligned PAN nanofibers are listed in Table 2.6. For proper characterization of the piezoelectric properties of PAN nanofibers,

the rotational speed of the ground collector was increased from the typical 400 to 2000 rpm to align the nanofibers. Higher rotational speed of the ground collector elongated the nanofibers more before the solvent evaporated, leading to slightly lower nanofiber diameter in most cases when compared to PAN nanofibers electrospun at 400 rpm. Nevertheless, the average nanofiber diameter increased linearly as a function of viscosity with R^2 value of approximately 0.98 (Figure not included). As shown in Figure 2.16, nanofibers electrospun from solutions with the two lowest viscosities (i.e. 3.25 and 4 wt.% PAN) exhibited some beading as well as fiber fraction lower than 0.95, which was considered as the threshold for defect-free nanofibers in this work. Furthermore, these two samples had the lowest alignment fraction (i.e. 40%), which represented the percentage of nanofibers at 0 to 10° from the vertical axis. This was attributed to the fact that thin nanofibers such as 36 and 61 nm in diameter could not withstand the high tangential velocity (i.e. approximately 13 m/s) as they approached the disc collector rotating at high speed. In fact, as the average nanofiber diameter increased from 200 to 521 nm, higher alignment fraction up to 64% was observed.

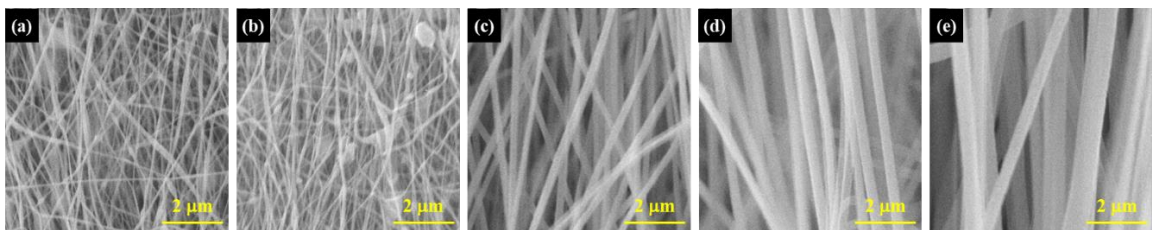


Figure 2.16 SEM images of (a) 3.25 wt.% (b) 4 wt.% (c) 6 wt.% (d) 8 wt.% (e) 10 wt.% PAN nanofibers electrospun at 2000 RPM.

A couple of hypotheses were set up prior to the piezoelectric properties characterization: (i) the high electric field applied during electrospinning would polarize

the polymer chain by aligning the CN triple bond to one side, forming an “electrospun phase”, which would exhibit enhanced piezoelectric properties compared to bulk or other nanomaterial counterparts; (ii) fine tuning of conditions to control the size and crystallinity of PAN nanofibers would further enhance the piezoelectric properties.

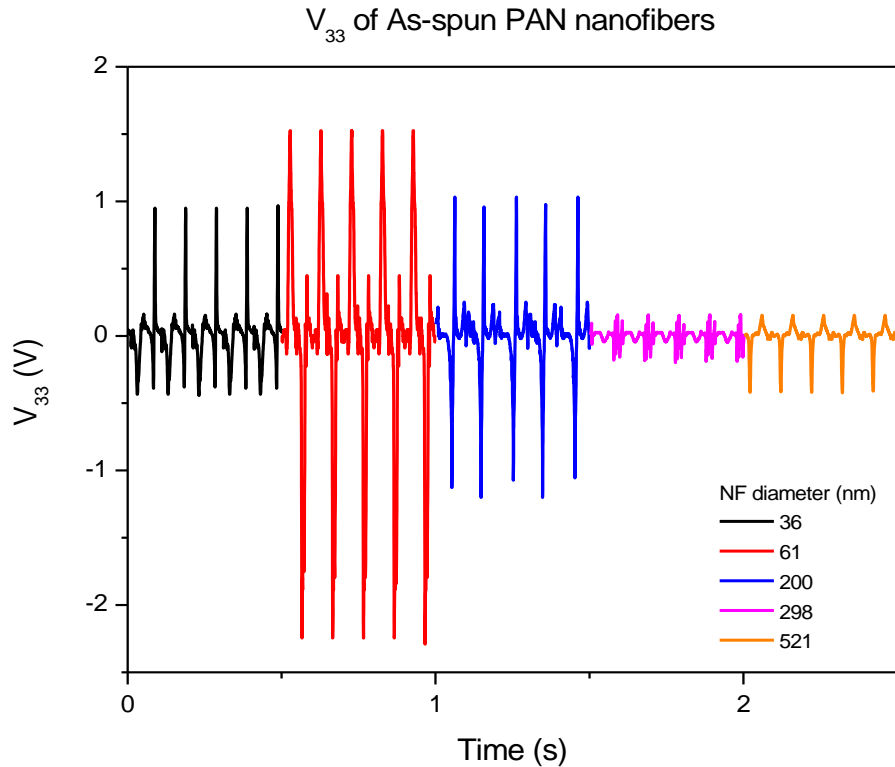


Figure 2.17 V_{33} of as-spun PAN nanofibers with various diameters. All measurements were taken at room temperature.

Typical piezoelectric response of various PAN nanofibers measured in V_{33} at room temperature is shown in Figure 2.17. As expected, significant increase in the voltage output was observed as the nanofiber diameter decreased from 298 to 61 nm. Though 36-nm nanofiber did not exhibit the largest voltage output, this could be described by the low fiber fraction, as approximately 14% of the sample was occupied by clumps and beads, which hindered uniform charge separation. Similarly, it could explain the fact that the nanofiber

with the highest diameter (i.e. 521 nm) output slightly higher V_{33} than 298 nm because of its high alignment fraction in addition to smooth, defect-free morphology. To further explain the size- and morphology-dependent piezoresponse, structural characterization such as FT-IR and XRD would be required to correlate with the molecular structure and change in degree of crystallinity as a function of nanofiber dimensions. Borrowing from previous works on other piezoelectric polymers such as P(VDF-TrFE), systematic variation of the solution conditions to control the resulting nanofiber diameter showed exponential increase in the piezoresponse as a function of decreasing nanofiber diameter.⁹⁴ This work by G. Ico et al. attributed this to the higher amount of electroactive phase in electrospun P(VDF-TrFE) compared to thin films, which further increased with smaller nanofiber dimensions. Furthermore, the increase in degree of crystallinity with decreasing nanofiber diameter was suggested to contribute to enhanced piezoelectric properties with higher ordered microstructure of the polymer chains. Similar observations are expected for PAN nanofibers to describe the size-dependent increase in piezoresponse.

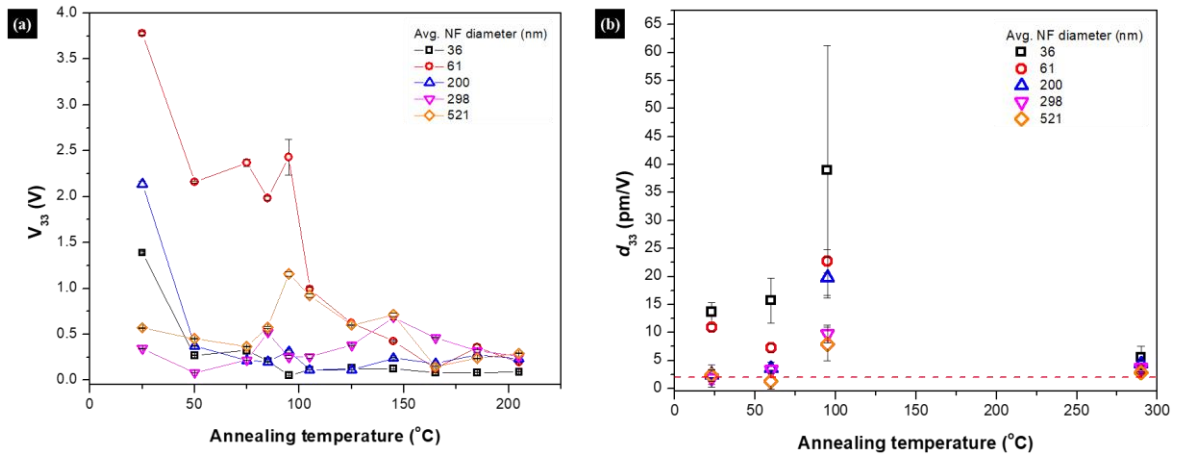


Figure 2.18. Effect of annealing temperature on (a) V_{33} and (b) d_{33} of PAN-derived nanofibers of various sizes. Five unique V_{pp} measurements were taken to calculate the average V_{33} . The red dashed line indicates literature value.

The as-spun aligned PAN nanofibers were annealed at various temperatures for one hour to induce change in crystallinity and eventually the molecular structure, which would correlate with change in piezoelectric properties. As shown in Figure 2.18(a), V_{33} of PAN nanofibers of all sizes decreased as a function of temperature, with a dramatic reduction in the voltage output at 50 °C followed by a steady decline. For the 61-nm nanofiber sample which exhibited the largest reduction in V_{33} response, it was clearer that the piezoresponse decreased dramatically again at 105 °C followed by another steady decline up to 205 °C. While the degradation of piezoelectric properties of PAN was expected with temperature due to the loss of the polar CN triple bond, it was initially hypothesized that the piezoelectric properties would be enhanced up to the glass transition temperature (T_g) of 95 °C, at which the polymer would transition to a “rubbery” state, leading to higher dielectric permittivity.¹²⁶ Unfortunately, it was not clear why the voltage output did not follow this trend, especially since the piezoelectric charge constant (d_{33}) did enhance until 95 °C, after which it decreased to a value below those measured at room temperature for all nanofiber diameters. (Figure 2.18(b)) However, it is important to note these values still exceeded that of literature value.⁵² Typically, at around 290 °C, PAN undergoes a cyclization process, during which one of the bonds in the nitrile group is broken to form a cyclical structure along the polymer chain. This structural change was observed by FT-IR; in Figure 2.19, three peaks and a shoulder at 1450, 2253, 2942, and 2864 cm^{-1} were detected for as-spun PAN nanofibers, whereas 2 different peaks at 1396 and 1609 cm^{-1} were observed for cyclized (or stabilized) PAN.

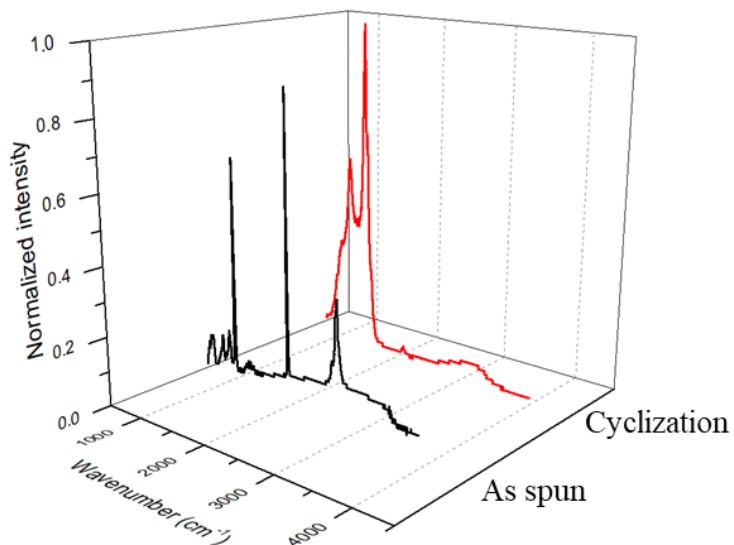


Figure 2.19 FT-IR spectra of as-spun and annealed (cyclized) PAN-derived nanofibers. Cyclization was conducted at 280 °C.

Peak assignment to functional groups is summarized in Table 2.7, which shows the peaks detected for as-spun PAN nanofibers represented the characteristic groups such as nitriles and CH₂ bending and stretching, while those for stabilized PAN represented C=C and C=N stretching as well as C-H stretching, indicating the loss of one of the CN triple bonds and one of the CH₂ bonds. Further investigation into the change at the molecular and crystal level over the temperature range with finer increments could help to provide more insight.

Table 2.7 Peak assignment from FT-IR for as-spun and stabilized PAN-derived nanofibers.

Step	Wavenumber [cm ⁻¹]	Product assignment
As spun	1450	CH ₂ bending
	2243	C≡N symmetric stretching
	2942	CH ₂ asymmetric stretching
	2864	CH ₂ symmetric stretching
Stabilization	1396	C-H stretching
	1609	C=C and C=N stretching

Piezoelectric response in the form of V_{13} , on the other hand, showed a slightly different trend, in which the 200-nm nanofibers exhibited the highest voltage output. This could be because the two smaller nanofibers (i.e. 36 and 61 in diameter) were simply too fragile to withstand the stretching motion. In fact, the samples were brittle and difficult to handle, and showed degradation faster than those with larger diameters. Combined with lower fiber and alignment fraction, 36- and 61-nm nanofiber samples might require further testing to consider the data at this time. For the three larger nanofibers (i.e. 200, 298 and 521 nm in diameter), typical trend of increase in piezoresponse as a function of decreasing nanofiber diameter was observed.

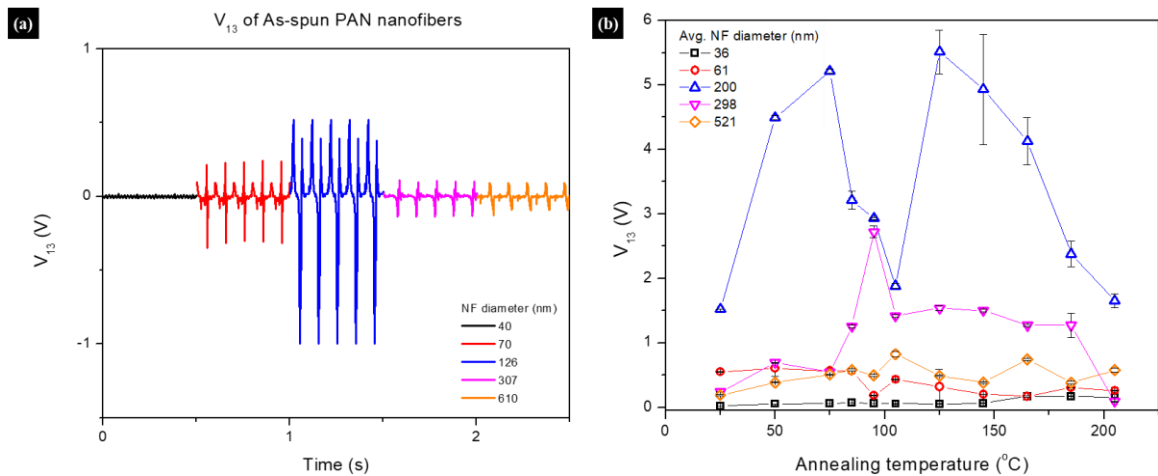


Figure 2.20. (a) V_{13} of as-spun PAN nanofibers with various diameters. (b) Effect of annealing temperature on V_{13} of PAN-derived nanofibers of various sizes. Five unique V_{pp} measurements were taken to calculate the average V_{13} .

2.4.2 PAN/MWNT nanofibers

2.4.2.1 DOE analysis on solution properties and morphology of as-spun PAN/MWNT nanofibers

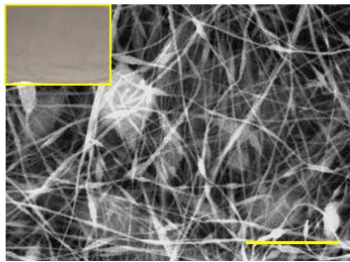
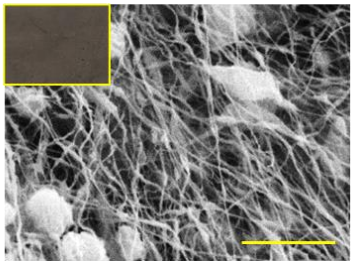
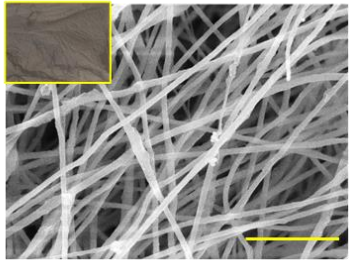
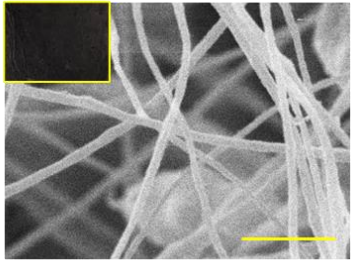
Table 2.8. Solution and nanofiber properties of various PAN/MWNT samples. 0.1 wt.% BYK was added to every solution. All electrospinning and environmental conditions were fixed.

DOE code	Design factors		Solution properties			Nanofiber properties		
	PAN wt. %	MWNT wt. %	Viscosity [cP]	Surface tension [dynes/cm]	Electrical conductivity [μ S/cm]	Average nanofiber diameter [nm]	Bead density [bead/ μ m ²]	Fiber fraction [μ m ² / μ m ²]
--	4.5	0.45	45.8	21.9	27.6	152	0.02350	0.974
+-	7	0.7	289.1	19.7	52.23	437 \pm 83	0.00087	0.983
++	4.5	2.25	85.0	22.3	56.28	174	0.00389	0.968
++	7	3.5	690.6	19.7	78.4	721 \pm 121	0	0.941

PAN/MWNT composite nanofibers were fabricated according to the design of experiment factors laid out in Table 2.8, where the solution and nanofiber properties of each sample are also laid out. As seen in Table 2.9, nanofibers with 7 wt.% PAN were

much smoother and uniform in diameter compared to those with 4.5 wt.% PAN, with less beading or clumps caused by some MWNT aggregates. The inset images shown in Table 2.9 visually confirms the increase in absolute MWNT loading with darker color of the as-spun nanofiber mat.

Table 2.9. SEM images of PAN/MWNT/BYK nanofibers fabricated according to DOE. Inset shows optical image of the nanofiber mat. Scale bar 5 μm .

PAN:MWNT (by wt.%)		-		+	
		-		+	
PAN wt.%		-		+	
	-				
	+				

DOE analysis on the effect of the DOE factors on the solution properties shown in Figure 2.21 showed that while the PAN wt.% was still the predominant factor affecting the solution viscosity, as explained in section 2.4.1.1.1, the MWNT loading also had a positive effect in increasing viscosity.

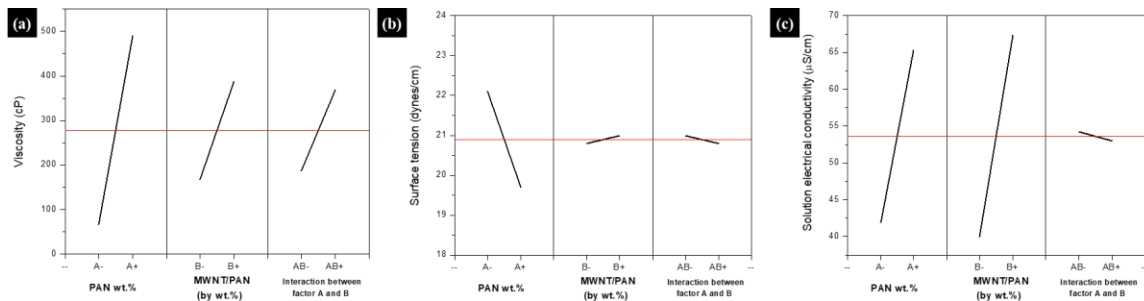


Figure 2.21. DOE analyses of (a) viscosity; (b) surface tension; and (c) solution electrical conductivity as a function of DOE factors laid out in Table 2.8.

Surface tension, as expected, was not significantly affected by either of the factors or their interactions. Figure 2.21(c) seemed to suggest that the PAN wt.% had a significant impact on increasing the solution electrical conductivity. However, it is important to note that as PAN wt.% was increased according to the DOE, so did the absolute amount of MWNT in the solution, as the regulated factor was the ratio between MWNT wt.% and PAN wt.%. Therefore, it was drawn from this analysis that the overall loading of MWNT in the solution predominantly affected the solution electrical conductivity due to its metallic properties. As the average response of the nanofiber diameter to the DOE factors coincide with that of the solution viscosity (Figure 2.22(a)), that the trend of the solution viscosity mainly affecting the nanofiber diameter was consistent even when a composite material (i.e. MWNT) was added to the polymer.

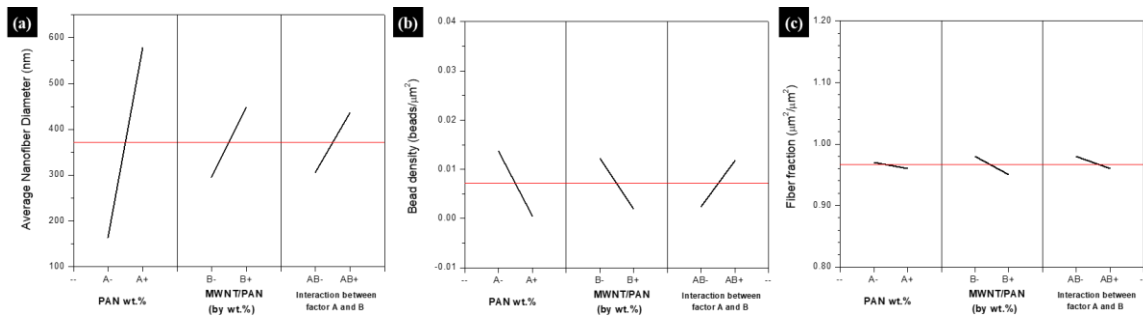


Figure 2.22. DOE analyses of (a) average nanofiber diameter; (b) bead density; and (c) fiber fraction as a function of DOE factors laid out in Table 2.8. Electrospinning conditions were fixed at 15 kV, 1 mL/h, and environmental conditions were fixed at 23 °C, 0.0105 kg H₂O/kg DA.

Though the bead density nor the fiber fraction was significantly controlled by either of the DOE factors, it can be seen in Figure 2.22(b) that the bead density was slightly decreased as a function of both DOE factors, agreeing with the optical observations shown in the SEM images. Furthermore, when the real experimental data were compiled for PAN and PAN/MWNT composites to plot nanofiber diameter as a function of solution conditions (Figure 2.23(a)) and solution properties (Figure 2.23(c)), nanofiber diameter generally followed a linear increase as a function of both PAN wt.% and solution viscosity in both absence and presence of MWNT. The strong correlation between the solution viscosity, controlled by the polymer concentration, and the nanofiber diameter was clear in the contour plots (Figure 2.23(b) and (d)), where the color gradation indicating the nanofiber diameter was almost vertical to the x-axis (i.e. PAN wt.% in Figure 2.23(b) and solution viscosity in Figure 2.23(d)).

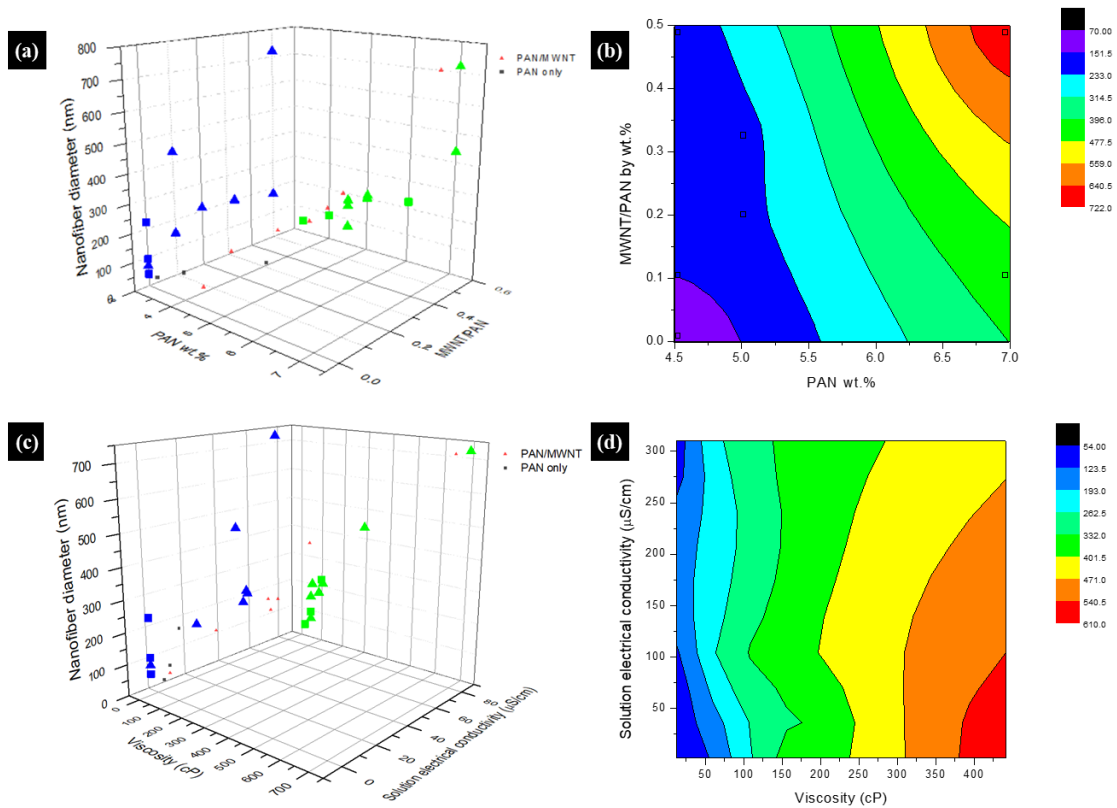


Figure 2.23. (a) 3D scatter plot and (b) contour plot of average diameter of PAN/MWNT nanofibers as a function of PAN wt.% and MWNT-to-PAN ratio by wt.% (c) 3D scatter plot and (d) contour plot of average diameter of PAN/MWNT nanofibers as a function of solution viscosity and electrical conductivity.

2.4.2.2 Piezoelectric properties of as-spun PAN/MWNT nanofibers

Voltage output of PAN/MWNT composite nanofibers in 3 (V_{33}) and 1 (V_{13}) direction in response to strain in 3 direction was measured similar to PAN nanofibers in Section 2.4.1.3. In Figure 2.24, V_{33} of as-spun PAN nanofibers at room temperature was 5-7 times higher than that of either PAN/MWNT nanofibers.

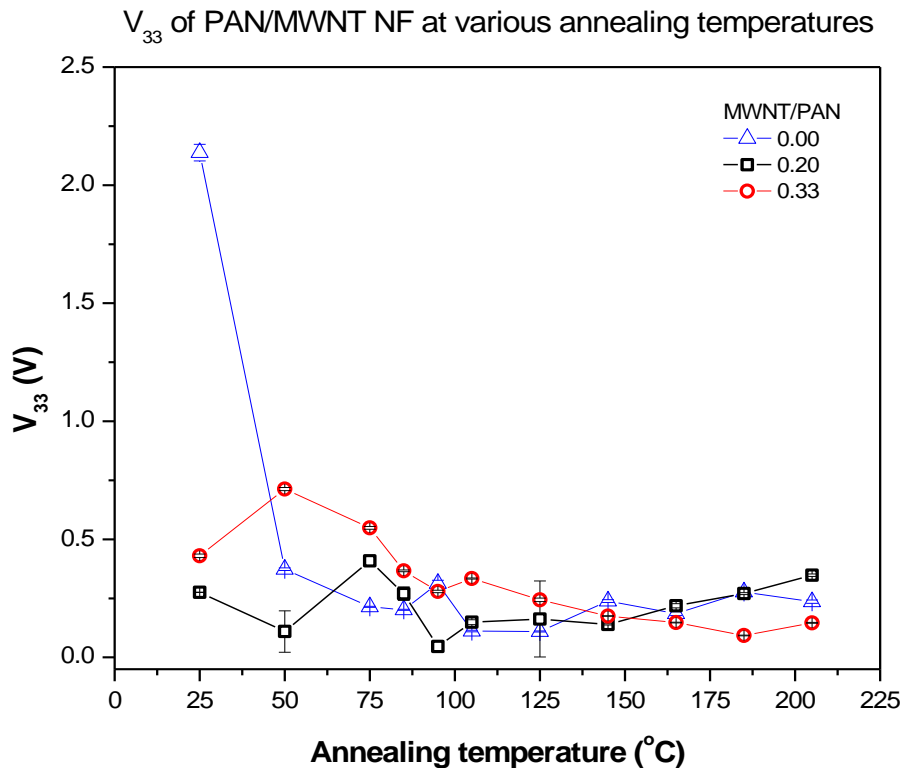


Figure 2.24 Effect of annealing temperature on V_{33} of PAN- and PAN/MWNT-derived nanofibers of various sizes. Five unique V_{pp} measurements were taken to calculate the average V_{33} .

While V_{33} of PAN nanofibers decreased significantly to ~17% of that measured as-spun upon annealing at 50 °C followed by consistent reduction down to 0.24 V at 205 °C, neither samples with MWNT loading of 0.20 nor 0.33 showed discernable trend as a function of temperature. It might be worth noting that V_{33} value of 5PAN/1.67MWNT

nanofibers annealed at 205 °C was approximately 34% of as-spun, as expected by the loss of the polar CN group in PAN polymer chain. Though the degree of reduction in the V_{33} value was not as significant as PAN nanofiber of similar diameter, this could be explained by the presence of metallic MWNT interfering with uniform charge separation across the piezoelectric PAN. For 5PAN/1MWNT nanofibers, on the other hand, the V_{33} at 205 °C turned out to be higher than that measured as spun; this might be attributed to low fiber or alignment fraction, which need to be confirmed.

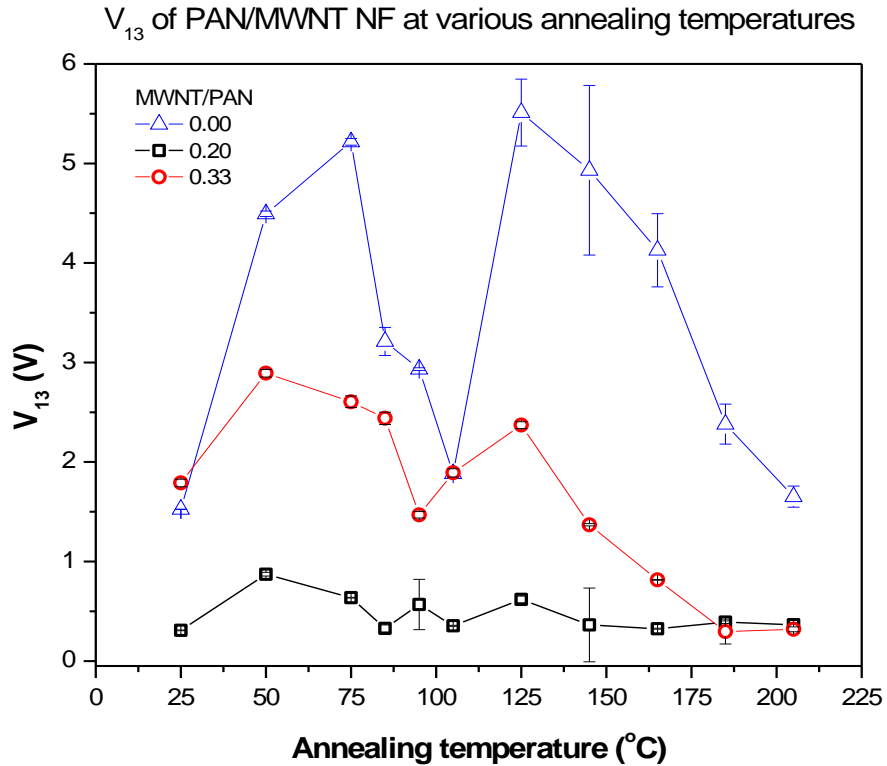


Figure 2.25 Effect of annealing temperature on V_{13} of PAN- and PAN/MWNT-derived nanofibers of various sizes. Five unique V_{pp} measurements were taken to calculate the average V_{13} .

In the case of V_{13} as a function of annealing temperature (Figure 2.26), all three nanofiber samples seemed to follow a similar trend, in which V_{13} exhibited an increase towards the glass transition temperature (T_g) of PAN (95 °C), followed by a dip at temperatures slightly above T_g ; then an increase up to 125 °C; finally a decrease as a function of temperature all the way to 205 °C. Again, the degree of change in V_{13} values were not as significant for either PAN/MWNT nanofibers compared to purely PAN-derived nanofibers, as the piezoelectric effect might have been hindered by the metallic MWNT. However, between MWNT loading of 0.20 and 0.33, both V_{33} and V_{13} values were higher for the PAN/MWNT nanofibers with larger MWNT loading. This might be due to the metallic properties of MWNT contributing to the electrical conductivity of the nanofiber mat, allowing for more efficient charge transfer across the sample. Similar to the Section 2.4.1.3, additional experiments such as FTIR and XRD would be required to provide further insight on the change in the piezoelectric properties of PAN/MWNT nanofibers as a function of MWNT loading.

2.4.2.3 Characterization of carbonized PAN/MWNT-derived nanofibers

In order to study the effect of the addition of MWNT to the physical and electrochemical properties of carbonaceous PAN-derived nanofibers, PAN/MWNT composite nanofibers were put through a two-step heat treatment: stabilization in air at 280 °C followed by carbonization in an inert environment, i.e. ultra-high purity nitrogen (UHP N_2), at 1000 °C. Nanofiber diameter decreased after each step of heat treatment, reaching ~70% lower than that before heat treatment.

Similar to how the electrical conductivity of carbonaceous PAN-derived nanofibers was calculated, averaged void fraction of 0.76 was accounted for when calculating the electrical conductivity of MWNT-embedded carbonaceous nanofibers via 4-point probe measurement of nanofiber mat resistance. When plotted as a function of nanofiber diameter and MWNT-to-PAN weight ratio for both PAN- and PAN/MWNT-derived carbon nanofibers, electrical conductivity showed to be predominantly controlled by the nanofiber diameter, indicated by the significant increase as the diameter is reduced from 200 nm to sub-100 nm range. (Figure 2.26)

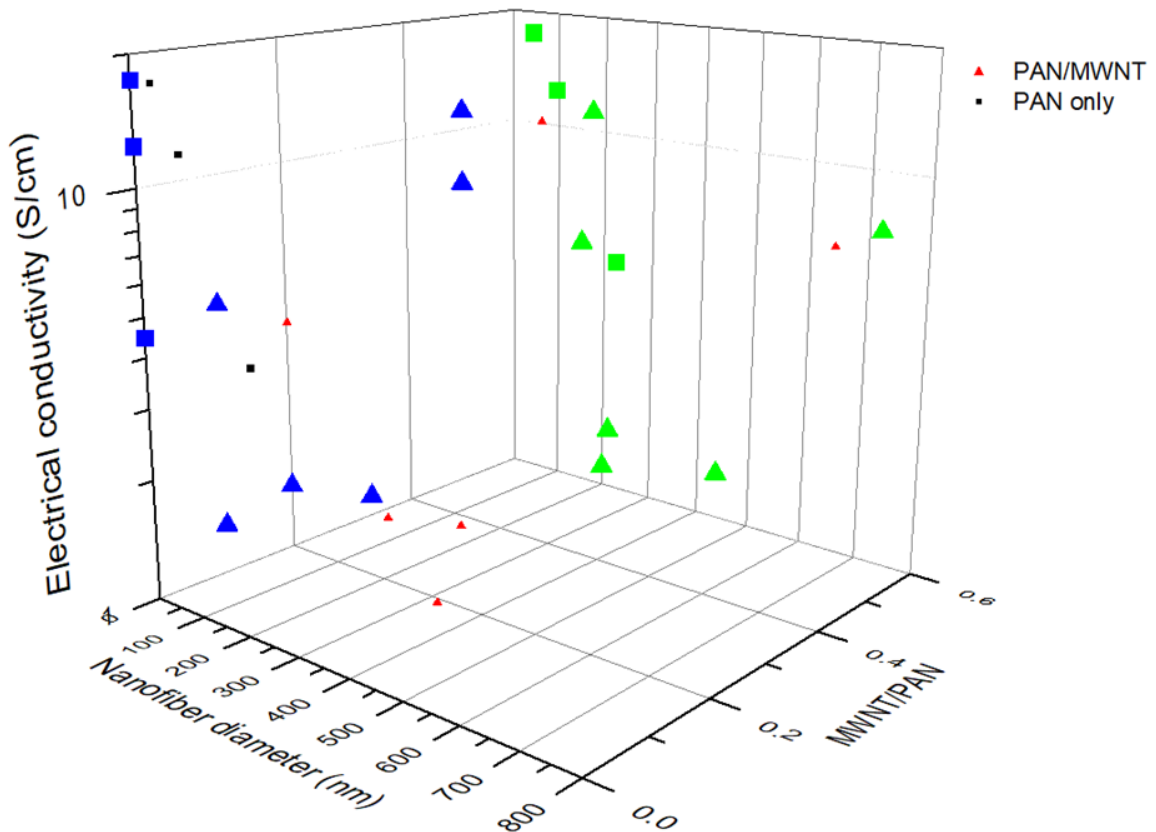


Figure 2.26 Electrical conductivity of carbonized PAN- and PAN/MWNT-derived nanofibers as a function of nanofiber diameter and MWNT-to-PAN ratio by wt.%.

The electrical conductivity of PAN/MWNT-derived carbon nanofibers as a function of MWNT loading generally followed a percolative behavior, in which the electrical conductivity sharply increased after a certain critical concentration of the conductive MWNT in the nanofibers.¹²⁷ Though the exact percolation threshold was not determined, the drastic increase in electrical conductivity was observed at ~2 vol.% MWNT. This value was slightly higher than literature values,^{128–130} which could be explained by the aggregation of the MWNT.

MWNT-embedded carbonaceous nanofibers (CNF) with fixed amount of PAN were fabricated into working electrodes for electrochemical characterization of the nanofiber mats. The electrodes were submerged in pH7.4 phosphate buffer saline (PBS) electrolyte for various electroanalytical methods to characterize the electrochemical properties of the nanofibers.

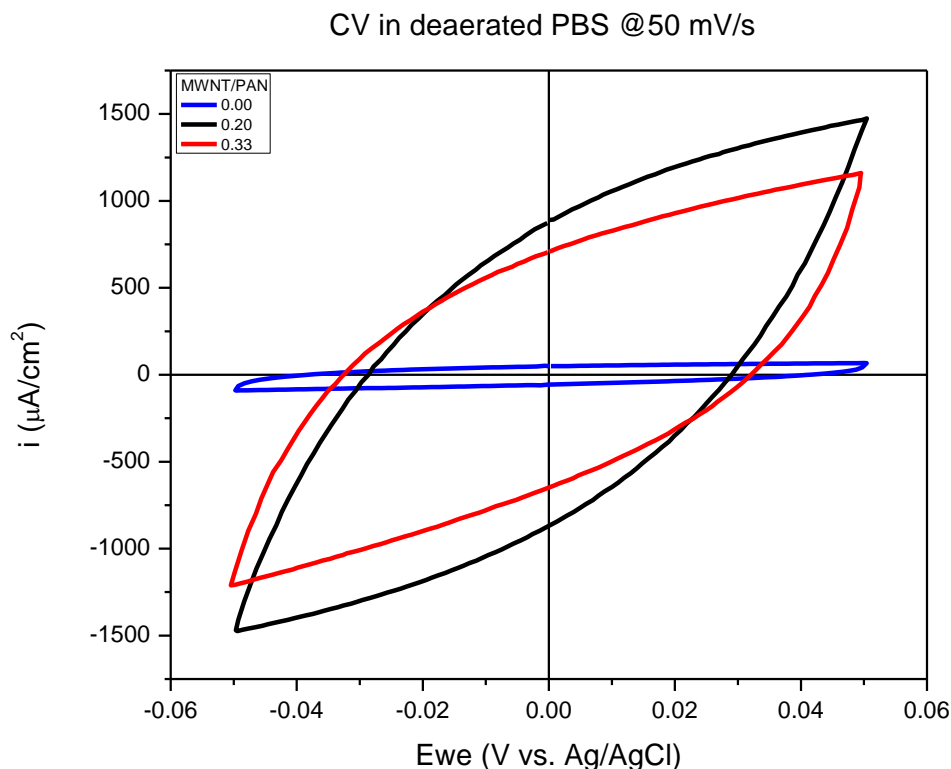


Figure 2.27 Cyclic voltammogram of working electrodes based on carbonized PAN- and PAN/MWNT-derived nanofibers of various MWNT loading. CV was conducted at room temperature.

Cyclic voltammograms (CV, Figure 2.27) of MWNT-embedded CNF showed that, compared to carbonaceous PAN-derived nanofibers with no MWNT loading, PAN/MWNT-derived CNF mat electrodes exhibited significantly higher capacitive current indicated by the height of cyclic voltammograms. Scan-rate dependent CV revealed both MWNT-embedded CNF mat retained nearly rectangular shape up to 25 mV/s, speaking to a good pseudocapacitive behavior and high reversibility due to fast ion kinetics.¹³¹ At higher scan rates, the voltammograms gradually lost the box-like shape and ended up with sharper ends, which were attributed to the porous structure of the MWNT-embedded CNFs, where inner pores were not easily accessible to ions at fast scan rates. Double-layer capacitance of the MWNT-embedded CNF mats were calculated by taking the slope of the

first linear region of the i - v curve (1-50 mV/s), where i was the current measured at a fixed potential where no faradaic reactions occurred. Double-layer capacitance were calculated to be 3386 and 2715 μF for MWNT-embedded CNF mat with MWNT loading of 0.20 and 0.33 (MWNT/PAN by wt.%), respectively. Contrary to the initial hypothesis that CNF with higher MWNT loading would exhibit larger double-layer capacitance, there seemed to be an optimum amount of MWNT.

The results from the electrochemical impedance spectroscopy on MWNT-embedded CNF mat electrodes were plotted as Nyquist and Bode plots. (Figure 2.28) While Nyquist plots can give parametric information such as solution and charge transfer resistance, Bode plots provide frequency-dependent response to describe the equivalent circuit in the electrode-electrolyte interface.

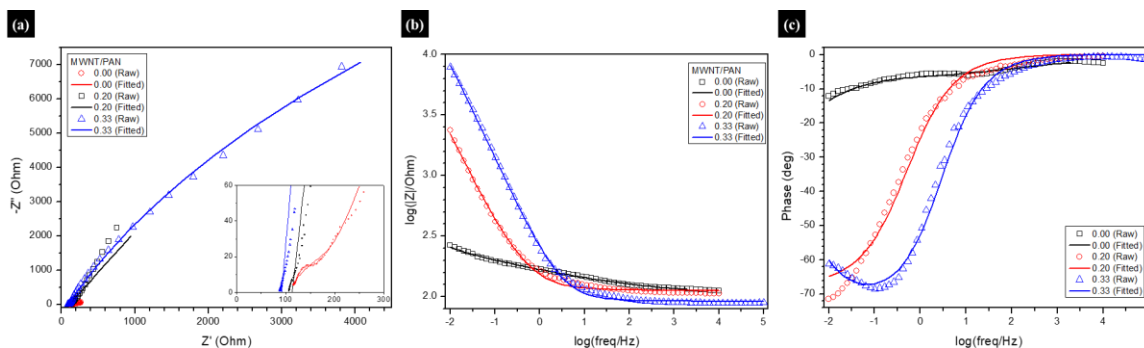


Figure 2.28 (a) Nyquist (b) Bode magnitude (c) Bode phase plots of MWNT-embedded CNF mat electrodes in deaerated PBS, pH7.4, at room temperature.

Nyquist plots of the MWNT-embedded CNF mat electrodes compared to that of PAN-derived CNF mat electrode were much more vertical, supporting the enhanced capacitive behavior shown in CV. Also, a semicircle from the high-frequency range that is typically visible in nanofiber mat electrodes was not observed with any MWNT loading,

which were attributed to the low contact resistance between the current collector and the electroactive nanofibers¹³² as well as small charge transfer resistance, indicating favorable charge transfer across the nanofiber electrode.¹³³ The x-intercept of the Nyquist plot, denoted as R_1 in Table 2.10, was used to determine the nanofiber mat electrical conductivity. R_1 of the CNF with MWNT/PAN loading of 0.33 showed the lowest R_1 , which could be due to the high concentration of the metallic MWNT, but R_1 value was consistently low for all CNF samples, measuring only up to 112 Ω . As suggested earlier in this section, the effect of MWNT on the electrical conductivity of the nanofibers was probably not significant until the loading was as high as 0.5 MWNT/PAN by wt.%.

Table 2.10 Parameters calculated from various electroanalytical methods for PAN- and PAN/MWNT-derived carbon nanofiber mat electrodes. All experiments were conducted in deaerated PBS, pH7.4, at room temperature.

Nanofiber diameter [nm]	MWNT/PAN	NF mat electrical conductivity [S/cm]	R_1 [Ω]	R_2 [Ω]	R_p [Ω] (LP)	C_2 [F]	Q_2 [Fs^{a-1}]	C_{dl} [μF] (CV)
140	0.00	1.7	106	147	4685	3.32×10^{-4}	1.53×10^{-3}	1055
200 (estimated from prev. literature)	0.00	1.4	118	116	3593	2.9×10^{-4}	1.13×10^{-3}	827
211	0.20	1.46	112	21931	2679	2.685	9.45×10^{-3}	3386
200	0.33	1.13	92	37559	5098	2.54×10^{-3}	1.05×10^{-3}	2715

Towards the lower frequency region, all three Nyquist plots trailed off with an approximately 45° incline, suggesting the presence of Warburg impedance, which was indicative of diffusive transport limitation. In the Bode plot (Figure 2.28(b)), the magnitude remained at its lowest in the high-frequency region for all three samples. As the frequency was decreased, impedance contributed from the capacitive component of the equivalent circuit increased the magnitude. The slope at which the magnitude increased was higher as

a function of concentration of MWNT, which added to the double layer capacitance. At the very low-frequency region, impedance on the capacitor was so high that the current would start to flow only to the resistive component, which is typically denoted as R_p (polarization resistance). The Bode phase plot (Figure 2.28(c)) for both 5PAN/1MWNT- and 5PAN/1.67MWNT-based CNF mat electrodes showed the phase angle reached up to approximately -70° , which was correlated with their highly capacitive behavior. Comparing to the CNF mat derived from purely PAN nanofibers that only reached a phase angle of -10° at the lowest frequency, it could be deduced that the addition of MWNT greatly improved the capacitance of the CNF mat electrodes by increasing the specific surface area and pore volume, which in turn enhanced the ion accessibility at the electrode-electrolyte interface. The Nyquist and Bode plots were thus fitted with a RRQW equivalent circuit and parameters calculated from the fitting are summarized in Table 2.10. To better investigate the effect of MWNT loading on the electrochemical properties and EIS parameters, the effect of nanofiber dimensions were taken out of account by estimating the values for pure PAN-derived CNF with 200-nm diameter, similar to that of MWNT-embedded CNFs, based on findings of previous literature.¹³⁴ The polarization resistance deduced from the EIS fitting (R_2) of MWNT-embedded CNFs was 2 orders of magnitude higher than that of PAN-derived CNFs, describing a more favorable material as an inert electrode. The Q_2 value, which represents the constant phase element, was highest for 5PAN/1MWNT-based CNF; this, combined with the double-layer capacitance calculated from CV, strongly suggested there was an optimum loading of MWNT when considering MWNT-embedded CNF as an electrode material. As Q_2 corresponds to the electroactive

area, that 5PAN/1MWNT-based CNFs showed higher Q_2 while exhibiting similar nanofiber dimensions and electrical conductivity indicated the MWNT-embedded CNFs were mesoporous. Brunauer–Emmett–Teller (BET) analysis would be beneficial in quantifying the porosity and specific surface area of the samples to better correlate the results from the electroanalytical methods to the effect of MWNT loading on electrochemical properties.

2.4.3 PAN/MWNT/ZnAc nanofibers

In order to further increase the mesoporous volume while retaining high electrical conductivity and mechanical integrity of carbonaceous nanofibers, zinc acetate (ZnAc) salt was added to the electrospinning solution to be oxidized to zinc oxide (ZnO) upon heat treatment, which could then be removed via simple acid treatment to create pores along the nanofibers. As more complexity in not only fabrication but also characterization and analysis of these so-called tri-composite nanofibers were expected, the effect of the addition of the ZnAc salt on the PAN nanofibers was first studied via design of experiment.

2.4.3.1 Fabrication and characterization of PAN/ZnAc nanofibers by DOE

Solution conditions according to the 2-factor DOE and the resulting solution and nanofiber properties are summarized in Table 2.11. This 2-factor DOE, containing upper and lower limit of two design factors creating a 4-corner “window” and a center point, was the minimum number of experiments needed to characterize any trends and effects of solution conditions varying the salt content on the PAN/ZnAc solution and nanofiber properties.

Table 2.11. Solution and nanofiber properties of various PAN/ZnAc samples. 0.1 wt.% BYK was added to every solution. All electrospinning and environmental conditions were fixed.

DOE code	Design factors		Solution conditions	Solution properties			Nanofiber properties		
	PAN wt.%	ZnAc: PAN (by wt.%)	ZnAc wt.%	Viscosity [cP]	Surface tension [dynes/cm]	Electrical conductivity [$\mu\text{S}/\text{cm}$]	Average nanofiber diameter [nm]	Bead density [bead/ μm^2]	Fiber fraction [$\mu\text{m}^2/\mu\text{m}^2$]
--	3.25	1:10	0.33	11.6	27.8	23.29	60 \pm 19	0.538	0.957
+-	7	1:10	0.7	86.3	27.4	41.56	389 \pm 62	0.000	1.000
00	5	1:5	1	24.2	27.3	32.1	209 \pm 43	0.016	0.996
-+	3.25	1:1	3.25	11.2	25.3	84.7	74 \pm 8	0.515	0.997
++	7	1:1	7	180.7	25.6	93.65	635 \pm 84	0.000	0.996

SEM images of the as-spun PAN/ZnAc nanofibers showed a clear increase in nanofiber dimensions as PAN wt.% was increased from 3.25 to 7 wt.%, while an increase in the overall salt content slightly affected the nanofiber dimensions as well. (Table 2.12) DOE analysis drawn on the effect of design factors on the solution properties in Figure 2.29 confirmed the polymer concentration was still the predominant factor for viscosity, which was a consistent result from PAN-only and PAN/MWNT data.

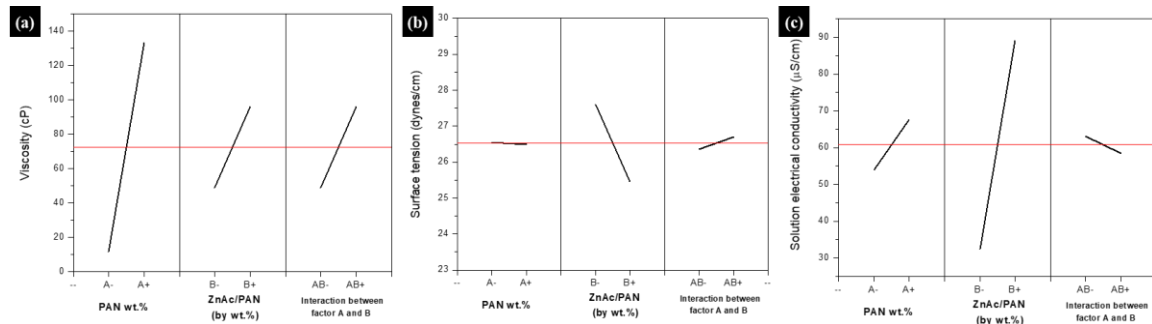


Figure 2.29 DOE analyses of (a) viscosity; (b) surface tension; and (c) solution electrical conductivity as a function of DOE factors laid out in Table 2.11.

While neither design factors exhibited significant impact on the surface tension, ZnAc concentration denoted as the weight ratio of ZnAc to PAN induced a positive response for the solution electrical conductivity, as expected. Based on these findings, it

was unsurprising to find PAN wt.% had the largest impact on the nanofiber diameter, which was known to be controlled by solution viscosity. (Figure 2.30(a))

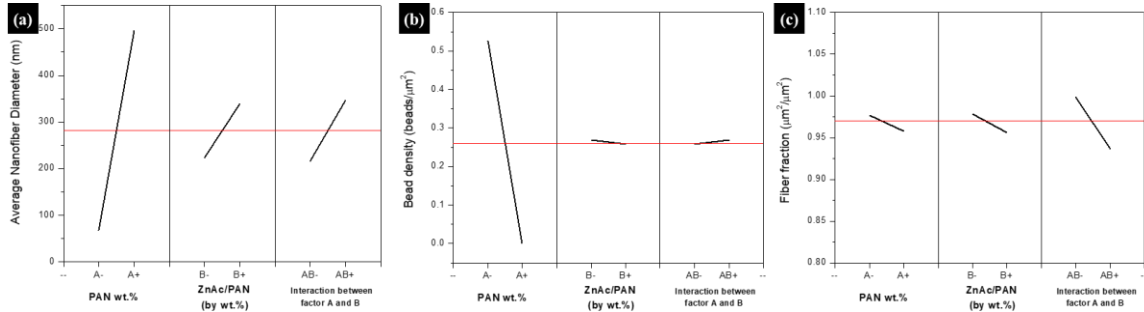


Figure 2.30 DOE analyses of (a) average nanofiber diameter; (b) bead density; and (c) fiber fraction as a function of DOE factors laid out in Table 2.8.

Table 2.12. SEM images of PAN/ZnAc/BYK nanofibers fabricated according to DOE conditions laid out in Table 2.11.

PAN wt.% \ ZnAc/PAN (by wt.%)	ZnAc/PAN (by wt.%)		
	0.1	0.2	1
3.25			
5			
7			

Similar to the DOE analysis of design factors on the bead density of PAN/MWNT nanofibers, increasing the polymer concentration decreased the bead density of PAN/ZnAc nanofibers; this might simply be due to the fact that higher-viscosity solutions tend to produce smoother, defect-free nanofibers, and the larger dimensions of the nanofibers allowed more room for composite materials. (Figure 2.30(b)) Regardless of the design factor variations, however, all solutions produced nanofibers with fiber fraction of 0.95 or higher, which was considered to be defect-free.

2.4.3.2 DOE analysis on solution properties and morphology of as-spun PAN/MWNT/ZnAc nanofibers

Tri-composite solutions containing various amounts of PAN, MWNT and ZnAc (all containing 0.1 wt.% BYK surfactant) according to a 2-factor DOE with a center point were electrospun to fabricate nanofibers. Solution conditions and the resulting solution and nanofiber properties of the five samples are summarized in Table 2.13.

Table 2.13. Solution and nanofiber properties of various PAN/MWNT/ZnAc samples. 0.1 wt.% BYK was added to every solution. All electrospinning and environmental conditions were fixed.

DOE code	Design factors		Solution conditions		Solution properties			Nanofiber properties		
	PAN: Composite	MWNT: ZnAc	MWNT wt. %	ZnAc wt. %	Viscosity [cP]	Surface tension [dynes/cm]	Electrical conductivity [μ S/cm]	Average nanofiber diameter [nm]	Bead density [bead/ μ m ²]	Fiber fraction [μ m ² / μ m ²]
--	10:1	5:1	0.67	0.13	351	20	30.59	568 \pm 105	0	1.000
+-	2:1	5:1	3.33	0.67	295	20	40.36	530 \pm 119	0.0122	0.941
00	5:1	1:1	0.80	0.80	272	21	42.41	729 \pm 219	0.0023	0.956
++	10:1	1:5	0.13	0.67	353	22	19.76	458 \pm 65	0	1.000
++	2:1	1:5	0.67	3.33	128	21	94.25	919 \pm 166	0.0006	0.999

DOE analysis of design factors on solution properties (Figure 2.31) showed that as the amount of composite materials (i.e. MWNT and ZnAc) increased with fixed amount of

PAN, solution viscosity increased. The positive viscosity response to the increase in the amount of ZnAc relative to MWNT was not expected, however; even though the DOE analysis for the PAN/ZnAc nanofibers in section 2.4.3.1 showed that increase in ZnAc concentration induced an increase in solution viscosity, the effect of MWNT concentration on the solution viscosity was expected to be more significant and thus a negative viscosity response was hypothesized when all three components were mixed together.

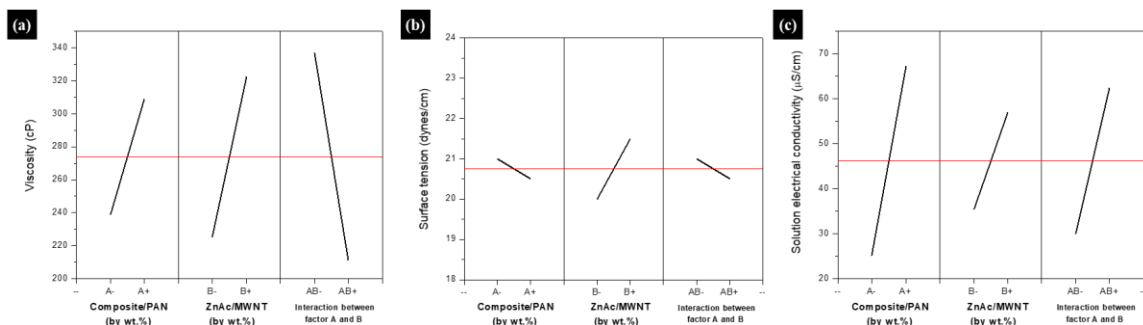


Figure 2.31. DOE analysis of solution properties of PAN/MWNT/ZnAc: (a) viscosity (b) surface tension (c) electrical conductivity as a function of DOE factors.

However, as the interaction between the two design factors in this DOE exhibited the highest impact on the solution viscosity, which showed a competing effect to the two individual design factors, further rheological characterization of the solutions might be needed to elucidate this phenomenon. Surface tension (Figure 2.31(b)) still confirmed to be unaffected by polymer or other composite material concentration, as it was known to be independently controlled by the absence or presence of a surfactant. The solution electrical conductivity (Figure 2.31(c)) showed positive response to the increase in overall amount of composite materials as well as that of ZnAc relative to MWNT, which were both expected trends since the upper limit of both design factors indicated a higher concentration of ZnAc salt, which was responsible for increasing the solution electrical conductivity.

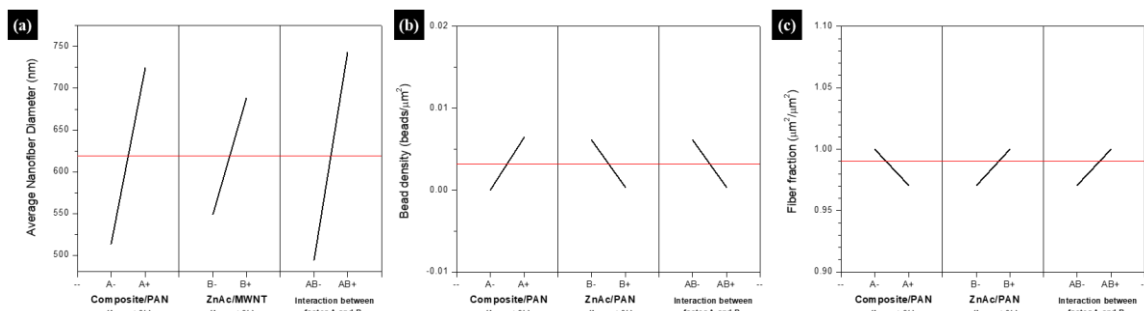


Figure 2.32 DOE analysis of nanofiber properties of PAN/MWNT/ZnAc: (a) nanofiber diameter (b) bead density (c) fiber fraction as a function of DOE factors.

DOE analyses of nanofiber properties as a function of DOE factors for the tri-composite nanofibers showed similar trends compared to PAN, PAN/MWNT and PAN/ZnAc nanofibers. (Figure 2.32) For example, an increase in overall composite materials increased the nanofiber diameter, as it was one of the contributing factors to the solution viscosity. No significant effect of DOE factors on the bead density nor fiber fraction was observed; all 5 samples fabricated from this DOE produced essentially bead-free nanofibers.

2.4.3.3 Morphological and elemental characterization of carbonized and acid-treated PAN/MWNT/ZnAc-derived nanofibers

In order to achieve highly mesoporous carbonaceous nanofibers (CNFs) while retaining high electrical conductivity, electrospun PAN/MWNT/ZnAc nanofibers were heat and then acid treated. The heat treatment, including stabilization and carbonization, would convert PAN to carbon and oxidize ZnAc to ZnO, while the acid treatment would remove the ZnO and other Zn residues to finally produce porous CNFs. Unlike PAN and PAN/MWNT nanofibers from previous sections, stabilization step was conducted at 280 °C then at 400 °C so that not only PAN went through its cyclization process, but also ZnAc

converted to ZnO. As 400 °C is typically the maximum temperature for PAN stabilization, past which PAN would start to burn off in the presence of oxygen, some brittleness and loss in nanofibrous structure were expected after the two-step stabilization. According to the SEM images shown in Figure 2.33, the surface of the nanofibers after two-step stabilization (Figure 2.33(c)) appeared rougher with some lamellar-like dimples compared to that after one-step stabilization (Figure 2.33(b)), indicating the conversion from ZnAc to ZnO might not have been complete after 280 °C. When both samples were carbonized under the same conditions (Figure 2.33(d) and (e)), those carbonized after two-step stabilization showed much rougher surface with the lamellar-like dimples more densely populated across the surface of the nanofibers. When these nanofibers were acid treated in 20 vol.% HCl, the lamellar-like dimples widened and deepened by 2-3 times, and some larger mesopores with diameters measuring up to 45 nm were observed randomly across the nanofiber surface.

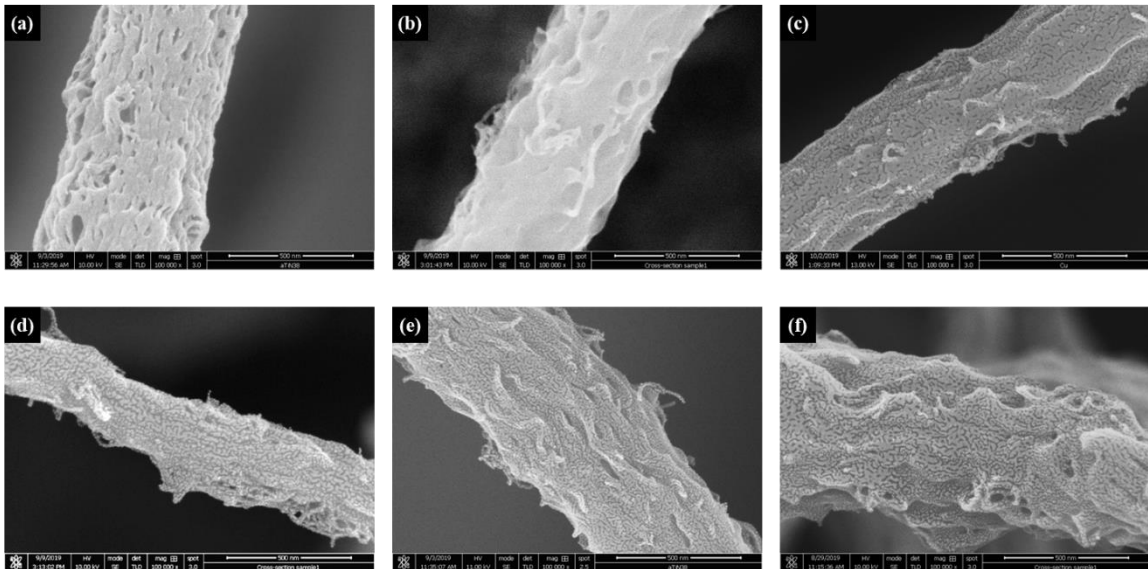


Figure 2.33. SEM images of 8 wt.% PAN, 3.33 wt.% MWNT, 0.67 wt.% ZnAc, 0.1 wt.% BYK nanofibers at various processing steps. (a) as-spun; (b) one-step stabilized; (c) two-step stabilized; (d) carbonized after one-step stabilization; (e) carbonized after two-step stabilization; (f) acid treated in 20 vol.% HCl in DI water for 60 s.

Elemental mapping via energy dispersive x-ray spectroscopy (EDS) confirmed that only after the two-step stabilization, carbonization followed by acid treatment was Zn removed. (Figure 2.34) Nanofibers treated with the same carbonization and acid conditions but with one-step stabilization showed residues of zinc, confirming that the second stabilization at 400 °C was necessary to fully convert ZnAc to ZnO.

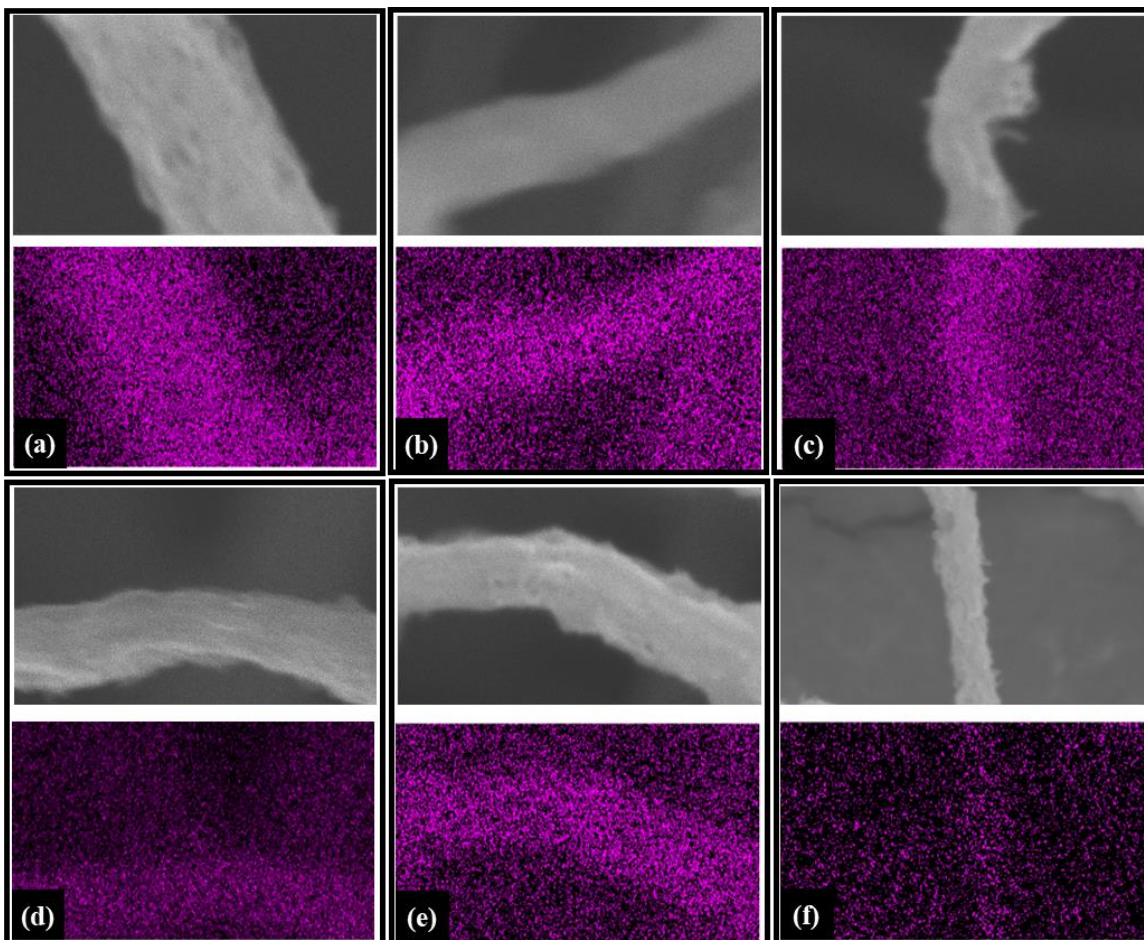


Figure 2.34. EDS mapping for Zn in PAN/MWNT/ZnAc-derived nanofibers at the following processing steps: (a) as-spun; (b) one-step stabilized; (c) carbonized after one-step stabilization; (d) carbonized after two-step stabilization; (e) acid treated after step (c); and (f) acid treated after step (d).

2.4.3.4 Electrochemical characterization of acid-treated PAN/MWNT/ZnAc-derived nanofibers

All five samples of tri-composite nanofibers were thus treated with two-step stabilization, carbonization, then acid treatment to produce porous MWNT-embedded CNFs, which were fabricated into electrodes for characterization via electroanalytical

methods such as cyclic voltammetry, linear polarization and electrochemical impedance spectroscopy.

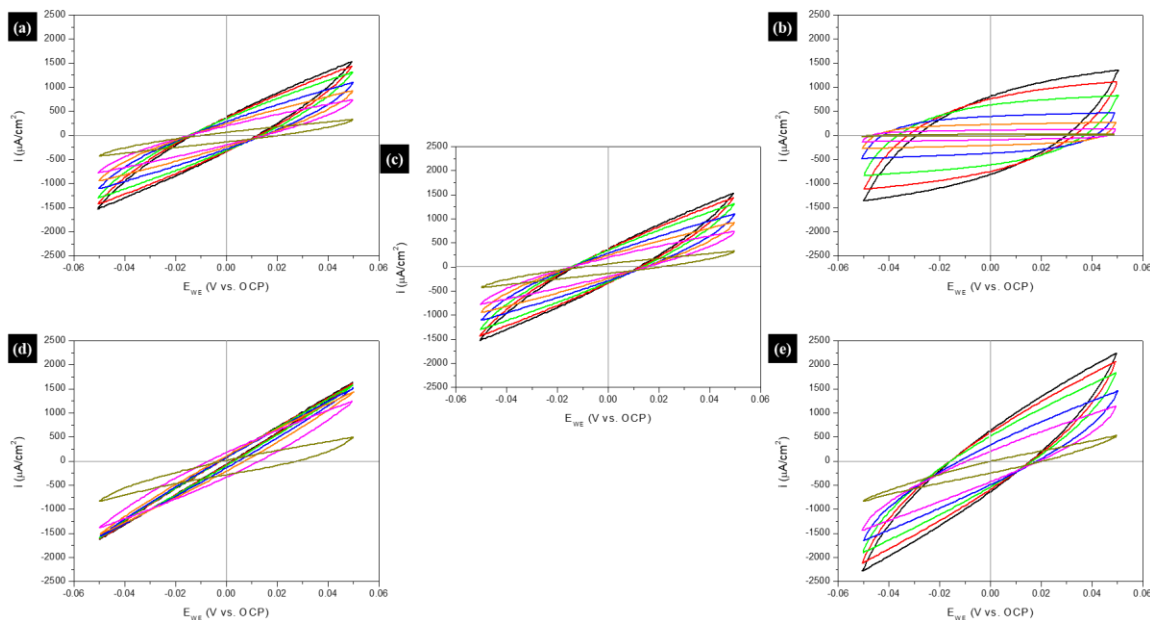


Figure 2.35. Cyclic voltammetry at 200, 150, 100, 50, 25, 10, 1 mV/s for PAN/MWNT/ZnAc-derived porous C/MWNT nanofibers with DOE code (a) ++ (b) +- (c) 00 (d) + (e) – in pH7.4 PBS at room temperature. Potential was swept with respect to the open circuit potential.

Cyclic voltammograms of the five porous CNF mat electrodes showed that sample with DOE code +- (i.e. 8PAN/3.33MWNT/0.67ZnAc) most closely resembled the box-like shape, which was representative of pseudocapacitive behavior. (Figure 2.35(b)) This rectangular geometry of the voltammogram was retained up to scan rates as high as 50 mV/s, which could be due to the mesoporous structure of the nanofibers. While the voltammograms of all five samples exhibited scan rate-dependent increase in current density and thus voltammogram height, electrodes fabricated from other 4 DOE codes did not show a box-like shape even at a scan rate as low as 1 mV/s, which was attributed to

that even though pores were observed on all four of the nanofibers, they were not easily accessible to ions.

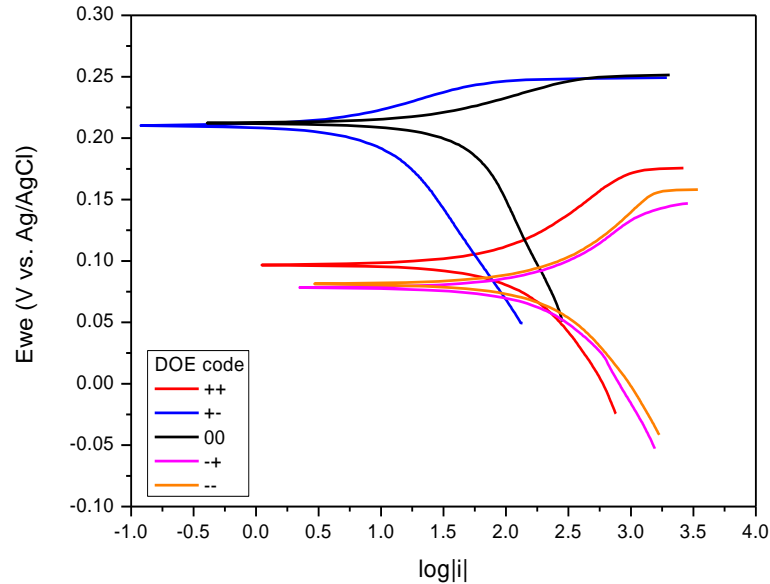


Figure 2.36 Tafel plots of carbonized PAN/MWNT/ZnAc-derived nanofiber mat electrodes in deaerated PBS, pH7.4, at room temperature. Scan rate was 1 mV/s.

Polarization resistance, R_p was calculated according to the following equation:

$$R_p = \frac{B}{i_{mix}} \text{ where } B = \frac{\beta_a \beta_c}{2.3(\beta_a + \beta_c)} \quad (\text{Equation 5})$$

The mixed current density, i_{mix} , was calculated based on the x-axis value of Tafel plot (Figure 2.36) at which the linear extrapolation of anodic and cathodic branches of the Tafel plot intersect. Slope of these extrapolated lines was also calculated to obtain β_a and β_c . All four parameters (i.e. i_{mix} , β_a , β_c , and R_p) for the five electrodes are summarized in Table 2.14. While the polarization resistance of all five nanofibers were relatively high, R_p of the tri-composite nanofibers of DOE code +- was the highest at 16091 Ω , which could also be attributed to the high density of mesopores on the nanofiber surface, allowing for more charge accumulation.

Table 2.14 Parameters calculated from Tafel plots of carbonized PAN/MWNT/ZnAc-derived nanofiber mat electrodes.

DOE code	i_{mix} [μA]	β_a [mV/dec]	β_c [mV/dec]	R_p [Ω]
++	28.334	90.4	126.3	808
+-	0.476	28.0	47.5	16,091
00	2.215	27.5	49.4	3,468
-+	20.266	68.7	94.0	852
--	10.081	69.8	87.3	1,673

Electrochemical impedance spectroscopy results were analyzed with Nyquist and Bode plots. All five curves in the Nyquist plot (Figure 2.37(a)) could be construed as a part of large, imperfect semicircle, supporting the high R_p calculated via LP since the diameter of the semicircle correlates with the polarization resistance. Zooming in on the Nyquist plot, however, a nearly vertical curves were observed in the very high-frequency region (inset of Figure 2.37(a)), indicating these porous CNF mats exhibited pseudocapacitive behavior. The x-intercept of the Nyquist plot and the Bode magnitude at the over the high-frequency region both represented the combination of electrolyte and electrode resistance, which was denoted as R_1 . With a known solution resistance of the electrolyte (20 Ω)(ref), the nanofiber mat resistance could be deduced. In the Bode magnitude plot (Figure 2.37(b)), electrode with DOE code +- reached the highest magnitude at the low frequency region, which was attributed to good pseudocapacitive behavior due to highly mesoporous structure.

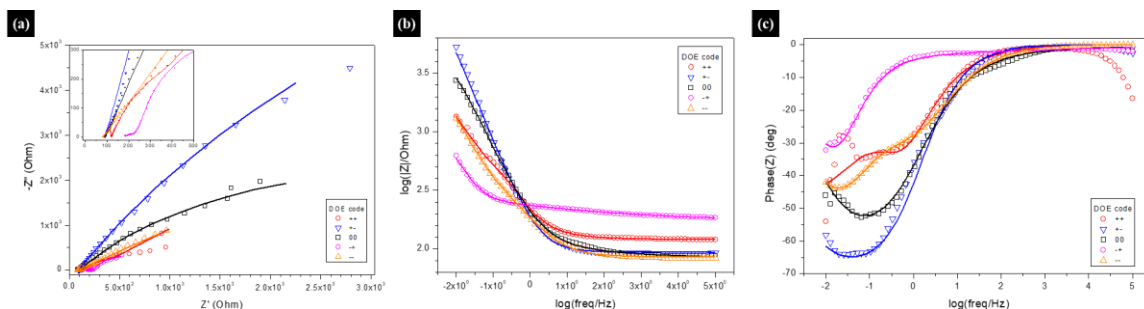


Figure 2.37 (a) Nyquist plot and (b,c) Bode plots of porous C/MWNT nanofibers derived from PAN/MWNT/ZnAc nanofibers.

In fact, the Bode phase plot (Figure 2.37(c)) of the same electrode reached up to -65° , which was close to the phase shift of -90° (i.e. phase shift of ideal capacitor). Furthermore, compared to the Bode phase plots of PAN/MWNT-derived CNF mats (Figure 2.37(c)), which showed a single peak at the low-frequency region, the presence of two peaks near the low-frequency range potentially indicated an additional RC component, which was likely attributed to the dimples across the surface of the nanofibers, as the single peak in the phase plot of MWNT-embedded CNFs was correlated with the capacitive behavior of MWNT. Therefore, the Nyquist and Bode plots were fitted according to RRQRQW equivalent circuit, which consisted of the additional RC component to the previously determined equivalent circuit of RRQW from the EIS of PAN/MWNT-derived CNF mat electrodes (See Section 2.4.2.3). Parameters calculated from this fitting are summarized in Table 2.15.

Table 2.15 Parameters calculated from various electroanalytical methods conducted with porous C/MWNT nanofiber mat electrodes derived from PAN/MWNT/ZnAc nanofibers.

DOE code	Nanofiber diameter [nm]	R ₁ [Ω]	R ₂ [Ω]	R _p [Ω] (LP)	C ₂ [F]	Q ₂ [Fs ⁻¹]	C _{dl} [μF] (CV)	C ₃ [F]	Q ₃ [Fs ⁻¹]	R ₃ [Ω]
--	568	80	654	1673	0.034	0.033	15098	0.019	9.66 x 10 ⁻³	183
+-	530	70	13175	16091	3.52 x 10 ⁻³	2.37 x 10 ⁻³	2080	9.0 x 10 ⁻¹⁴	2.49 x 10 ⁻³	23
00	729	88	6825	3468	0.017	0.013	9285	5.03 x 10 ⁻³	3.63 x 10 ⁻³	1304
-+	458	175	429	852	0.043	0.043	18355	4.6 x 10 ⁻⁴	5.64 x 10 ⁻³	89
++	919	120	6420	808	0.045	3.53 x 10 ⁻³	12535	1.4 x 10 ⁻¹⁰	1.24 x 10 ⁻⁵	83

DOE analyses were performed on some parameters determined by EIS fitting in the EC-Lab software as a function of the DOE factors. (Figure 2.38) The weight ratio between ZnAc and MWNT showed the highest impact on R₁, which was correlated with the nanofiber mat electrical conductivity. (Figure 2.38(a)) Increasing MWNT:ZnAc ratio by wt.% from 5:1 to 1:5 increased the nanofiber mat resistance, as more mesopores created not only on the surface of the nanofibers but also throughout the nanofibers would interfere with the current flow across the nanofiber mat electrode. This was compensated by the decrease in mat electrode with increase in the overall content of composite materials, likely attributed to the metallic properties of MWNT slightly contributing to the enhanced electrical conductivity of the nanofiber mat. R₂, on the other hand, was affected in the opposite direction by the same DOE factors. (Figure 2.38(b)) The polarization resistance increased with overall composite materials, and ZnAc in particular. This trend explained that while the increase in mesopores across the nanofiber mats decreased the overall electrical conductivity of the electrode, it increased the polarization resistance due to accumulation of charge in the mesopores.¹³⁵

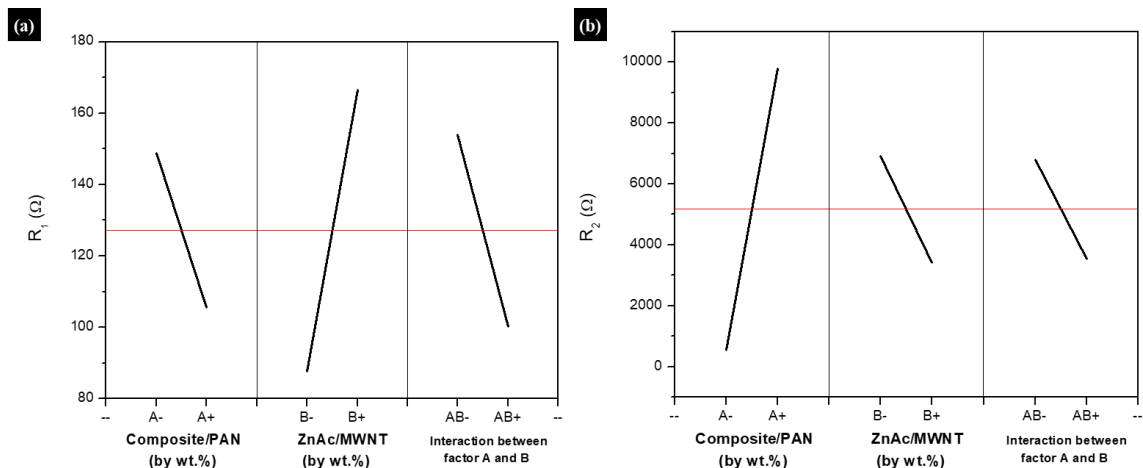


Figure 2.38 DOE analyses of (a) R_1 and (b) R_2 as a function of DOE factors for tri-composite nanofibers. R_1 and R_2 refer to the parameters calculated from EIS fitting.

2.5 Conclusion

Polyacrylonitrile-derived nanofibers with various amounts of composite materials such as multi-walled carbon nanotubes and zinc acetate were fabricated via electrospinning based on design of experiment as a systematic way to elucidate the effect of solution, electrospinning, and environmental conditions on the resulting nanofiber properties. Regardless of the composite material, the concentration of PAN in the electrospinning solution was the predominant factor in the solution viscosity, which had the highest impact on the nanofiber dimensions.

As-spun, aligned PAN nanofibers were fabricated for detailed study of size-dependent piezoelectric properties for the first time. Similar to other popularly known piezoelectric polymers like PVDF-TrFE, voltage output (V_{33}) increased significantly with nanofiber diameter. Decrease in piezoelectric properties with temperature was observed as the polar nitrile group in PAN was removed via cyclization with annealing. Addition of

MWNT significantly reduced the piezoelectric output along the 3 direction due to the metallic MWNT interfering with uniform charge distribution along the nanofibers. Further material characterization such as FT-IR and XRD would be required to correlate the change in molecular structure and crystallinity as a function of nanofiber diameter and annealing temperature with the resulting piezoelectric properties.

Precise control of loading of MWNT and ZnAc contributed to control of the solution properties as well as nanofiber properties, including electrical conductivity, double-layer capacitance, and polarization resistance, and the degree of this contribution was characterized by a series of DOE analyses. Various electroanalytical methods such as cyclic voltammetry, linear polarization and electrochemical impedance spectroscopy were used to characterize the PAN-derived carbonaceous nanofibers as a working electrode, which was fabricated by applying heat and/or acid treatment to the as-spun PAN-derived nanofibers.

2.6 References

1. Chung, M. *et al.* Applied Surface Science Ultrarapid sonochemical synthesis of enzyme-incorporated copper nanoflowers and their application to mediatorless glucose biofuel cell. *Appl. Surf. Sci.* **429**, 203–209 (2018).
2. Jing, X., Wang, Y., Wu, D. & Qiang, J. Sonochemical synthesis of polyaniline nanofibers. (2006) doi:10.1016/j.ultsonch.2006.02.001.
3. Xing, S., Zheng, H. & Zhao, G. Preparation of polyaniline nanofibers via a novel interfacial polymerization method. *Synth. Met.* **158**, 59–63 (2008).
4. Bian, C., Yu, Y. & Xue, G. Synthesis of conducting polyaniline/TiO₂ composite nanofibres by one-step in situ polymerization method. *J. Appl. Polym. Sci.* **104**, 21–26 (2007).
5. Yan, C., Chen, G., Zhou, X., Sun, J. & Lv, C. Template-Based Engineering of Carbon-Doped Co₃O₄ Hollow Nanofibers as Anode Materials for Lithium-Ion Batteries. *Adv. Funct. Mater.* **26**, 1428–1436 (2016).
6. Zhang, W. *et al.* Protein-mimetic peptide nanofibers: Motif design, self-assembly synthesis, and sequence-specific biomedical applications. *Progress in Polymer Science* vol. 80 94–124 (2018).
7. Liao, H. S. *et al.* Self-assembly mechanisms of nanofibers from peptide amphiphiles in solution and on substrate surfaces. *Nanoscale* **8**, 14814–14820 (2016).
8. Kenry & Lim, C. T. Nanofiber technology: current status and emerging developments. *Progress in Polymer Science* vol. 70 1–17 (2017).
9. Ye, D. *et al.* Large-Scale Direct-Writing of Aligned Nanofibers for Flexible Electronics. *Small* vol. 14 (2018).
10. Ahmad, Z., Rasekh, M. & Edirisinghe, M. Electrohydrodynamic Direct Writing of Biomedical Polymers and Composites. *Macromol. Mater. Eng.* **295**, 315–319 (2010).
11. Ren, L. & Kotha, S. P. Centrifugal jet spinning for highly efficient and large-scale fabrication of barium titanate nanofibers. *Mater. Lett.* **117**, 153–157 (2014).
12. Rogalski, J. J., Bastiaansen, C. W. M. & Peijs, T. Rotary jet spinning review—a potential high yield future for polymer nanofibers. *Nanocomposites* vol. 3 97–121 (2017).

13. Zhang, Z.-M., Duan, Y.-S., Xu, Q. & Zhang, B. A review on nanofiber fabrication with the effect of high-speed centrifugal force field. *J. Eng. Fiber. Fabr.* **14**, 155892501986751 (2019).
14. Hu, X. *et al.* Plasma-induced synthesis of CuO nanofibers and ZnO nanoflowers in water. *Plasma Chem. Plasma Process.* **34**, 1129–1139 (2014).
15. Sun, Y. *et al.* Plasma-Facilitated Synthesis of Amidoxime/Carbon Nanofiber Hybrids for Effective Enrichment of ²³⁸U(VI) and ²⁴¹Am(III). *Environ. Sci. Technol.* **51**, 12274–12282 (2017).
16. Medeiros, E. S., Glenn, G. M., Klamczynski, A. P., Orts, W. J. & Mattoso, L. H. C. Solution blow spinning: A new method to produce micro- and nanofibers from polymer solutions. *J. Appl. Polym. Sci.* **113**, 2322–2330 (2009).
17. Rotta, M. *et al.* YBCO ceramic nanofibers obtained by the new technique of solution blow spinning. *Ceram. Int.* **42**, 16230–16234 (2016).
18. Koyama, H., Watanabe, Y. & Suzuki, A. Poly(*p*-phenylene sulfide) nanofibers prepared by CO₂ laser supersonic drawing. *J. Appl. Polym. Sci.* **131**, n/a-n/a (2014).
19. Roberts, S. Dielectric and piezoelectric properties of barium titanate. *Phys. Rev.* **71**, 890–895 (1947).
20. Kawai, H. The Piezoelectricity of Poly (vinylidene Fluoride). *Jpn. J. Appl. Phys.* **8**, 975–976 (1969).
21. Mimura, K. ichi, Moriya, M., Sakamoto, W. & Yogo, T. Synthesis of BaTiO₃ nanoparticle/poly(2-hydroxyethyl methacrylate) hybrid nanofibers via electrospinning. *Compos. Sci. Technol.* **70**, 492–497 (2010).
22. Lee, S. J., Arun, A. P. & Kim, K. J. Piezoelectric properties of electrospun poly(l-lactic acid) nanofiber web. *Mater. Lett.* **148**, 58–62 (2015).
23. Sencadas, V. *et al.* Local piezoelectric activity of single poly(L-lactic acid) (PLLA) microfibers. *Appl. Phys. A Mater. Sci. Process.* **109**, 51–55 (2012).
24. Sultana, A. *et al.* Human skin interactive self-powered wearable piezoelectric bio-skin by electrospun poly-l-lactic acid nanofibers for non-invasive physiological signal monitoring. *J. Mater. Chem. B* **5**, 7352–7359 (2017).
25. Zhu, J., Jia, L. & Huang, R. Electrospinning poly(l-lactic acid) piezoelectric ordered porous nanofibers for strain sensing and energy harvesting. *J. Mater. Sci. Mater. Electron.* **28**, 12080–12085 (2017).

26. Zhao, G. *et al.* Electrospun Poly(L-Lactic Acid) Nanofibers for Nanogenerator and Diagnostic Sensor Applications. *Macromol. Mater. Eng.* **302**, 1600476 (2017).
27. Cuong, N. T. *et al.* On the Nanoscale Mapping of the Mechanical and Piezoelectric Properties of Poly (L-Lactic Acid) Electrospun Nanofibers. *Appl. Sci.* **10**, 652 (2020).
28. Zhao, G. *et al.* Piezoelectric Polyacrylonitrile Nanofiber Film-Based Dual-Function Self-Powered Flexible Sensor. *ACS Appl. Mater. Interfaces* **10**, 15855–15863 (2018).
29. Wang, W. *et al.* Unexpectedly high piezoelectricity of electrospun polyacrylonitrile nanofiber membranes. *Nano Energy* **56**, 588–594 (2019).
30. Sengupta, D. *et al.* Flexible Graphitized Polyacrylonitrile Nanofiber Bundles for Strain Sensors. in *NEMS 2018 - 13th Annual IEEE International Conference on Nano/Micro Engineered and Molecular Systems* 615–618 (Institute of Electrical and Electronics Engineers Inc., 2018). doi:10.1109/NEMS.2018.8556930.
31. Street, R. M., Minagawa, M., Vengrenyuk, A. & Schauer, C. L. Piezoelectric electrospun polyacrylonitrile with various tacticities. *J. Appl. Polym. Sci.* **136**, 47530 (2019).
32. Baniasadi, M., Xu, Z., Hong, S., Naraghi, M. & Minary-Jolandan, M. Thermo-electromechanical Behavior of Piezoelectric Nanofibers. *ACS Appl. Mater. Interfaces* **8**, 2540–2551 (2016).
33. Persano, L. *et al.* High performance piezoelectric devices based on aligned arrays of nanofibers of poly(vinylidene fluoride-co-trifluoroethylene). *Nat. Commun.* **4**, 1–10 (2013).
34. Sencadas, V., Ribeiro, C., Bdikin, I. K., Kholkin, A. L. & Lanceros-Mendez, S. Local piezoelectric response of single poly(vinylidene fluoride) electrospun fibers. *Phys. status solidi* **209**, 2605–2609 (2012).
35. Baniasadi, M. *et al.* High-performance coils and yarns of polymeric piezoelectric nanofibers. *ACS Appl. Mater. Interfaces* **7**, 5358–5366 (2015).
36. Gheibi, A., Latifi, M., Merati, A. A. & Bagherzadeh, R. Piezoelectric electrospun nanofibrous materials for self-powering wearable electronic textiles applications. *J. Polym. Res.* **21**, 1–7 (2014).

37. Park, S. H., Lee, H. B., Yeon, S. M., Park, J. & Lee, N. K. Flexible and Stretchable Piezoelectric Sensor with Thickness-Tunable Configuration of Electrospun Nanofiber Mat and Elastomeric Substrates. *ACS Appl. Mater. Interfaces* **8**, 24773–24781 (2016).
38. Fu, D., Suzuki, H., Ogawa, T. & Ishikawa, K. High-piezoelectric behavior of c-axis-oriented lead zirconate titanate thin films with composition near the morphotropic phase boundary. *Appl. Phys. Lett* **80**, 3572 (2002).
39. Okano, H. *et al.* Piezoelectric Response to Pressure of Aluminum Nitride Thin Films Prepared on Nickel-Based Superalloy Diaphragms. *Japanese J. Appl. Phys. To* **45**, 5169 (2006).
40. Ho, C.-J., Shing, T.-K. & Li, P.-C. Preferred Orientation Control and Characterization of AlN Thin Films Using Reactive Sputtering. *Tamkang Journal of Science and Engineering* vol. 7 (2004).
41. Bauer, S. & Bauer, F. Piezoelectric Polymers and Their Applications. in *Springer Series in Materials Science* vol. 114 157–177 (Springer Verlag, 2008).
42. Kobiakov, I. B. Elastic, piezoelectric and dielectric properties of ZnO and CdS single crystals in a wide range of temperatures. *Solid State Commun.* **35**, 305–310 (1980).
43. Takahashi, H. *et al.* Lead-Free Barium Titanate Ceramics with Large Piezoelectric Constant Fabricated by Microwave Sintering. *Jpn. J. Appl. Phys.* **45**, L30–L32 (2006).
44. Royer, D. & Kmetik, V. Measurement of piezoelectric constants using an optical heterodyne interferometer. *Electron. Lett.* **28**, 1828–1830 (1992).
45. Tian, J., Han, P. & Payne, D. A. Measurements along the growth direction of PMN-PT crystals: Dielectric, piezoelectric, and elastic properties. in *IEEE Transactions on ultrasonics, ferroelectrics, and frequency control* 1895–1902 (2007).
46. Varadan, V. K., Vinoy, K. J., Gopalakrishnan, S. & Wiley, J. *Smart Material Systems and MEMS: Design and Development Methodologies*.
47. Ummer, R. P., Thevenot, C., Didier Rouxel, E., Sabu Thomas bc, E. & Kalarikkal, N. Electric, magnetic, piezoelectric and magnetoelectric studies of phase pure (BiFeO₃-NaNbO₃)-(P(VDF-TrFE)) nanocomposite films prepared by spin coating. *RSC Adv.* **6**, (2016).

48. Fukada, E. Recent developments of polar piezoelectric polymers. in *IEEE Transactions on dielectrics and electrical insulation* 1110–1119 (2006).
49. Jacob, J. *et al.* Smart Piezoelectric Nanohybrid of Poly(3-hydroxybutyrate-co-3-hydroxyvalerate) and Barium Titanate for Stimulated Cartilage Regeneration. *ACS Appl. Bio Mater.* (2019) doi:10.1021/acsabm.9b00667.
50. Rajala, S. *et al.* Cellulose Nanofibril Film as a Piezoelectric Sensor Material. *ACS Appl. Mater. Interfaces* (2016) doi:10.1021/acsami.6b03597.
51. Harrison, J. S. & Ounaies, Z. *Piezoelectric Polymers.* (2001).
52. Street, R. M., Minagawa, M., Vengrenyuk, A. & Schauer, C. L. Piezoelectric electrospun polyacrylonitrile with various tacticities. *J. Appl. Polym. Sci.* **136**, 47530 (2019).
53. Isakov, D. *et al.* Energy harvesting from nanofibers of hybrid organic ferroelectric dabcoHReO₄. *Appl. Phys. Lett.* **104**, 032907 (2014).
54. Lee, S., Ahn, Y., Prabu, A. & Kim, K. Piezoelectric Polymer and Piezocapacitive Nanoweb Based Sensors for Monitoring Vital Signals and Energy Expenditure in Smart Textiles. *J. Fiber Bioeng. Informatics* **6**, 369–381 (2013).
55. Huang, T. *et al.* Human walking-driven wearable all-fiber triboelectric nanogenerator containing electrospun polyvinylidene fluoride piezoelectric nanofibers. *Nano Energy* **14**, 226–235 (2014).
56. Wang, X. *et al.* A flexible triboelectric-piezoelectric hybrid nanogenerator based on P(VDF-TrFE) nanofibers and PDMS/MWCNT for wearable devices. *Sci. Rep.* **6**, 1–10 (2016).
57. Chen, X. *et al.* A wave-shaped hybrid piezoelectric and triboelectric nanogenerator based on P(VDF-TrFE) nanofibers. *Nanoscale* **9**, 1263–1270 (2017).
58. Chen, X. *et al.* Flexible fiber-based hybrid nanogenerator for biomechanical energy harvesting and physiological monitoring. *Nano Energy* **38**, 43–50 (2017).
59. Guo, Y. *et al.* All-fiber hybrid piezoelectric-enhanced triboelectric nanogenerator for wearable gesture monitoring. *Nano Energy* **48**, 152–160 (2018).
60. Song, J. *et al.* Highly Flexible, Large-Area, and Facile Textile-Based Hybrid Nanogenerator with Cascaded Piezoelectric and Triboelectric Units for Mechanical Energy Harvesting. *Adv. Mater. Technol.* **3**, 1800016 (2018).

61. Sun, J. G., Yang, T. N., Wang, C. Y. & Chen, L. J. A flexible transparent one-structure tribo-piezo-pyroelectric hybrid energy generator based on bio-inspired silver nanowires network for biomechanical energy harvesting and physiological monitoring. *Nano Energy* **48**, 383–390 (2018).
62. Lee, C. *et al.* Electrospun uniaxially-aligned composite nanofibers as highly-efficient piezoelectric material. *Ceram. Int.* **42**, 2734–2740 (2016).
63. Dhakras, D. & Ogale, S. High-Performance Organic-Inorganic Hybrid Piezo-Nanogenerator via Interface Enhanced Polarization Effects for Self-Powered Electronic Systems. *Adv. Mater. Interfaces* **3**, 1600492 (2016).
64. Shi, K., Sun, B., Huang, X. & Jiang, P. Synergistic effect of graphene nanosheet and BaTiO₃ nanoparticles on performance enhancement of electrospun PVDF nanofiber mat for flexible piezoelectric nanogenerators. *Nano Energy* **52**, 153–162 (2018).
65. Siddiqui, S. *et al.* An Omnidirectionally Stretchable Piezoelectric Nanogenerator Based on Hybrid Nanofibers and Carbon Electrodes for Multimodal Straining and Human Kinematics Energy Harvesting. *Adv. Energy Mater.* **8**, 1701520 (2018).
66. Deng, W. *et al.* Cowpea-structured PVDF/ZnO nanofibers based flexible self-powered piezoelectric bending motion sensor towards remote control of gestures. *Nano Energy* **55**, 516–525 (2019).
67. Ma, J., Zhang, Q., Lin, K., Zhou, L. & Ni, Z. Piezoelectric and optoelectronic properties of electrospinning hybrid PVDF and ZnO nanofibers. (2018) doi:10.1088/2053-1591/aab747.
68. Zhang, H.-D. *et al.* Electrospun ZnO/SiO₂ hybrid nanofibers for flexible pressure sensor. *J. Phys. D: Appl. Phys.* **51**, 085102 (2018).
69. Bairagi, S. & Ali, S. W. A hybrid piezoelectric nanogenerator comprising of KNN/ZnO nanorods incorporated PVDF electrospun nanocomposite webs. *Int. J. Energy Res.* **44**, 5545–5563 (2020).
70. Fakhri, P. *et al.* Flexible hybrid structure piezoelectric nanogenerator based on ZnO nanorod/PVDF nanofibers with improved output. *RSC Adv.* **9**, 10117–10123 (2019).
71. Sun, B. *et al.* Electrospun poly(vinylidene fluoride)-zinc oxide hierarchical composite fiber membrane as piezoelectric acoustoelectric nanogenerator. *J. Mater. Sci.* **54**, 2754–2762 (2019).

72. Liu, X., Wang, X., Zhao, H. & Du, Y. Myocardial cell pattern on piezoelectric nanofiber mats for energy harvesting. in *Journal of Physics: Conference Series* vol. 557 (Institute of Physics Publishing, 2014).
73. Kang, H. B., Chang, J., Koh, K., Lin, L. & Cho, Y. S. High quality Mn-doped (Na,K)NbO₃ nanofibers for flexible piezoelectric nanogenerators. *ACS Appl. Mater. Interfaces* **6**, 10576–10582 (2014).
74. Tang, M., Shu, W. & Yang, F. The fabrication of vanadium-doped ZnO piezoelectric nanofiber by electrospinning. (2010) doi:10.1088/0957-4484/21/5/055708.
75. Ahmed, A. *et al.* Preparation of PVDF-TrFE based electrospun nanofibers decorated with PEDOT-CNT/rGO composites for piezo-electric pressure sensor. *J. Mater. Sci. Mater. Electron.* **30**, 14007–14021 (2019).
76. Xu, Y. *et al.* Glowing stereocomplex biopolymers are generating power: Polylactide/carbon quantum dot hybrid nanofibers with high piezoresponse and multicolor luminescence. *J. Mater. Chem. A* **7**, 1810–1823 (2019).
77. Kim, S. *et al.* Utilization of a magnetic field-driven microscopic motion for piezoelectric energy harvesting. *Nanoscale* **11**, 20527–20533 (2019).
78. Tiwari, S., Gaur, A., Kumar, C. & Maiti, P. Electrospun hybrid nanofibers of poly(vinylidene fluoride) and functionalized graphene oxide as a piezoelectric energy harvester. *Sustain. Energy Fuels* **4**, 2469–2479 (2020).
79. Hosseini, S. M. & Yousefi, A. A. Electrospun PVDF/MWCNT/OMMT hybrid nanocomposites: preparation and characterization. *Iran. Polym. J. (English Ed.)* **26**, 331–339 (2017).
80. Hosseini, S. M. & Yousefi, A. A. Piezoelectric sensor based on electrospun PVDF-MWCNT-Cloisite 30B hybrid nanocomposites. *Org. Electron.* **50**, 121–129 (2017).
81. Liu, Z. H., Pan, C. T., Lin, L. W. & Lai, H. W. Piezoelectric properties of PVDF/MWCNT nanofiber using near-field electrospinning. *Sensors Actuators, A Phys.* **193**, 13–24 (2013).
82. Samadi, A., Hosseini, S. M. & Mohseni, M. Investigation of the electromagnetic microwaves absorption and piezoelectric properties of electrospun Fe₃O₄-GO/PVDF hybrid nanocomposites. *Org. Electron.* **59**, 149–155 (2018).

83. Tiwari, S., Gaur, A., Kumar, C. & Maiti, P. Enhanced piezoelectric response in nanoclay induced electrospun PVDF nanofibers for energy harvesting. *Energy* **171**, 485–492 (2019).
84. Haddadi, S. A., Ahmad Ramazani, S. A., Talebi, S., Fattahpour, S. & Hasany, M. Investigation of the Effect of Nanosilica on Rheological, Thermal, Mechanical, Structural, and Piezoelectric Properties of Poly(vinylidene fluoride) Nanofibers Fabricated Using an Electrospinning Technique. *Ind. Eng. Chem. Res.* **56**, 12596–12607 (2017).
85. Samadi, A., Ahmadi, R. & Hosseini, S. M. Influence of TiO₂-Fe₃O₄-MWCNT hybrid nanotubes on piezoelectric and electromagnetic wave absorption properties of electrospun PVDF nanocomposites. *Org. Electron.* **75**, 105405 (2019).
86. Parangusan, H., Ponnamma, D. & Al-Maadeed, M. A. A. Stretchable Electrospun PVDF-HFP/Co-ZnO Nanofibers as Piezoelectric Nanogenerators. *Sci. Rep.* **8**, 754 (2018).
87. Mao, D., Quevedo-Lopez, M. A., Stiegler, H., Gnade, B. E. & Alshareef, H. N. Optimization of poly(vinylidene fluoride-trifluoroethylene) films as non-volatile memory for flexible electronics. *Org. Electron.* **11**, 925–932 (2010).
88. Chen, X. *et al.* Flexible piezoelectric nanofiber composite membranes as high performance acoustic emission sensors. *Sensors Actuators A Phys.* **199**, 372–378 (2013).
89. Baniasadi, M. *et al.* Correlation of annealing temperature, morphology, and electro-mechanical properties of electrospun piezoelectric nanofibers. *Polymer (Guildf)*. **127**, 192–202 (2017).
90. Jiang, Y. *et al.* Aligned P(VDF-TrFE) Nanofibers for Enhanced Piezoelectric Directional Strain Sensing. *Polymers (Basel)*. **10**, 364 (2018).
91. Chang, C., Tran, V. H., Wang, J., Fuh, Y. K. & Lin, L. Direct-write piezoelectric polymeric nanogenerator with high energy conversion efficiency. *Nano Lett.* **10**, 726–731 (2010).
92. Shao, H., Fang, J., Wang, H. & Lin, T. Effect of electrospinning parameters and polymer concentrations on mechanical-to-electrical energy conversion of randomly-oriented electrospun poly(vinylidene fluoride) nanofiber mats. *RSC Adv.* **5**, 14345–14350 (2015).

93. Gheibi, A., Bagherzadeh, R., Merati, A. A. & Latifi, M. Electrical power generation from piezoelectric electrospun nanofibers membranes: electrospinning parameters optimization and effect of membranes thickness on output electrical voltage. *J. Polym. Res.* **21**, 1–14 (2014).
94. Ico, G. *et al.* Size-dependent piezoelectric and mechanical properties of electrospun P(VDF-TrFE) nanofibers for enhanced energy harvesting. *J. Mater. Chem. A* **4**, 2293–2304 (2016).
95. Shirazi, P. *et al.* Size-Dependent Piezoelectric Properties of Electrospun BaTiO₃ for Enhanced Energy Harvesting. *Adv. Sustain. Syst.* **1**, 1700091 (2017).
96. Chen, Y. *et al.* A Highly Efficient and Robust Nanofiber Cathode for Solid Oxide Fuel Cells. *Adv. Energy Mater.* **7**, 1601890 (2017).
97. Brodt, M., Wycisk, R. & Pintauro, P. N. Nanofiber Electrodes with Low Platinum Loading for High Power Hydrogen/Air PEM Fuel Cells. *J. Electrochem. Soc.* **160**, F744–F749 (2013).
98. Manickam, S. S. *et al.* Activated carbon nanofiber anodes for microbial fuel cells. *Carbon N. Y.* **53**, 19–28 (2013).
99. Karra, U., Manickam, S. S., McCutcheon, J. R., Patel, N. & Li, B. Power generation and organics removal from wastewater using activated carbon nanofiber (ACNF) microbial fuel cells (MFCs). *Int. J. Hydrogen Energy* **38**, 1588–1597 (2013).
100. Santoro, C. *et al.* Activated carbon nanofibers (ACNF) as cathode for single chamber microbial fuel cells (SCMFCs). *J. Power Sources* **243**, 499–507 (2013).
101. Ahn, M., Lee, J. & Lee, W. Nanofiber-based composite cathodes for intermediate temperature solid oxide fuel cells. *J. Power Sources* **353**, 176–182 (2017).
102. Lai, C., Kolla, P., Zhao, Y., Fong, H. & Smirnova, A. L. Lignin-derived electrospun carbon nanofiber mats with supercritically deposited Ag nanoparticles for oxygen reduction reaction in alkaline fuel cells. *Electrochim. Acta* **130**, 431–438 (2014).
103. Abdelkareem, M. A., Al Haj, Y., Alajami, M., Alawadhi, H. & Barakat, N. A. M. Ni-Cd carbon nanofibers as an effective catalyst for urea fuel cell. *J. Environ. Chem. Eng.* **6**, 332–337 (2018).
104. Ghouri, Z. K., Barakat, N. A. M., Obaid, M., Lee, J. H. & Kim, H. Y. Co/CeO₂-decorated carbon nanofibers as effective non-precious electro-catalyst for fuel cells application in alkaline medium. *Ceram. Int.* **41**, 2271–2278 (2015).

105. Zhao, W. *et al.* Sustainable seaweed-based one-dimensional (1D) nanofibers as high-performance electrocatalysts for fuel cells. *J. Mater. Chem. A* **3**, 14188–14194 (2015).
106. Zamani, P. *et al.* Electrospun iron-polyaniline-polyacrylonitrile derived nanofibers as non-precious oxygen reduction reaction catalysts for PEM fuel cells. *Electrochim. Acta* **139**, 111–116 (2014).
107. Chen, Y. *et al.* A durable, high-performance hollow-nanofiber cathode for intermediate-temperature fuel cells. *Nano Energy* **26**, 90–99 (2016).
108. Bauer, A. *et al.* Synthesis and characterization of Nb-TiO₂ mesoporous microsphere and nanofiber supported Pt catalysts for high temperature PEM fuel cells. *Electrochim. Acta* **77**, 1–7 (2012).
109. Zhang, W. *et al.* La_{0.6}Sr_{0.4}Co_{0.2}Fe_{0.8}O_{3-δ}/CeO₂ Heterostructured Composite Nanofibers as a Highly Active and Robust Cathode Catalyst for Solid Oxide Fuel Cells. *ACS Appl. Mater. Interfaces* **11**, 26830–26841 (2019).
110. Choi, J., Lee, K. M., Wycisk, R., Pintauro, P. N. & Mather, P. T. Sulfonated Polysulfone/POSS Nanofiber Composite Membranes for PEM Fuel Cells. *J. Electrochem. Soc.* **157**, B914 (2010).
111. Lee, C. *et al.* SiO₂/sulfonated poly ether ether ketone (SPEEK) composite nanofiber mat supported proton exchange membranes for fuel cells. *J. Mater. Sci.* **48**, 3665–3671 (2013).
112. Wang, H. *et al.* Modification of Nafion membrane with biofunctional SiO₂ nanofiber for proton exchange membrane fuel cells. *J. Power Sources* **340**, 201–209 (2017).
113. Tamura, T. & Kawakami, H. Aligned electrospun nanofiber composite membranes for fuel cell electrolytes. *Nano Lett.* **10**, 1324–1328 (2010).
114. Li, H. Y. & Liu, Y. L. Nafion-functionalized electrospun poly(vinylidene fluoride) (PVDF) nanofibers for high performance proton exchange membranes in fuel cells. *J. Mater. Chem. A* **2**, 3783–3793 (2014).
115. Park, J. W., Wycisk, R. & Pintauro, P. N. Nafion/PVDF nanofiber composite membranes for regenerative hydrogen/bromine fuel cells. *J. Memb. Sci.* **490**, 103–112 (2015).
116. Park, A. M., Wycisk, R. J., Ren, X., Turley, F. E. & Pintauro, P. N. Crosslinked poly(phenylene oxide)-based nanofiber composite membranes for alkaline fuel cells. *J. Mater. Chem. A* **4**, 132–141 (2015).

117. Li, H. Y. & Liu, Y. L. Polyelectrolyte composite membranes of polybenzimidazole and crosslinked polybenzimidazole-polybenzoxazine electrospun nanofibers for proton exchange membrane fuel cells. *J. Mater. Chem. A* **1**, 1171–1178 (2013).
118. Wang, T. Electrospun carbon nanofibers for electrochemical capacitor electrodes. (2007).
119. Guo, C., Zhou, L. & Lv, J. Effects of expandable graphite and modified ammonium polyphosphate on the flame-retardant and mechanical properties of wood flour-polypropylene composites. *Polym. Polym. Compos.* **21**, 449–456 (2013).
120. Kim, C., Yang, K.-S. & Lee, W.-J. The Use of Carbon Nanofiber Electrodes Prepared by Electrospinning for Electrochemical Supercapacitors. *Electrochem. Solid-State Lett.* **7**, A397 (2004).
121. Gan, J. K., Lim, Y. S., Pandikumar, A., Huang, N. M. & Lim, H. N. Graphene/polypyrrole-coated carbon nanofiber core-shell architecture electrode for electrochemical capacitors. *RSC Adv.* **5**, 12692–12699 (2015).
122. Ueda, H. & Carr, S. H. *Piezoelectricity in Polyacrylonitrile*. *Polymer Journal* vol. 16 (1984).
123. von Berlepsch, H., Künstler, W., Wedel, A., Danz, R. & Geiß, D. Piezoelectric Activity in a Copolymer of Acrylonitrile and Methylacrylate. *IEEE Trans. Electr. Insul.* **24**, 357–362 (1989).
124. Comstock, R. J., Stupp, S. I., Carr, S. H. & Stupp, S. I. Thermally stimulated discharge currents from polyacrylonitrile Thermally Stimulated Discharge Currents from Polyacrylonitrile. **13**, 101–115 (1977).
125. Cai, T., Yang, Y. & Bi, E. Preparation of high-performance polyacrylonitrile piezoelectric thin film by temperature control. *Reactive and Functional Polymers* vol. 154 (2020).
126. Hammami, H., Arous, M., Lagache, M. & Kallel, A. Experimental study of relaxations in unidirectional piezoelectric composites. *Compos. Part A Appl. Sci. Manuf.* **37**, 1–8 (2006).
127. Linares, A. *et al.* Broad-Band Electrical Conductivity of High Density Polyethylene Nanocomposites with Carbon Nanoadditives: Multiwall Carbon Nanotubes and Carbon Nanofibers. doi:10.1021/ma801410j.

128. Tjong, S. C., Liang, G. D. & Bao, S. P. Electrical behavior of polypropylene/multiwalled carbon nanotube nanocomposites with low percolation threshold. *Scr. Mater.* **57**, 461–464 (2007).
129. Kharchenko, S. B., Douglas, J. F., Obrzut, J., Grulke, E. A. & Migler, K. B. Flow-induced properties of nanotube-filled polymer materials. *Nat. Mater.* **3**, 564–568 (2004).
130. Warren, H., Gately, R. D., O'Brien, P., Gorkin, R. & in het Panhuis, M. Electrical conductivity, impedance, and percolation behavior of carbon nanofiber and carbon nanotube containing gellan gum hydrogels. *J. Polym. Sci. Part B Polym. Phys.* **52**, 864–871 (2014).
131. Daraghme, A. *et al.* A Study of Carbon Nanofibers and Active Carbon as Symmetric Supercapacitor in Aqueous Electrolyte: A Comparative Study. *Nanoscale Res. Lett.* **12**, (2017).
132. Li, T. *et al.* One-pot synthesis and electrochemical properties of polyaniline nanofibers through simply tuning acid–base environment of reaction medium. *Electrochim. Acta* **249**, 33–42 (2017).
133. Sidhu, N. K. & Rastogi, A. C. Bifacial carbon nanofoam-fibrous PEDOT composite supercapacitor in the 3-electrode configuration for electrical energy storage. *Synth. Met.* **219**, 1–10 (2016).
134. Yu, S. & Myung, N. V. Minimizing the Diameter of Electrospun Polyacrylonitrile (PAN) Nanofibers by Design of Experiments for Electrochemical Application. *Electroanalysis* **30**, (2018).
135. Attia, A., Zikalova, M., Pospisil, L. & Kavan, L. Electrochemical impedance spectroscopy of mesoporous Al-stabilized TiO₂ (anatase) in aprotic medium. doi:10.1007/s10008-006-0256-2.

3 DNA-Guided Assembly of a Five-Component Enzyme Cascade for Enhanced Conversion of Cellulose to Gluconic Acid and Hydrogen Peroxide

This chapter is based on: Chen, Q., Yu, S., Myung, N. & Chen, W. DNA-guided assembly of a five-component enzyme cascade for enhanced conversion of cellulose to gluconic acid and H₂O₂. *J. Biotechnol.* **263**, 30–35 (2017).

3.1 Abstract

Enzymatic fuel cells have received considerable attention because of their potential for direct conversion of abundant raw materials such as cellulose to electricity. The use of multi-enzyme cascades is particularly attractive as they offer the possibility of achieving a series of complex reactions at higher efficiencies. Here we reported the use of a DNA-guided approach to assemble a five-component enzyme cascade for direct conversion of cellulose to gluconic acid and H₂O₂. Site-specific co-localization of β -glucosidase and glucose oxidase resulted in over 11-fold improvement in H₂O₂ production from cellobiose, highlighting the benefit of substrate channeling. Although a more modest 1.5-fold improvement in H₂O₂ production was observed using a five-enzyme cascade, due to H₂O₂ inhibition on enzyme activity, these results demonstrated the possibility to enhance the production of gluconic acid and H₂O₂ directly from cellulose by DNA-guided enzyme assembly.

3.2 Introduction

Fuel cells are potential alternative to thermo-mechanical power generation processes by directly converting chemical fuels into electricity. Even though the technology has been around for decades, fuel cells are still not economically competitive because expensive and nonrenewable noble metals are typically used as catalysts. In addition, metallic catalysts must be used at high temperatures and can be deactivated by trace amounts of impurities such as CO and sulfur in the fuels.¹ On the other hand, biofuel cells^{2,3} that utilize enzymes can effectively catalyze redox reactions of abundant raw materials (e.g. glucose) to electrical energy under ambient conditions and neutral pH. In contrast to noble metals, enzymes are renewable and the cost of production can be very low, as enzymes can be economically produced easily by large-scale fermentation.

Past efforts on enzyme fuel cells have been focusing on the use of an individual enzyme to oxidize the substrate.⁴ Unfortunately, the use of a single enzyme often limits the number of released electrons due to incomplete fuel oxidation. For instance, the conversion of methanol to formaldehyde by alcohol dehydrogenase releases only two of the six available electrons, while the complete oxidation of methanol to CO₂ using a sequential three-enzyme oxidation system generates six electrons for fuel-cell applications.⁵ In an effort to address this shortcoming, many researchers have incorporated multi-enzyme cascades for more complete oxidization of fuels that are both abundant and renewable.⁶⁻⁸

Cellulose, one of the most abundant natural resources on earth, has been the focus of considerable interest as a renewable energy source.⁹ Although extensive research efforts

have been made toward the development of glucose oxidase (GOx)-based fuel cells using glucose as the fuel,¹⁰⁻¹² progress toward the use of cellulose as a substrate has been lagging. Recently, cellulose has been used as the fuel in a microbial fuel cell (MFC) for the direct electricity generation^{13,14} using both cellulolytic and exoelectrogenic microorganisms. More importantly, it has been shown that addition of cellulases to increase the hydrolysis of cellulose can substantially improve the overall power output to a level achieved using the same amount of glucose.¹⁵ This result clearly indicates the importance of cellulose hydrolysis on the overall fuel cell performance.

Cellulosomes are multi-enzyme systems found in many anaerobic bacteria for efficient degradation of cellulose to glucose.¹⁶ Endoglucanases, exoglucanases, and β -glucosidases are organized in close proximity on a scaffold via the high-affinity cohesin-dockerin interaction for synergistic digestion of cellulose.¹⁷ Inspired by cellulosome systems, synthetic protein scaffolds based on cohesin-dockerin interaction have been developed for efficient enzymatic reaction.¹⁸⁻²⁰ However, truncation of protein scaffold becomes significant when scaffold sizes increase, which limits the complexity of synthetic enzymatic systems.²¹

DNA is a promising scaffold for immobilization of enzymes based on its programmable hybridization rule and predictable hybridized structures.²² More importantly, DNA scaffolds provide the unique benefit of site-specific enzyme organization, which could have a significant effect when the diffusion of intermediates is the determining factor for cascade enzymatic reactions.^{18,23,24} Recently, a DNA-guided approach for enzyme fuel cell applications has been reported in which the mediator

ferrocene and glucose oxidase (GOx) were coupled to a gold electrode based on DNA hybridization.^{24,25} By simply switching the positioning of ferrocene on the DNA scaffold, a strong effect on the rate of glucose oxidation was observed. This example demonstrates the importance of using DNA to control the order of assembly for enzyme fuel cell applications.

Motivated by these examples, our goal is to demonstrate the possibility of using site-specific organization of cellulases and GOx onto a synthetic DNA template for the efficient conversion of cellulose to gluconic acid and H₂O₂ (Figure 3.1).

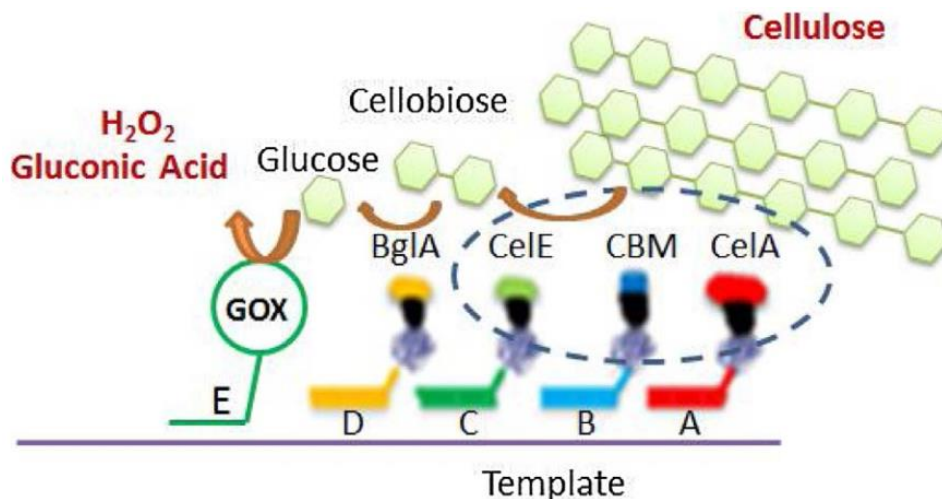


Figure 3.1 Schematic of a DNA-guided five-enzyme cascade for direct conversion of cellulose to gluconic acid and H₂O₂.

In our design, three cellulosomal components, CelA (endoglucanase), CelE (exoglucanase), and CBM (cellulose binding module), were used to first convert cellulose to the disaccharide, cellobiose, which was subsequently converted to glucose by the last cellulosomal component, BglA (β -glucosidase) and finally to gluconic acid and H₂O₂ by glucose oxidase (GOx). Although the synergistic effect of synthetic cellulosome on

cellulose hydrolysis has been well documented,^{26,27} it was not clear whether a similar beneficial effect could be obtained by channeling glucose between BglA and GOx by DNA-guided assembly. As the current generated by GOx -based fuel cells depends on how fast H₂O₂ is generated,²⁴ we focused our investigation on the effect of enzyme assembly on enhancing H₂O₂ generation.

3.3 Materials and methods

3.3.1 Protein expression and conjugation with DNA linkers

The four cellulosomal components (CelA-ELP-Halo, CBM-ELP-Halo, CelE-ELP-Halo, BglA-ELP-Halo) were constructed as reported.¹⁸ All four proteins were expressed in *E. coli* BLR in TB medium supplemented with 50 µg/mL kanamycin at 37 °C. The cultures were transferred to 25 °C shaker for overnight leaky expression when the OD₆₀₀ reached 1. Cells were harvested and resuspended in PBS for sonication. The cell debris was removed by centrifugation for 10 min at 4 °C. Two cycles of ELP purification were conducted to purify the proteins from cell lysis. 1 M Na₂SO₄ was added to protein samples to induce inverse-phase transition of ELP. The proteins samples were incubated at 37 °C for 10 min and centrifuged for 10 min in 37 °C. The supernatants were removed and the pellets containing ELP proteins were resuspended in PBS and incubated on ice for resolubilization. Centrifugation at 4 °C was used to remove insoluble proteins in the pellet and the supernatant containing ELP proteins were collected for DNA conjugation.

The DNA linkers were ordered with a 5' amine group. They were first modified with a chlorohexane (CH) ligand (Promega P675A) for HaloTag attachment by mixing the CH ligand and DNA linkers at a molar ratio of 30:1. The mixture was incubated at room temperature for 4 h. To purify CH-conjugated DNA and remove excessive CH ligands, a 3000 DA ultrafiltration column (Vivaspin 500, Sartorius Stedim Biotech) was used for purification. The purified DNA linkers were then mixed with ELP purified cellulase components for conjugation via HaloTag at a molar ratio of 3:1 overnight at 4 °C. The excessive DNA linkers were removed by ELP purification. 10% SDS-PAGE was used to check the conjugation efficiency.

Glucose oxidase (GOx) from *Aspergillus niger* was purchase from Sigma-Aldrich (G2133). The DNA linker for GOx was modified with a 5' thiol group. Sulfo-EMCS (Sigma-Aldrich 803235) was used as the cross linker for conjugation. Thiolated DNA linkers at 25 µM were incubated with 25 mM DTT for 2 h at room temperature to reduce possible disulfide linkage between DNA linkers. A 3000 DA ultrafiltration column was used to purify DNA linkers. GOx at 50 µM was mixed with 5 mM sulfo-EMCS in PBS buffer (pH 7.4) at room temperature for 6 h.

A 50 kDa centrifugal column (EMD Millipore, Amicon UltraUFC505096) was used to remove the excessive sulfo-EMCS. The treated DNA linkers and purified GOx were mixed at 1:1 molar ratio for 2 h at room temperature. The conjugation efficiency of DNA linker to GOx was evaluated by 8% native gel running at 100 V for 1 h.

3.3.2 Proteins assembly onto the DNA template

The sequences of DNA template and linkers are listed in Table 3.1 with the corresponding regions in same color coding.

Table 3.1 List of DNA sequences used in this study.

Template	GAGAGTCAGTCAGGAATTTTTAAAGGAGGGAGGGGAATTTTTACAGC GAGCGTCTACATTTTTACACCAGCCAGCCAACTTTTTGATTGACTGCT ACGTATTTTT
LinkerA	AAAAATTCCTGACTGACTCTC
LinkerB	AAAAATTCCTCCCTCCCTCCTT
LinkerC	AAAAATGTAGACGCTCGCTGT
LinkerD	AAAAAGTTGGCTGGCTGGTGT
LinkerE	AAAAATACGTAGCAGTCAATC
BlockerA	GAGAGTCAGTCAGGAATTTTT
BlockerB	AAAGGAGGGAGGGGAATTTTT
BlockerC	ACAGCGAGCGTCTACATTTTT
BlockerD	ACACCAGCCAGCCAACTTTT
BlockerE	GATTGACTGCTACGTATTTTT

To assemble DNA-conjugated proteins onto the DNA template, the proteins and DNA template were mixed at 1:1 molar ratio for 1 h at room temperature. Binding was detected by electromobility shift assays by running the samples on a 0.8% agarose gel at 90 V for 30 min.

3.3.3 Measurements of enzyme activities

To evaluate the H₂O₂ production rate from BglA and GOx, 50 nM enzymes were incubated with 20 mM cellobiose (equivalent to 40 mM glucose) and the H₂O₂ produced was detected kinetically at OD570 nm using the glucose oxidase activity assay kit (Sigma MAK097).

To evaluate the glucose production rate from the four cellulosomal components, 1 μM enzymes were incubated with 8 g/L phosphoric acid swollen cellulose (PASC, equivalent to 40 mM glucose). PASC was prepared from Avicel PH101 (Sigma) as previously described (Tsai et al., 2009). The glucose concentration was measured using a glucose (HK) assay kit (Sigma GAHK20) at various time points. The pH of the reaction buffer was adjusted using 100 mM citric acid-sodium citrate buffer.

To measure H_2O_2 production rate from the 5-enzyme system, 1 μM enzymes were incubated with 8 g/L PASC. The H_2O_2 concentration samples were collected periodically measured using the glucose oxidase activity assay kit.

3.4 Results and discussion

3.4.1 Protein conjugation with DNA linkers

We have previously demonstrated that CelA (endoglucanase from *Clostridium Thermocellum*), CBM (the carbohydrate binding module from *Clostridium Thermocellum*), CelE (exoglucanase from *Clostridium Cellulolyticum*), and BglA (β -glucosidase from *Clostridium Thermocellum*) can be assembled on the same DNA template via their corresponding conjugated DNA linkers (Figure 3.1) to achieve enhanced hydrolysis of cellulose.¹⁸ In all cases, a self-labeling HaloTag²⁸ was used for covalent attachment of chlorohexane (CH)-modified DNA linkers in order to minimize enzyme deactivation. Based on protein sizes,^{29,30} DNA linkers of 21 base pairs in length were used to assemble the cellulosomal components and GOx onto a 105 bp template.

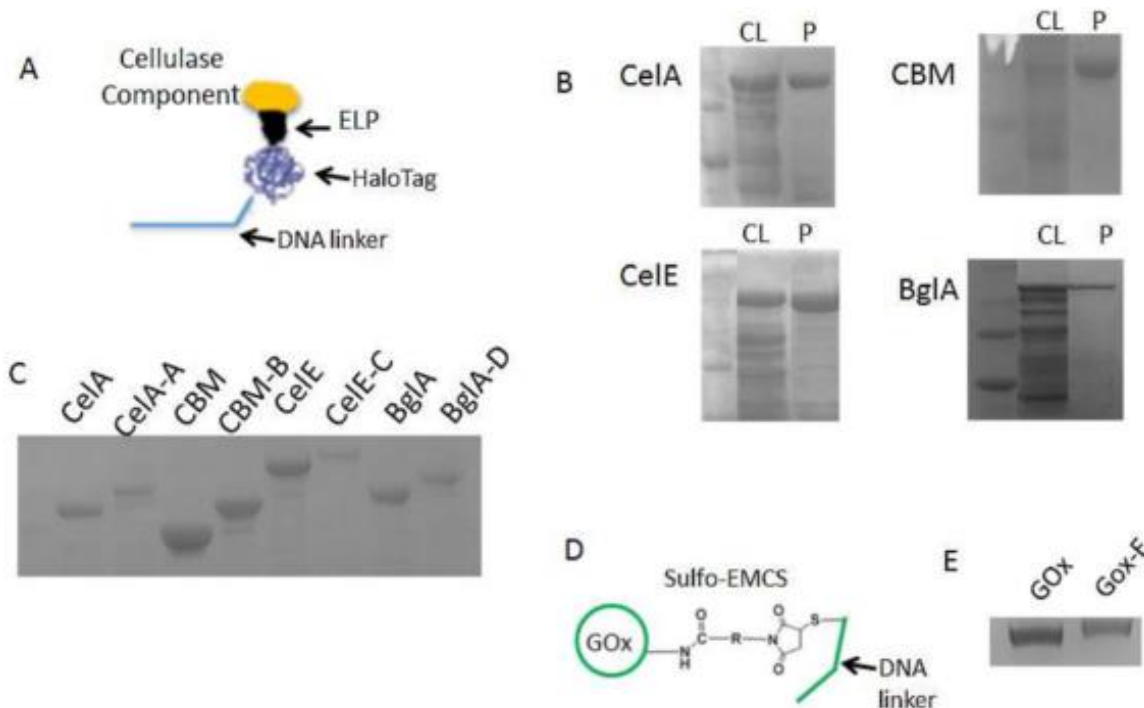


Figure 3.2 Protein conjugation with DNA linkers. (A) Conjugation of a DNA linker onto each cellulosomal component using the N-terminus HaloTag. (B) Expression and purification of each cellulosomal component. CL: cell lysate, P: purified protein. (C) Confirmation of DNA conjugation onto the cellulosomal components by 10% SDS-PAGE. Presence of a slower mobility band confirmed the successful conjugation. (D) Conjugation of a DNA linker to GOx using the well-known EDC chemistry. (E) Confirmation of GOx conjugation with a DNA linker by 10% native acrylamide gel.

As reported previously, the four cellulosomal components were fused to an elastin like polypeptides (ELP) tag at the N-terminus for easy purification, and a HaloTag at the C-terminus for specific conjugation to DNA linkers (Figure 3.2(a)).^{18,31} The presence of ELP enabled the easy purification of proteins and protein-DNA conjugates using two cycles of thermal precipitation and resolubilization.³² After expression and purification of the cellulosomal components via ELP purification (Figure 3.2(b)), 3-fold molar excess of chlorohexane-modified DNA linkers were incubated with the corresponding purified proteins. Two more cycles of thermal precipitation and resolubilization were used to remove excessive DNA linkers. Based on SDS-PAGE analysis (Figure 3.2(c)), the

conjugation efficiency was close to 100% in all cases as indicated by the slower migrating DNA-protein conjugates as compared to unconjugated proteins.

Since GOx from *Aspergillus niger* cannot be produced in large quantities in *E. coli* without refolding,³³ commercial GOx was conjugated with a DNA linker via the well-known sulfo-EMCS chemistry (Figure 3.2(d)).^{34,35} Size-exclusion centrifugal column was used to remove excessive DNA linkers after conjugation. Again, successful conjugation was confirmed by native gel and the conjugation efficiency was about 100% (Figure 3.2(e)).

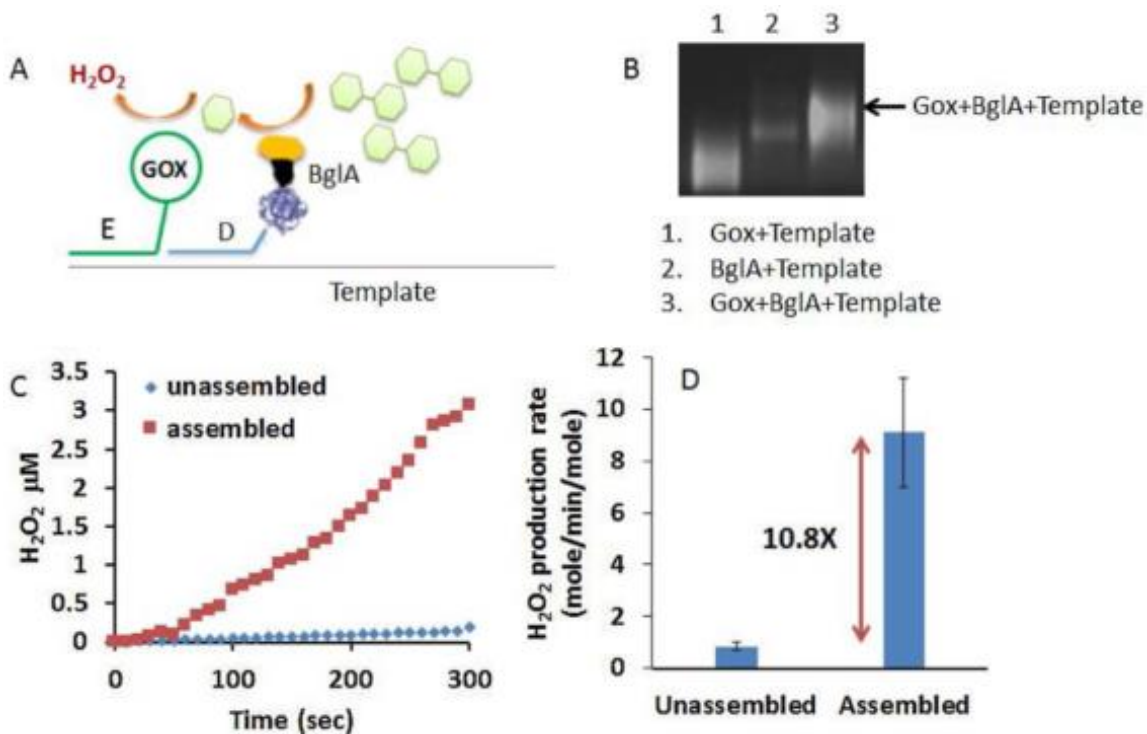


Figure 3.3 (a) Production of gluconic acid and H₂O₂ by BglA and GOx. (b) Confirmation of BglA and GOx assembly on agarose gel. (c) H₂O₂ production for either assembled or unassembled BglA and GOx. (d) The rate of H₂O₂ production for either assembled or unassembled BglA and GOx.

3.4.2 Enhanced H₂O₂ production by assembled BglA and GOx

Since the synergistic effect of cellulosome on cellulose hydrolysis has been demonstrated before,^{20,36} we first investigated the impact of enzyme assembly on the conversion of cellobiose to gluconic acid and H₂O₂ by BglA and GOx. In this cascade reaction, cellobiose is first converted to glucose, which is sequentially converted to gluconic acid and H₂O₂ by GOx (Figure 3.3(a)). Since the reported K_m for GOx is 10 mM,³⁷ this very low affinity toward glucose may significantly limit the cascade reaction due to the very low local concentration of glucose. It is possible that the direct channeling of glucose between BglA and GOx may partially overcome this limitation.

To assess this possibility, the rate of H₂O₂ production was monitored for both assembled and unassembled BglA and GOx. The assembly of DNA-conjugated GOx and BglA onto the same DNA template were first evaluated by agarose gel (Figure 3.3(b)). Due to the co-assembly of BglA and GOx, the resulting complex migrated slower than the single assembly complexes formed by hybridizing with either BglA or GOx alone. For the control experiment where BglA and GOx were not assembled on the same DNA template, a DNA blocker that is complimentary to the corresponding DNA linker was added to prevent unspecific association of the two proteins and to avoid any potential stabilization effect by hybridization. The rate of H₂O₂ production from cellobiose was monitored using a glucose oxidase activity assay kit (Figure 3.3(c)). Under this condition, barely any H₂O₂ production was detected for the unassembled enzyme mixture, while the production rate was almost 11-fold higher for the assembled BglA/GOx complex (Figure 3.3(d)). This observation

highlights the importance of site-specific assembly in controlling enzyme proximity and in enhancing glucose transfer between BglA and GOx for better H₂O₂ production.

3.4.3 Conversion of cellulose to H₂O₂ by the five-enzyme assembly

After confirming the benefit of enzyme proximity on the conversion of cellobiose, we further investigated the effect of enzyme assembly on the overall conversion of cellulose to gluconic acid and H₂O₂. The optimum reaction conditions for the five-enzyme system were first explored. GOx has a reported reaction rate that is 1000-fold faster than the cellulases used with an optimum reaction condition at pH 5 and 37 °C.^{38,39} As GOx is not the limiting step in converting cellulose to H₂O₂, the reaction conditions of the cellulosomal components were compared at room temperature and 37 °C and at pH values from 4 to 7.

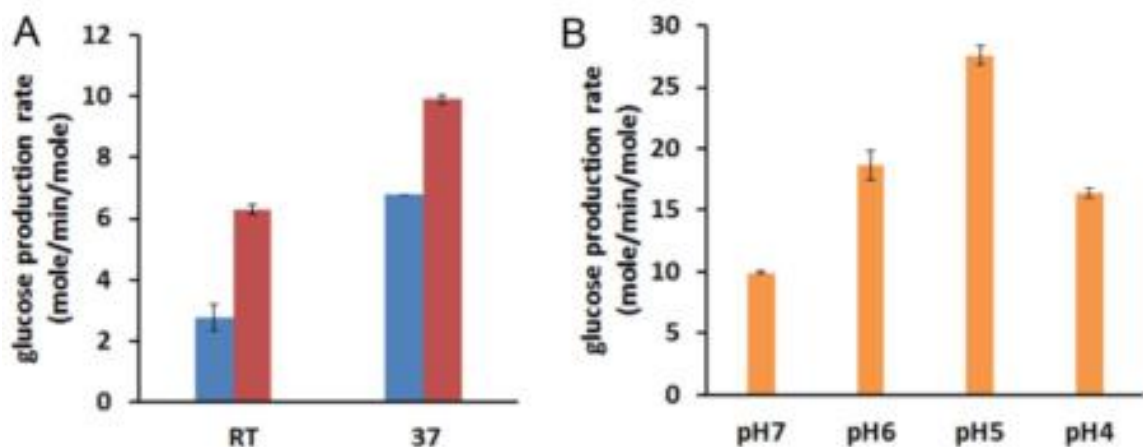


Figure 3.4 Effect of temperature (a) and pH (b) on glucose production by either unassembled (blue) or assembled (red) CelA, CBM, CelE and BglA. (For interpretation of the references to color in this figure legend, the reader is referred to the web version of this article.)

Cellulose was supplied as the substrate and the glucose concentration was measured periodically to determine the glucose production rate. While a 2-fold faster glucose production rate was observed for the assembled enzymes at room temperature (Figure 3.4(a)), a result consistent with that reported previously, the enhancement was only 1.5-fold at 37 °C. This result is not surprising as the benefit of substrate channeling is the more prominent at lower temperatures with less random diffusion.⁴⁰ The effect of pH was further investigated with the assembled enzymes and the optimum condition was identified at pH 5 (Figure 3.4(b)).

Using the optimized conditions, we proceeded to evaluate the conversion of cellulose to gluconic acid and H₂O₂ using the five-enzyme assembly. Assembly of the five proteins onto a single DNA template was evaluated by agarose gel and as expected, the complex migrated much slower when more proteins were assembled on the DNA template (Figure 3.5(a)). After incubating with cellulose, the H₂O₂ concentrations were measured periodically. Consistent with the increase in glucose production, the overall H₂O₂ production rate was improved by 1.5-fold with the assembled enzymes. This improvement is significantly lower than the 11-fold enhancement observed using cellobiose as the substrate for the BglA and GOx bi-enzyme system. One plausible reason is the well-known H₂O₂ inhibition on enzyme activity, which can play a role in reducing the overall reaction rate and activity enhancement by enzyme assembly.⁴¹ This inhibition effect is further supported by a significantly lower level of glucose produced in 3 h using the five-enzyme cascade (58.4 μM) vs the four-enzyme cascade (233.3 μM). Nevertheless, our results demonstrated the possibility of enhanced production of gluconic acid and H₂O₂ directly

from cellulose using a five-enzyme cascade assembled onto a single DNA template. Further optimization is necessary to improve the overall enhancement for more practical applications.

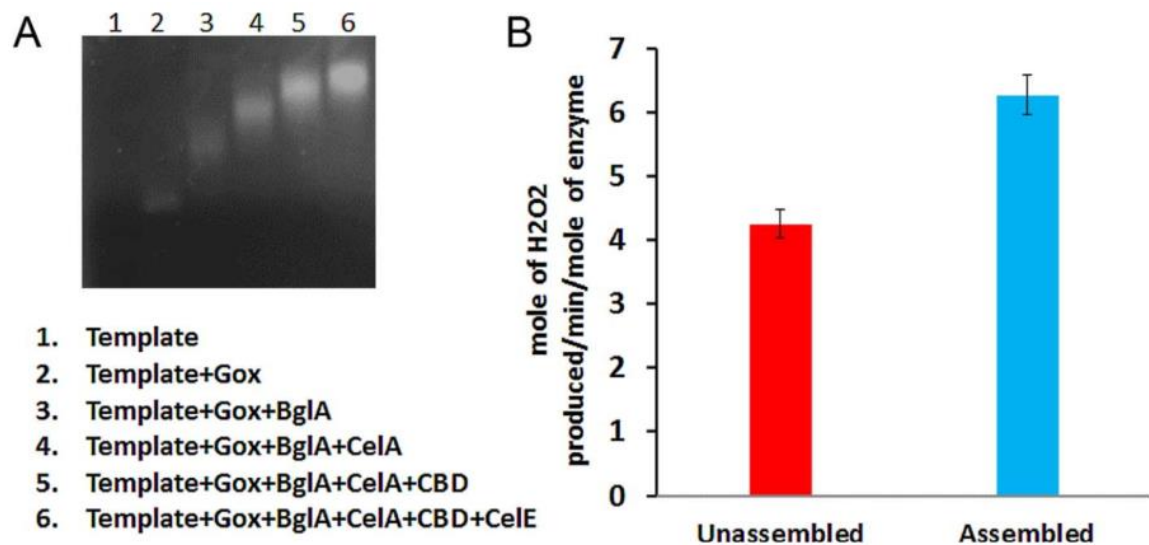


Figure 3.5 Enhanced H₂O₂ production from cellulose using an assembled five-enzyme cascade. (A) Confirmation of five-enzyme assembly by agarose gel. (B) Comparison of H₂O₂ production using either the assembled or unassembled five-enzyme system.

3.5 Conclusion

In conclusion, we demonstrated the direct conversion of cellulose to gluconic acid and H₂O₂ using a five-enzyme cascade. Site-specific colocalization of BglA and GOx using DNA-guided assembly resulted in over 11-fold improvement in H₂O₂ production, highlighting the benefit of substrate channeling. However, the level of enhancement is substantially less using the five-enzyme cascade, likely the result of activity imbalance and H₂O₂ inhibition. It is expected that the removal of H₂O₂ can reduce the toxic effect on enzyme activities, which can be accomplished by incorporating both an anode (GOx producing electron) and a cathode in the cellulosic fuel cell system.^{42,43} To match the higher

reaction rate of GOx, longer DNA templates can be generated to varying the ratio of cellulases and GOx in order to further fine-tune the overall reaction rate.¹⁸

3.6 References

1. Kim, J., Jia, H. & Wang, P. Challenges in biocatalysis for enzyme-based biofuel cells. *Biotechnology Advances* vol. 24 296–308 (2006).
2. Minteer, S. D., Liaw, B. Y. & Cooney, M. J. Enzyme-based biofuel cells. *Curr. Opin. Biotechnol.* **18**, 228–234 (2007).
3. Ramanavicius, A., Kausaite, A. & Ramanaviciene, A. Enzymatic biofuel cell based on anode and cathode powered by ethanol. **24**, 761–766 (2008).
4. Moehlenbrock, M. J., Toby, T. K., Waheed, A. & Minteer, S. D. Metabolon catalyzed pyruvate/air biofuel cell. *J. Am. Chem. Soc.* **132**, 6288–6289 (2010).
5. Addo, P. K., Arechederra, R. L. & Minteer, S. D. Evaluating Enzyme Cascades for Methanol/Air Biofuel Cells Based on NAD⁺-Dependent Enzymes. *Electroanalysis* **22**, 807–812 (2010).
6. Liu, F., Banta, S. & Chen, W. Functional assembly of a multi-enzyme methanol oxidation cascade on a surface-displayed trifunctional scaffold for enhanced NADH production. *Chem. Commun.* **49**, 3766–3768 (2013).
7. Siu, K. H. *et al.* Synthetic scaffolds for pathway enhancement. *Curr. Opin. Biotechnol.* **36**, 98–106 (2015).
8. Sokic-Lazic, D., Arechederra, R. L., Treu, B. L. & Minteer, S. D. Oxidation of biofuels: Fuel diversity and effectiveness of fuel oxidation through multiple enzyme cascades. *Electroanalysis* **22**, 757–764 (2010).
9. Liao, J. C., Mi, L., Pontrelli, S. & Luo, S. Fuelling the future: Microbial engineering for the production of sustainable biofuels. *Nature Reviews Microbiology* vol. 14 288–304 (2016).
10. Du Toit, H. & Di Lorenzo, M. Glucose oxidase directly immobilized onto highly porous gold electrodes for sensing and fuel cell applications. *Electrochim. Acta* **138**, 86–92 (2014).
11. Korkut, S. & Kilic, M. S. Power improvement of enzymatic fuel cells used for sustainable energy generation. *Environ. Prog. Sustain. Energy* **35**, 859–866 (2016).
12. Willner, I. *et al.* Electrical wiring of glucose oxidase by reconstitution of FAD-modified monolayers assembled onto Au-electrodes. *J. Am. Chem. Soc.* **118**, 10321–10322 (1996).

13. Ren, Z., Ward, T. E. & Regan, J. M. Electricity production from cellulose in a microbial fuel cell using a defined binary culture. *Environ. Sci. Technol.* **41**, 4781–4786 (2007).
14. Rezaei, F., Richard, T. L., Brennan, R. A. & Logan, B. E. Substrate-enhanced microbial fuel cells for improved remote power generation from sediment-based systems. *Environ. Sci. Technol.* **41**, 4053–4058 (2007).
15. Rezaei, F., Richard, T. L. & Logan, B. E. Enzymatic hydrolysis of cellulose coupled with electricity generation in a microbial fuel cell. *Biotechnol. Bioeng.* **101**, 1163–1169 (2008).
16. Bayer, E. A., Belaich, J.-P., Shoham, Y. & Lamed, R. The Cellulosomes: Multienzyme Machines for Degradation of Plant Cell Wall Polysaccharides. *Annu. Rev. Microbiol.* **58**, 521–554 (2004).
17. Bayer, E. A., Lamed, R., White, B. A. & Flint, H. J. From cellulosomes to cellulosomes. *Chem. Rec.* **8**, 364–377 (2008).
18. Sun, Q. & Chen, W. HaloTag mediated artificial cellulosome assembly on a rolling circle amplification DNA template for efficient cellulose hydrolysis. *Chem. Commun.* **52**, 6701–6704 (2016).
19. Sun, Q., Madan, B., Tsai, S. L., De Lisa, M. P. & Chen, W. Creation of artificial cellulosomes on DNA scaffolds by zinc finger protein-guided assembly for efficient cellulose hydrolysis. *Chem. Commun.* **50**, 1423–1425 (2014).
20. Tsai, S. L., Oh, J., Singh, S., Chen, R. & Chen, W. Functional assembly of minicellulosomes on the *Saccharomyces cerevisiae* cell surface for cellulose hydrolysis and ethanol production. *Appl. Environ. Microbiol.* **75**, 6087–6093 (2009).
21. Morais, S. *et al.* Deconstruction of lignocellulose into soluble sugars by native and designer cellulosomes. *MBio* **3**, (2012).
22. Pinheiro, A. V., Han, D., Shih, W. M. & Yan, H. Challenges and opportunities for structural DNA nanotechnology. *Nature Nanotechnology* vol. 6 763–772 (2011).
23. Han, D. *et al.* A logical molecular circuit for programmable and autonomous regulation of protein activity using DNA aptamer-protein interactions. *J. Am. Chem. Soc.* **134**, 20797–20804 (2012).
24. Piperberg, G., Wilner, O. I., Yehezkeli, O., Tel-Vered, R. & Willner, I. Control of bioelectrocatalytic transformations on DNA scaffolds. *J. Am. Chem. Soc.* **131**, 8724–8725 (2009).

25. Müller, J. & Niemeyer, C. M. DNA-directed assembly of artificial multienzyme complexes. *Biochem. Biophys. Res. Commun.* **377**, 62–67 (2008).
26. Tsai, S. L., DaSilva, N. A. & Chen, W. Functional display of complex cellulosomes on the yeast surface via adaptive assembly. *ACS Synth. Biol.* **2**, 14–21 (2013).
27. Tsai, S.-L., Park, M. & Chen, W. Size-modulated synergy of cellulase clustering for enhanced cellulose hydrolysis. *Biotechnol. J.* **8**, 257–261 (2013).
28. Los, G. V. *et al.* HaloTag: A novel protein labeling technology for cell imaging and protein analysis. *ACS Chem. Biol.* **3**, 373–382 (2008).
29. Alzari, P. M., Souchon, H. & Dominguez, R. The crystal structure of endoglucanase CelA, a family 8 glycosyl hydrolase from *Clostridium thermocellum*. *Structure* **4**, 265–275 (1996).
30. Hecht, H. J., Kalisz, H. M., Hendle, J., Schmid, R. D. & Schomburg, D. Crystal structure of glucose oxidase from *Aspergillus niger* refined at 2.3 Å resolution. *J. Mol. Biol.* **229**, 153–172 (1993).
31. Blackstock, D. & Chen, W. Halo-tag mediated self-labeling of fluorescent proteins to molecular beacons for nucleic acid detection. *Chem. Commun.* **50**, 13735–13738 (2014).
32. Kim, H. & Chen, W. A non-chromatographic protein purification strategy using Src 3 homology domains as generalized capture domains. *J. Biotechnol.* **234**, 27–34 (2016).
33. Witt, S., Singh, M. & Kalisz, H. M. Structural and kinetic properties of nonglycosylated recombinant *Penicillium amagasakiense* glucose oxidase expressed in *Escherichia coli*. *Appl. Environ. Microbiol.* **64**, 1405–1411 (1998).
34. Xin, L., Zhou, C., Yang, Z. & Liu, D. Regulation of an Enzyme Cascade Reaction by a DNA Machine. *Small* **9**, 3088–3091 (2013).
35. You, M. *et al.* Photon-regulated DNA-enzymatic nanostructures by molecular assembly. *ACS Nano* **5**, 10090–10095 (2011).
36. Tsai, S. L., Goyal, G. & Chen, W. Surface display of a functional minicellulosome by intracellular complementation using a synthetic yeast consortium and its application to cellulose hydrolysis and ethanol production. *Appl. Environ. Microbiol.* **76**, 7514–7520 (2010).

37. Karmali, K., Karmali, A., Teixeira, A. & Curto, M. J. M. Assay for glucose oxidase from *Aspergillus niger* and *Penicillium amagasakiense* by Fourier transform infrared spectroscopy. *Anal. Biochem.* **333**, 320–327 (2004).
38. Meng, Y. *et al.* Production and characterization of recombinant glucose oxidase from *Aspergillus niger* expressed in *Pichia pastoris*. *Lett. Appl. Microbiol.* **58**, 393–400 (2014).
39. Wong, C. M., Wong, K. H. & Chen, X. D. Glucose oxidase: Natural occurrence, function, properties and industrial applications. *Applied Microbiology and Biotechnology* vol. 78 927–938 (2008).
40. Wheeldon, I. *et al.* Substrate channelling as an approach to cascade reactions. *Nature Chemistry* vol. 8 299–309 (2016).
41. Bao, J., Furumoto, K., Yoshimoto, M., Fukunaga, K. & Nakao, K. Competitive inhibition by hydrogen peroxide produced in glucose oxidation catalyzed by glucose oxidase. *Biochem. Eng. J.* **13**, 69–72 (2003).
42. Barton, S. C., Gallaway, J. & Atanassov, P. Enzymatic biofuel cells for implantable and microscale devices. *Chem. Rev.* **104**, 4867–4886 (2004).
43. Rasmussen, M., Abdellaoui, S. & Minteer, S. D. Enzymatic biofuel cells: 30 years of critical advancements. *Biosens. Bioelectron.* **76**, 91–102 (2016).

4 Development of Bienzymatic Electrode as Concept Demonstration for Cellulolytic Anode with Multienzyme Cascade on DNA Scaffold

4.1 Abstract

Cellulose is one of the naturally abundant resources that can be used for various green sources of energy. To employ this raw material as fuel for enzymatic fuel cells, multiple cellulases and an oxidoreductase for its single block of sugar (i.e. glucose) could be combined in a bioanode. Previously, 3 cellulases, a cellulose-binding domain, and glucose oxidase (GOx) were site-specifically immobilized on a DNA scaffold to achieve the cascade reaction consisting of cellulose hydrolysis to glucose followed by glucose oxidation in aqueous solution. As a concept demonstration of implementing the five-enzyme cascade system for EFC application, a bienzymatic bioanode consisting of BglA (i.e. β -glucosidase) and commercial GOx was fabricated. Each enzyme was combined with a single-stranded DNA linker and then immobilized on a thiolated DNA template via hybridization. The DNA-immobilized bienzyme system was then reacted with gold nanoparticles, which acted as anchors to hold down the system on a multi-walled carbon nanotube-functionalized screen-printed carbon electrode surface. Once the electroactivity of GOx in the bienzymatic system was confirmed and compared to a GOx-only electrode, a concentration dependent current response was measured using cellobiose. Both the concentration-dependent current density profile and GOx activity assay suggested that cellobiose hydrolysis by BglA was the rate-limiting step. Preliminary results showed that

up to 87% of current density was retained after 7 days. Successful demonstration of the bienzymatic cascade-based electrode could readily lead to bioanodes and biocathodes functionalized with multienzyme cascade biocatalyst system for cellulolytic enzymatic fuel cell and more.

4.2 Introduction

Fuel cells are studied as one of the greener alternatives to the conventional energy production such as combustion of fossil fuels since they utilize renewable sources of energy like biomass and typically produce water as the only byproduct. Enzymatic fuel cells (EFCs), in particular, offer high specificity toward fuel and oxidant at anode and cathode, respectively, by employing isolated enzymes as biocatalysts, eliminating the need for separation membrane or compartmentalization of each electrode.

Early works on enzymatic fuel cells involved a single enzyme as biocatalyst, which led to a relatively low power density due to incomplete oxidation of fuel. Additionally, bulk electrodes exhibit low specific surface area that could lead to low enzyme loading as well as inefficient electron transfer. Furthermore, simple enzyme immobilization methods such as physisorption allowed for the biocatalysts to leach off the electrode surface over time, which reduces the stability of the EFCs. To enhance the performance of the EFCs, three main aspects can be engineered: the enzyme catalyst, the electron transfer from the enzyme redox center to the electrode, and the electrodes.

More recently, various methods have been studied to increase the power density and stability of EFCs. For example, instead of a typical two-step oxidation to gluconic acid, glucose was oxidized all the way to carbon dioxide by a cascade reaction driven by six enzymes combined on the anode, producing almost 47 times the power density than when a single enzyme was used.¹ Up to six electrons per one molecule of fuel were generated by an artificial enzyme cascade pathway consisting of four dehydrogenases, exhibiting 4.2-fold increase in current density than when one enzyme was used.² Similar studies were conducted by employing multiple enzymes for sequential oxidation reactions to increase the coulombic efficiency, imitating a naturally available multienzyme complex called cellulosome.³⁻⁷ Another method to enhance the EFC performance is to increase the specific surface area of the electrode, which poses a few advantages: (i) increased enzyme loading⁸; (ii) reduction of enzyme-to-electrode distance, thereby facilitating higher direct electron transfer rate⁹; and (iii) increased stability of enzyme immobilization¹⁰. Lastly, engineering of enzyme immobilization method could further enhance the electron transfer and stability of bioelectrodes.

Combining such methods widens the range of fuels to be used to more complex molecules like the naturally abundant cellulose. As it already presents uses as an environmentally friendly energy sources such as production of biofuels as well as fuel for microbial fuel cells, cellulose contains much potential to be used in EFCs as well. To achieve this, multiple cellulosomal enzymes – enzymes that hydrolyze cellulose; also referred to as cellulases – must be employed at once to break down the long chain to a single molecule of glucose, which has already been proven a popular choice of fuel in

EFCs. Following our previous work that clearly showed the synergistic effect of site-specific immobilization of cellulases and a commercial glucose oxidase (GOx) on a customized DNA scaffold for a sequential hydrolysis of cellulose followed by glucose oxidation,¹¹ this work presents a first step of concept demonstration of implementing the same five-enzyme cascade system on a bioanode.

4.3 Materials and Methods

4.3.1 Materials

Glucose oxidase (GOx, *Aspergillus Niger*) was purchased from Sigma Aldrich. Cellobiose (99%), D-glucose (anhydrous), N,N-dimethylformamide (DMF), sodium chloride (NaCl), potassium chloride (KCl), disodium phosphate (Na₂HPO₄), monopotassium phosphate (KH₂PO₄) were purchased from Fisher. Short COOH-functionalized multi-walled carbon nanotubes (MWNT-COOH, hereafter referred to as MWNT, OD 8-15 nm, length 0.5-2.0 μm) were purchased from Cheap Tubes. Carbon screen-printed electrodes, containing carbon as working and counter electrodes and silver as pseudo-reference electrode, were purchased from Metrohm USA. Gold nanoparticles with diameters 10 and 100 nm were graciously provided by Yadong Yin group at the Department of Chemistry in University of California Riverside.

4.3.2 Methods

Various concentrations of GOx and MWNT were dispersed in autoclaved Milli-Q water and DMF, respectively. MWNT dispersion in MWNT was achieved ultrasonically

for 2 hours. GOx solutions were stored in -20 °C until use. Phosphate buffer saline (PBS) was prepared by first dissolving 8 g NaCl, 0.2 g KCl, 1.44 g Na₂HPO₄, 0.245 g KH₂PO₄ in autoclaved Milli-Q water, followed by pH adjustment to 7.4 with either 1 M hydrochloric acid (HCl) or 1 M sodium hydroxide (NaOH). Glucose and cellobiose were each dissolved in autoclaved Milli-Q water and stored at room temperature until use.

4.3.2.1 Protein expression and conjugation with DNA linkers

BglA-ELP-Halo, a cellulosomal component that cleaves cellobiose in half to produce glucose, was constructed as reported. BglA was expressed in *E. coli* BLR in TB medium supplemented with 50 µg/mL kanamycin at 37 °C. The cultures were transferred to 25 °C shaker for overnight leaky expression when the OD₆₀₀ reached 1. Cells were harvested and resuspended in PBS for sonication. The cell debris was removed by centrifugation for 10 min at 4 °C. Two cycles of elastin-like polypeptide (ELP) purification were conducted to purify the proteins from cell lysis. 1 M Na₂SO₄ was added to protein samples to induce inverse-phase transition of ELP. The protein samples were then incubated at 37 °C for 10 min and centrifuged at 37 °C for 10 min. The supernatants were removed and the pellets containing ELP proteins were resuspended in PBS and incubated on ice for resolubilization. Then the sample was centrifuged at 4 °C to remove the insoluble proteins in the pellet, while the supernatant containing ELP proteins was collected for DNA conjugation.

The DNA linkers for BglA were ordered with a 5' amine group. They were first modified with a chlorohexane (CH) ligand (Promega P675A) for HaloTag attachment by

mixing the CH ligand and DNA linkers at a molar ratio of 30:1. The mixture was incubated at room temperature for 4 h. To purify CH-conjugated DNA and remove excessive CH ligands, a 3000 DA ultrafiltration column (Vivaspin 500, Sartorius Stedim Biotech) was used for purification. The purified DNA linkers were then mixed with ELP purified cellulase components for conjugation via HaloTag at a molar ratio of 3:1 overnight at 4 °C. The excessive DNA linkers were removed by ELP purification. 10% SDS-PAGE was used to check the conjugation efficiency.

The DNA linker for GOx was modified with a 5' thiol group. Sulfo-EMCS (Sigma-Aldrich 803235) was used as the cross linker for conjugation. Thiolated DNA linkers at 25 μ M were incubated with 25 mM DTT for 2 h at room temperature to reduce possible disulfide linkage between DNA linkers. A 3000 DA ultrafiltration column was used to purify DNA linkers. GOx at 50 μ M was mixed with 5 mM sulfo-EMCS in PBS buffer (pH 7.4) at room temperature for 6 h. A 50 kDa centrifugal column (EMD Millipore, Amicon UltraUFC505096) was used to remove the excessive sulfo-EMCS. The treated DNA linkers and purified GOx were mixed at 1:1 molar ratio for 2 h at room temperature.

4.3.2.2 Protein assembly onto DNA scaffold

The sequences of DNA template and linkers are listed in Table 4.1 with the corresponding regions color-coded. Thiolated DNA template was first reacted with gold nanoparticles at room temperature for 1 h. The DNA-conjugated proteins were then mixed with the template DNA-AuNP mixture at 1:1 molar ratio (protein-to-template DNA) for 1 h at room temperature.

Table 4.1 Sequence of DNA template and linkers used.

Sequence Name	Sequence
Seq 1	AAAAAACCTCAGCAATACTAACTGACGATGCATAAA
Main	GAGAGTCAGTCAGGAATTTTAAAGGAGGGAGGGGAATTTT TACAGCGAGCGTCTACATTTTACACCAGCCAGCCAACCTTTT TTTATGCATCGTCAGTTAG
BglI Linker	AAAAAGTTGGCTGGCTGGTGT
GOx Linker	AAAAAAAAAATATTGCTGAGGT

4.3.2.3 Enzymatic electrode fabrication and electroanalytical methods

Two types of enzymatic electrodes were fabricated in this work: i) proteins physisorbed onto MWNT dispersion; ii) DNA-conjugated proteins immobilized on gold nanoparticles dropcasted with MWNT dispersion. Both types of electrodes were fabricated by dropcasting of MWNT dispersion followed by protein solution, but the protein solution used for type (i) electrodes had the enzymes flowing freely in solution, while those used for type (ii) electrodes were site-specifically immobilized onto DNA scaffold according to the protocol laid out in sections 4.3.2.1 and 4.3.2.2. After each electrode was allowed to air dry, Nafion solution was dropcasted to prevent leaching. Electroanalytical methods were conducted in pH7.4 PBS, which was either deaerated with ultra-high purity nitrogen (UHP N₂, 99.999%) or aerated with compressed air. Gas was bubbled into the electrolyte at 250 sccm for at least 30 minutes before conducting experiments. Concentration of dissolved oxygen (DO) was measured with a DO meter (Oakton WD-35643-12) to confirm the deaeration/aeration. Cyclic voltammetry (CV) was conducted for 5 cycles sweeping the

potential ranging from 0.24 to -0.9 V vs. RE. Scan rate-dependent CV was carried out by varying scan rate from 10 to 200 mV/s, while it was fixed at 50 mV/s for concentration-dependent CV. Glucose oxidase activity assay (Sigma Aldrich, MAK097) was used according to the user guide to confirm the enzyme activity by monitoring the production of hydrogen peroxide as the byproduct of glucose oxidation.

Electroactive surface area, A , was estimated according to the Randles-Sevcik equation:

$$I_p = 26800n^{3/2}AD^{1/2}Cv^{1/2} \quad (\text{Equation 1})$$

Where I_p is the peak current, n is the number of electrons transferred, D is the diffusion coefficient, C is the concentration, and v is the scan rate. Peak current as a function of square root of scan rate was plotted for each electrode, and the slope of this curve was used as a means to correlate with the electroactive surface area, as A was the only variable.

4.4 Results and Discussion

4.4.1 Design of experiment (DOE) for enzymatic electrode fabrication

4.4.1.1 Confirmation of GOx activity on electrodes

Before determining any factors and their upper and lower limits for a DOE, GOx activity after electrode fabrication had to be confirmed. Simple physisorption of free GOx in solution with MWNT dispersion to facilitate electron transfer to the electrode surface was used, and the as-fabricated electrode was coated with a layer of Nafion to prevent

leaching. Cyclic voltammetry in deaerated PBS electrolyte (pH 7.4) in Figure 4.1 revealed several features. First, the height of the voltammogram measured by the difference between the maximum and minimum current density in the non-faradaic region increased more than 26 times after modification of GOx/MWNT mixture. This dramatic increase in voltammogram height was likely due to the high number of active site and double-layer capacitance, which were attributed to the presence of MWNT. Second, a pair of redox peaks at $E_{pa}=-0.41$ and $E_{pc}=-0.49$ V vs. Ag appeared after GOx/MWNT modification.

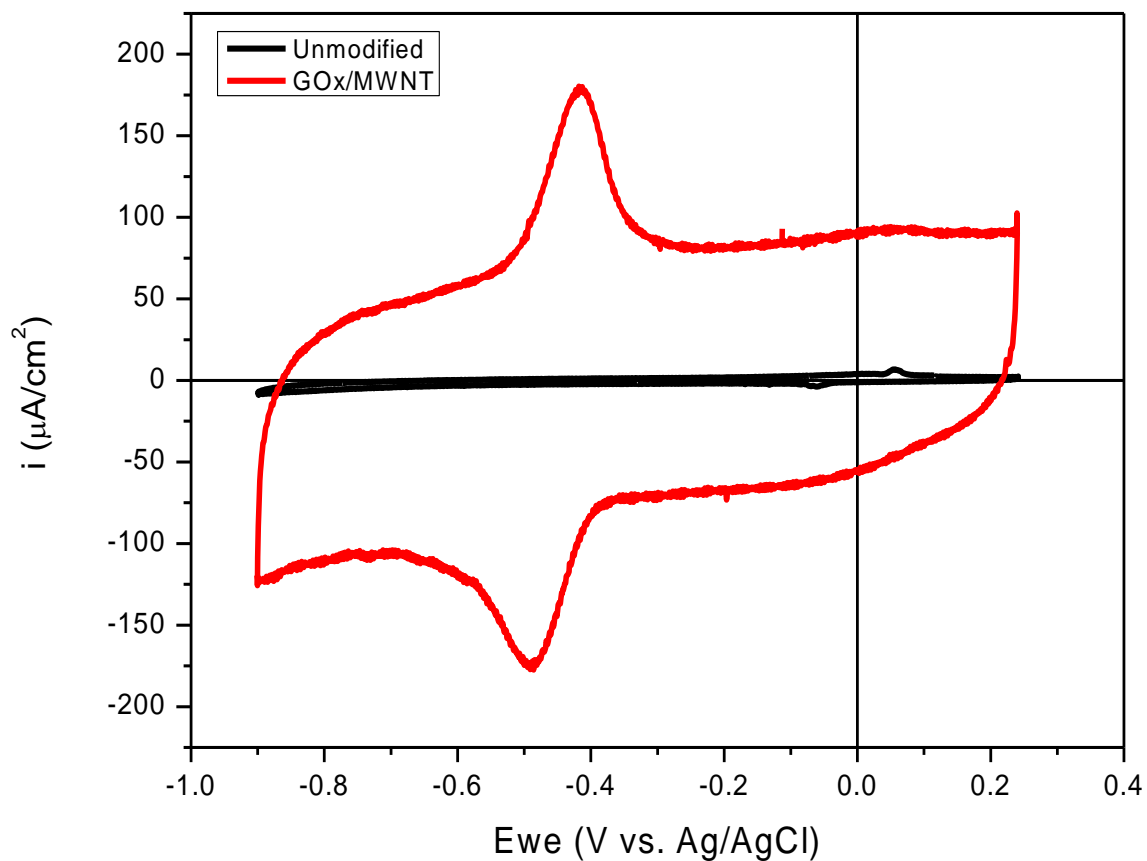
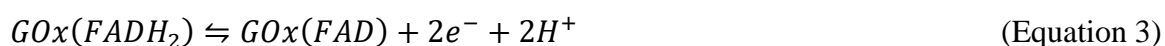
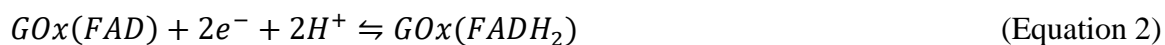


Figure 4.1 Cyclic voltammogram of electrode before and after modification with GOx and MWNT. CV was conducted in deaerated PBS, pH7.4, at 50 mV/s.

This was indicative of the redox of the FAD cofactor in the GOx, as E° calculated as the average of the anodic and the cathodic peaks was -0.44 V, which was very close to literature value of the redox potential of GOx.¹² Thus, the anodic and cathodic peak was each assigned to the following electrochemical equation:



The peak potential separation, ΔE_p , was 0.08/n V. Since the theoretical threshold for a reversible process is $\Delta E_p=0.059/n$ V, this process was characterized as quasi-reversible. In fact, scan-rate dependent CV (Figure 4.2) showed that both anodic and cathodic peaks shifted in less negative and more negative directions, respectively, with increasing scan rate, supporting the quasi-reversibility of the redox of GOx(FAD). As the peak current density was linearly correlated with the square root of the scan rate, Randles-Sevcik equation (Equation 1) could be used to estimate the electroactive surface area.

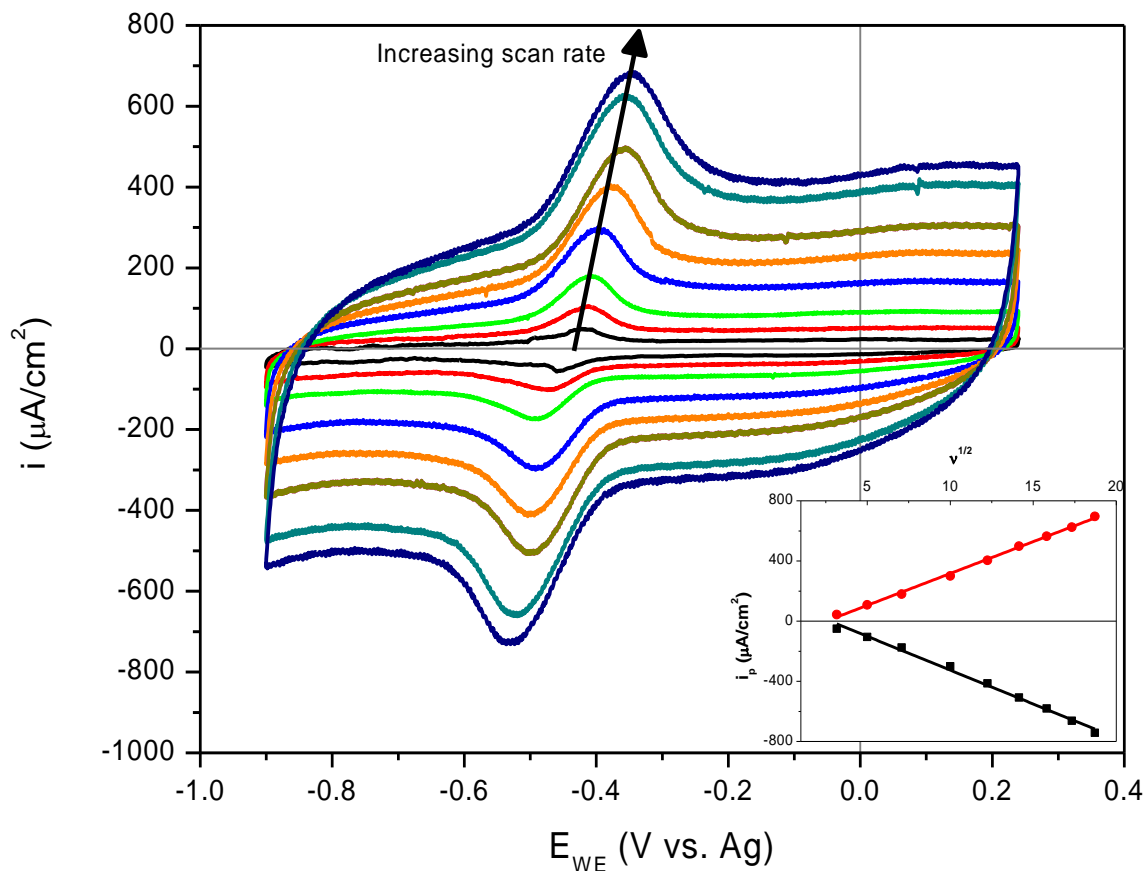


Figure 4.2 Scan rate-dependent cyclic voltammogram of electrode modified with GOx and MWNT. CV was conducted in deaerated PBS, pH7.4, at scan rates ranging from 10 to 350 mV/s. Inset shows linear correlation between peak current densities and square root of scan rate.

To further confirm the faradaic response was due to the redox of cofactor of GOx, CV was also conducted in an aerated electrolyte. This was because oxygen is a co-substrate for GOx, so an additional peak correlating to the reduction of oxygen due to its interaction with GOx cofactor was expected. As shown in Figure 4.3, the cathodic current density dramatically increased starting at around -0.2 V, and an additional peak at $E_{pc2} = -0.4$ V appeared. The pair of redox peaks shifted to $E^0 = -0.62$ V, possibly because more energy was

required to drive the redox reaction of GOx as some of the cofactor had reacted with oxygen at lower potentials.

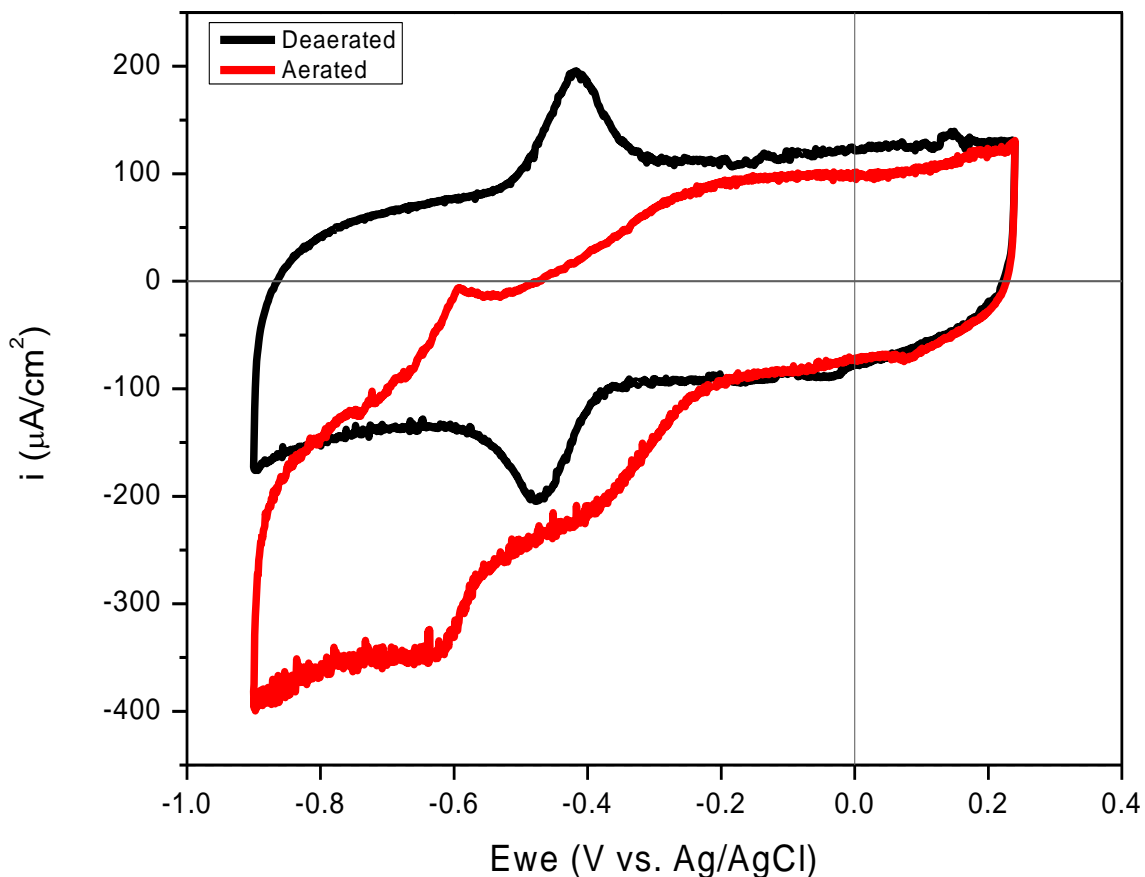


Figure 4.3 Cyclic voltammogram of electrode modified with GOx and MWNT in deaerated and aerated PBS, pH7.4. CV was conducted at 50 mV/s.

4.4.1.2 DOE 1: variation of concentration of MWNT and GOx

Once the electroactivity of the GOx on the electrode surface was confirmed, two electrode fabrication conditions – GOx and MWNT concentration – were varied based on a design of experiment (hereafter referred to as DOE1). As MWNT was thought to facilitate the electron transfer from the enzyme cofactor to the electrode surface, it was initially hypothesized that an increase in MWNT loading on the electrode could enhance the

electron transfer with larger specific surface area and better electrical contact. Additionally, the effect of increasing the enzyme loading on the electroactivity of the enzyme was of interest. It was hypothesized that there would be a certain point after which increasing the enzyme loading would not have any effect; once all of the MWNT on the electrode was covered with GOx, any additional amount of enzyme would not be electroactive as it is not close enough to the MWNT for an efficient electron transfer to the electrode.

Table 4.2 Summary of resulting parameters from cyclic voltammetry using working electrodes fabricated with conditions laid out by design of experiment 1 (DOE1). The anodic and cathodic peak densities were measured from CV conducted in deaerated PBS, pH7.4, at 50 mV/s. Slope of i_{pc} vs. $v^{1/2}$ curve is the absolute value.

DOE code	Design factors		Results from CV		
	[GOx] [mg/mL]	[MWNT] [mg/mL]	Anodic peak density, i_{pa} [$\mu\text{A}/\text{cm}^2$]	Cathodic peak density, i_{pc} [$\mu\text{A}/\text{cm}^2$]	Slope of i_{pc} vs. $v^{1/2}$ curve
--	10	0.4	180	-175	45
+-	50	0.4	329	-410	58
00	30	1.2	173	-176	62
-+	10	2.0	125	-157	48
++	50	2.0	414	-229	100

Anodic and cathodic peak current density as well as the slope of i_p vs. $v^{1/2}$ curve were chosen as the resulting electrode properties to investigate the effect of the DOE factors. (Table 4.2) DOE analysis of the cathodic peak current density as a function of DOE1 factors showed that the concentration of GOx had a slightly higher impact than the MWNT loading. (Figure 4.4(a)) As increase in [GOx] would lead to higher peak cathodic current density, this could first indicate that the maximum amount of GOx allowed on the electrode surface was not reached within the range of GOx concentration chosen for DOE1 and increasing amount of GOx was electroactive. Contrary to the other hypothesis, however,

MWNT loading had a competing effect on the cathodic peak current density. This could be attributed to higher amount of aggregates of the carbon nanotube with increasing MWNT concentration, which would not be an effective medium through which electron transfer could occur. The slope of the i_p vs. $v^{1/2}$ curve could be a better indication of the electroactivity of the electrode based on the Randles-Sevcik equation. (Figure 4.4(b)) The slope showed a positive trend as a function of both DOE factors, which suggested that both GOx and MWNT concentration should be increased for higher electroactive surface area. The opposite trend of cathodic peak current density and i_p - $v^{1/2}$ slope as a function of MWNT loading might be better explained with further studies with electroanalytical methods such as electrochemical impedance spectroscopy to shed light on the equivalent circuit on the electrode-electrolyte interface.

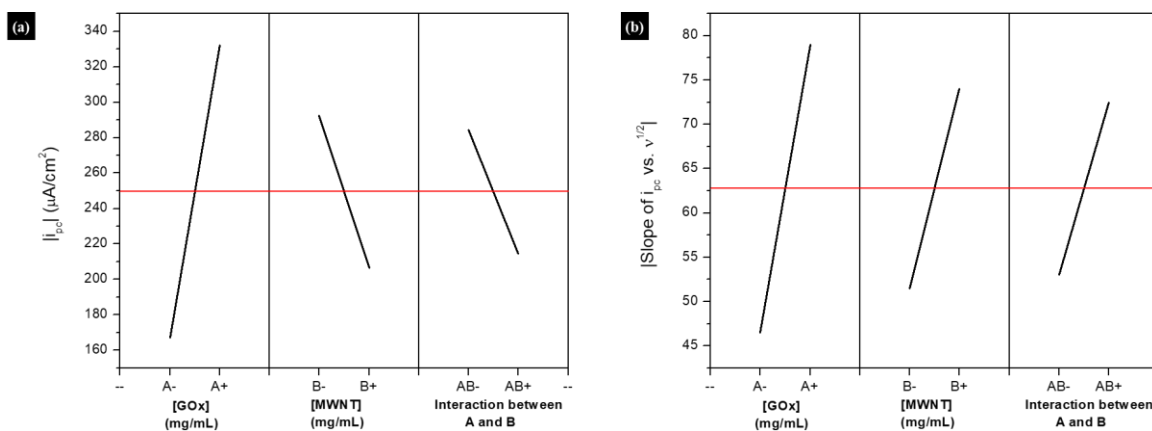


Figure 4.4 DOE analysis of (a) cathodic peak current density and (b) slope of i_{pc} vs. $v^{1/2}$ curve as a function of DOE1 factors.

4.4.1.3 DOE 2: variation of enzyme and protective layer

In order to better understand the effect of Nafion as well as the synergistic effect between MWNT and GOx on the electroactivity of the enzyme electrode, the number of

enzyme-MWNT layers and total volume of Nafion coating were varied according to another set of DOE (hereafter referred to as DOE2). The upper and lower limit were set based on one of the conditions used in DOE1 as the starting point: 5 alternating layers of GOx and MWNT, and 5 μL of Nafion. Concentration of GOx and MWNT were fixed at 10 and 0.4 mg/mL, respectively, and each layer of enzyme and MWNT was achieved by dropcasting 1 μL of MWNT dispersion followed by 1 μL of GOx solution. The GOx-MWNT layer was air dried almost completely before dropcasting the subsequent layer. The Nafion was dropcasted on top of the 5- or 1-layer enzyme-MWNT mixture after drying. Cyclic voltammetry with 4 samples fabricated according to DOE2 in deaerated PBS showed that the height of voltammogram was slightly higher with thinner Nafion coating at fixed number of GOx-MWNT layers. (Figure 4.5(a)) This suggested that Nafion could have hindered the signal from reaching deeper into the GOx-MWNT layer, overall reducing the double-layer characteristics typical of the MWNT.^{13,14}

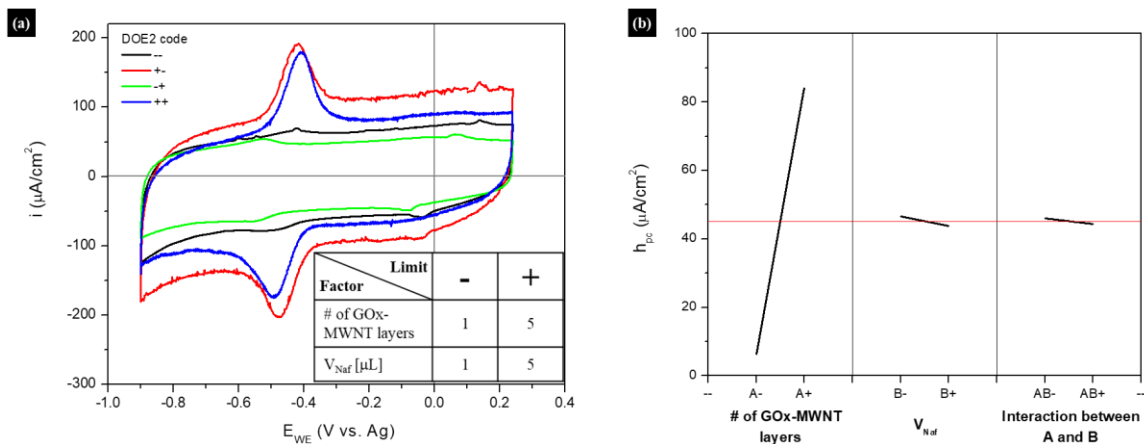


Figure 4.5 (a) Cyclic voltammogram of electrodes fabricated according to DOE2 (shown in inset table). CV was conducted in deaerated PBS, pH7.4, at 50 mV/s. (b) DOE analysis of cathodic peak height.

Despite the larger nonfaradaic current potentially reducing the sensitivity of the electrode, the peak heights of both anodic and cathodic peaks were higher with thinner Nafion coatings. However, the effect of Nafion on the peak heights was almost negligible compared to that of the number of enzyme-MWNT layers. Regardless of the volume of Nafion used, electrodes fabricated with 5 alternating layers of MWNT and GOx exhibited cathodic and anodic peak heights in 80's and 100's of $\mu\text{A}/\text{cm}^2$, respectively, while those with one alternating layer of MWNT and GOx showed cathodic and anodic peak heights registered at an order of magnitude lower. In fact, DOE analysis of cathodic peak height as a function of DOE2 factors showed the number of GOx-MWNT layers was the predominant factor, while the Nafion volume had virtually no effect. (Figure 4.5(b))

4.4.2 Bienzymatic system on DNA scaffold

As a concept demonstration of multienzyme cascade immobilized on DNA scaffold as an effective biocatalyst system, two enzymes – glucose oxidase and BglA – were site-specifically immobilized by DNA conjugation onto a template DNA scaffold. Hybridizing the ssDNA linker-conjugated enzymes with template DNA would not only increase the stability of the biocatalysts, but also allow for organization of the enzymes in a specific sequence to create the cascade effect. As the synergistic effect of site-specific immobilization of up to 5 enzymes (3 cellulases, GOx and cellulose-binding module) in solution was clearly shown in Chapter 3, the idea was to implement the same multienzyme system onto an anode surface to hydrolyze cellulose to glucose, which would then be catalytically oxidized by GOx to generate electricity. As a first step towards this goal,

electroactivity of bienzymatic electrode was demonstrated in this chapter with GOx-BglA immobilized on DNA scaffold.

Since the template DNA has been modified with a thiol group, which is well known to covalently bind to gold, a concept was drawn to utilize gold nanoparticles (AuNP) as anchors to weigh down the enzyme cascade systems onto the electrode surface. Therefore, two differently sized gold nanoparticles – 10 and 100 nm in diameter – were used as anchors. The enzyme system bound to the 10-nm AuNP is hereafter referred to as enzyme-DNA-AuNP(10), while that with 100-nm AuNP is enzyme-DNA-AuNP(100). Intuitively, larger nanoparticle would be more effective in weighing down the enzyme systems as it is heavier; furthermore, it might be possible that multiple strands of template DNA holding bienzyme systems could bind to a single nanoparticle, which would increase not only the weight of the enzyme-DNA-AuNP cluster but also the enzyme loading. Since the diameter of GOx is approximately 10 nm and the total length of the assembled enzyme-DNA system would be approximately 40 nm, it might be difficult for a 10-nm AuNP to accommodate for more than 1 unit of enzyme-DNA system as it is not rigid.

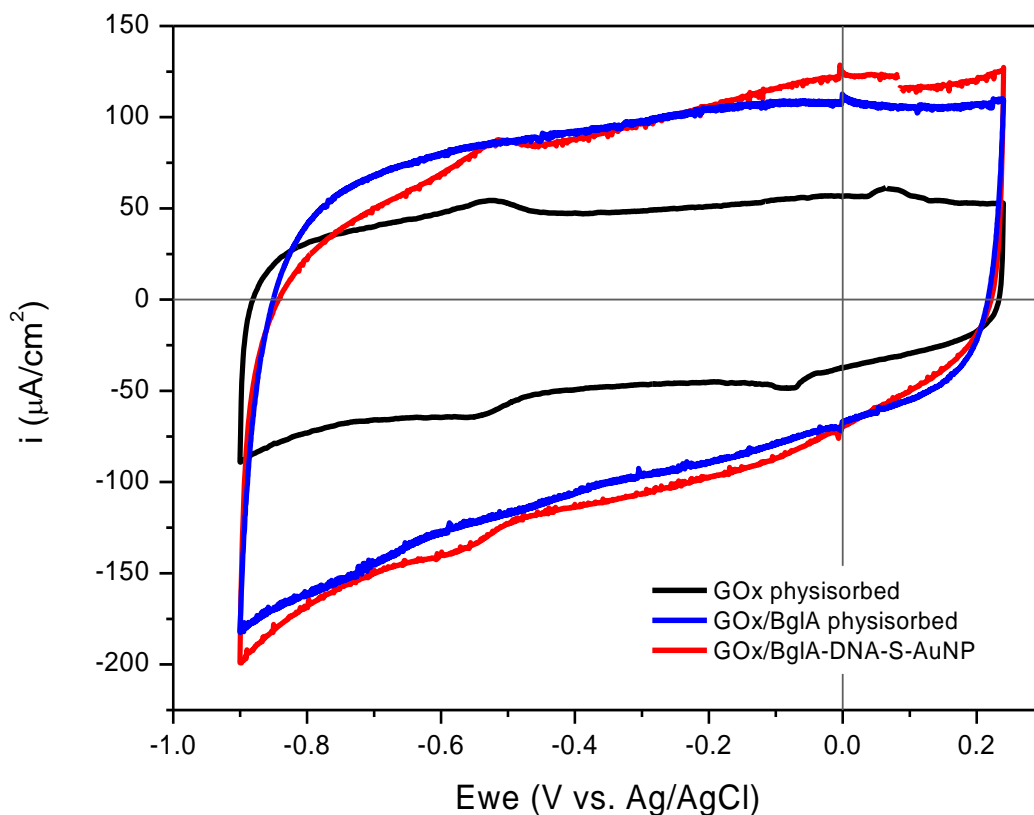


Figure 4.6 Cyclic voltammogram of electrodes with one or two enzymes immobilized by either physisorption or DNA conjugation. DNA-conjugated enzyme cascade was anchored down onto the electrode by 100-nm gold nanoparticles. CV was conducted in deaerated PBS, pH7.4, with scan rate of 50 mV/s.

The electroactivity of GOx when it was combined with a secondary enzyme (BglA) was studied with a cyclic voltammetry in deaerated PBS first. As shown in Figure 4.6, the pair of redox peaks indicative of redox of FAD cofactor at $E \sim -0.55$ V that was detected with GOx-physisorbed electrode was not visible when BglA was also physisorbed onto the surface. This, combined with an increase in voltammogram height from approximately 100 to 250 $\mu\text{A}/\text{cm}^2$, suggested that BglA not only contributed to the nonfaradaic processes as expected, but also hindered the electroactivity of GOx, possibly by being a physical barrier between GOx and electrode surface and interrupted the electron transfer. BglA is a β -

glucosidase that cleaves a dimer of glucose (cellobiose) in half to produce glucose, and thus is not considered an electroactive species. However, when these two enzymes were immobilized onto a DNA scaffold, the same redox peaks were exhibited with comparable peak heights. This was attributed to the site-specific immobilization of GOx and BglA that allowed for GOx to be placed closer to the electrode surface, as it was closest to the heaviest part of the enzyme-DNA-AuNP cluster. The electroactivity of GOx in the GOx-BglA-DNA-AuNP on the screen-printed electrode was further confirmed by the drastic increase in cathodic current in the aerated PBS as electrolyte. (Figure 4.7) A highly distinguishable peak was observed for electrode functionalized with enzyme-DNA-AuNP(100) at $E = -0.48\text{V}$, which was likely due to the oxygen reacting with the FAD cofactor. Though the redox peak pair of GOx(FAD) was not discernable in either cases, the clear difference in the electrodes' behavior in absence and presence of oxygen was a promising indication that the GOx in both enzyme cascade systems was electroactive.

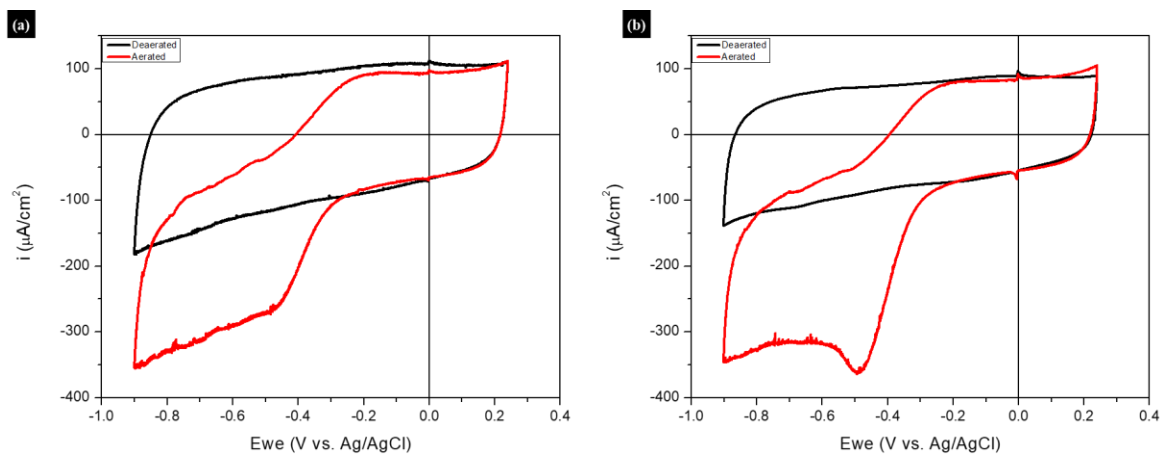


Figure 4.7 Cyclic voltammogram of electrode with GOx-BglA system immobilized by DNA conjugation in deaerated and aerated PBS, pH7.4. DNA-immobilized enzyme cascade was anchored down onto the electrode with (a) 10-nm and (b) 100-nm gold nanoparticles. CV was conducted with scan rate of 50 mV/s.

Concentration-dependent CV was carried out by adding incremental volumes of cellobiose into the aerated electrolyte. At a fixed amount of BglA and GOx, higher concentration of cellobiose would result in higher supply of glucose, which is the main substrate for GOx. As glucose reacts with the GOx cofactor, the concentration of the oxidized form of GOx (GOx(FAD)) would decrease, resulting in a reduction in the cathodic current. As shown in Figure 4.8(a) and (b), both electrodes utilizing 10- and 100-nm AuNPs as anchors for the bienzymatic cascade on DNA scaffold showed a decrease in the cathodic current as a function of cellobiose. This not only supported the glucose concentration-dependent behavior of GOx, but also indicated the cascade reaction of cellobiose hydrolysis by BglA followed by oxidation of glucose by GOx. When the degree of cathodic current reduction was plotted as a function of glucose equivalent concentration (Figure 4.8(c)), electrodes utilizing 100-nm AuNPs as anchors for the GOx-BglA cascade system only reduced in cathodic current by approximately $20 \mu\text{A}/\text{cm}^2$ at glucose equivalent concentration of 0.08 mM, while those with 10-nm AuNP anchors reduced by 40. At 1.12 mM glucose, however, a huge uptick in the cathodic current reduction was observed for 100-nm AuNP anchored samples, which could be speaking to the relatively slow cellobiose hydrolysis rate of BglA. In fact, when similar glucose concentration range was applied to DNA-immobilized GOx with AuNP anchors (open symbols in Figure 4.8(c)), cathodic current was reduced immediately upon introduction of glucose (0.1 mM). This could be attributed to the fact that the enzymatic activity of GOx was much higher than that of BglA.

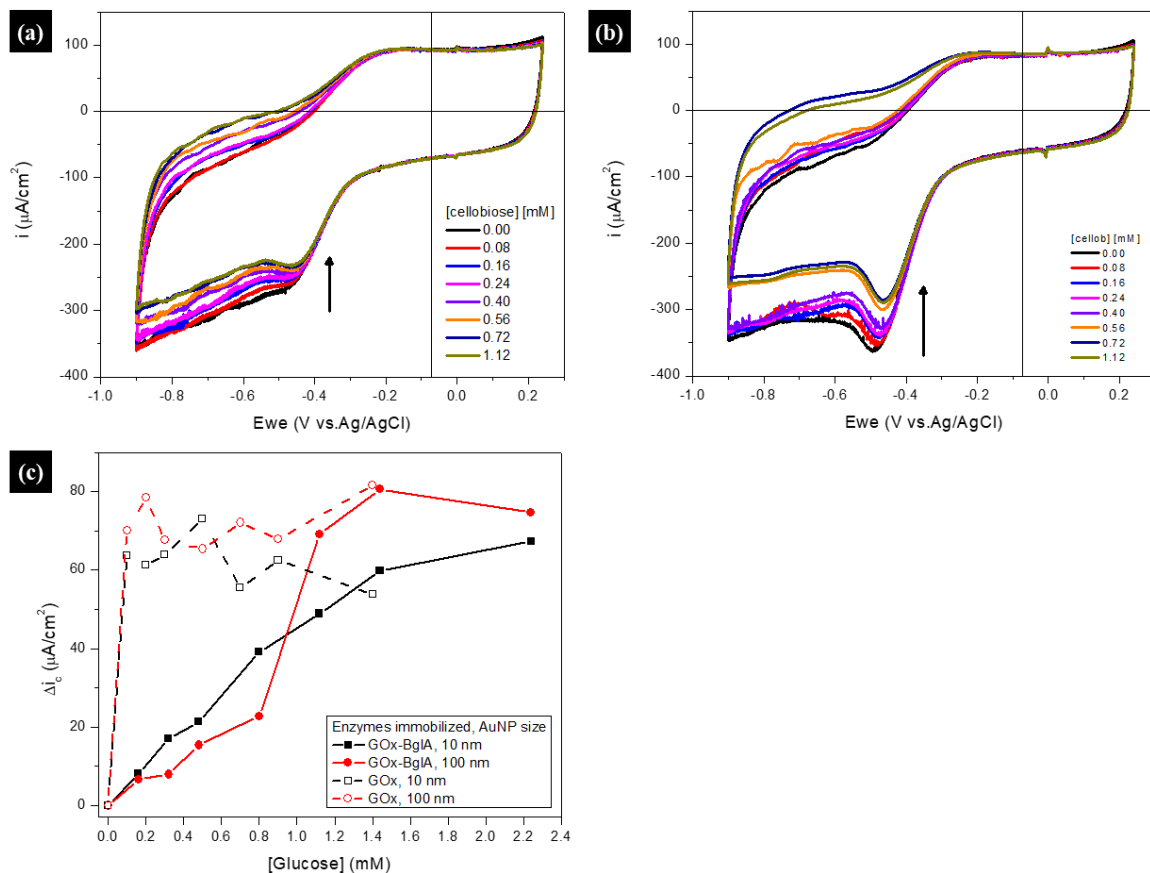


Figure 4.8 [Cellobiose]-dependent cyclic voltammogram of electrode with GOx-BglA system immobilized by DNA conjugation. DNA-immobilized enzyme cascade was anchored down onto the electrode with (a) 10-nm and (b) 100-nm gold nanoparticles. CV was conducted in aerated PBS, pH7.4, with scan rate of 50 mV/s. Arrows indicate increasing cellobiose concentration. (c) Change in cathodic current at $E = -0.7$ V as a function of glucose concentration. Electrodes functionalized with bienzyme cascade (closed symbols) were reacted with cellobiose ($[\text{glucose equiv.}] = 2 \times [\text{cellobiose}]$), while those with only GOx on DNA scaffold (open symbols) were reacted with glucose.

Glucose oxidase activity assay was utilized for a couple of purposes: (i) to rule out that cellobiose concentration-dependent behavior in CV of GOx-BglA-DNA-AuNP system was not simply due to the oxidation of trace amounts of glucose in the cellobiose solution (<1%), and (ii) to roughly compare the activity of GOx and BglA in the DNA-immobilized bienzymatic system. As shown in Figure 4.9(a), time-dependent absorbance for monitoring concentration of H₂O₂ for DNA-immobilized bienzyme cascades with either size of the AuNP anchor exhibited a comparable production rate of H₂O₂ with that for DNA-immobilized GOx with AuNP anchor up to 10 minutes (600 s), after which the production rate increased for approximately 6 minutes (up to 1000 s) before it decreased back to its initial rate for the remainder of the study. The lagged increase in H₂O₂ production rate at 10 minutes was a clear evidence that the cellobiose hydrolysis by BglA was the rate-limiting step. The specific production rate of each DNA-immobilized enzyme system reacted with cellobiose showed that DNA-immobilized bienzyme cascade exhibited twice the production rate of DNA-immobilized GOx. (Figure 4.9(b)) Thus, it was confirmed that while cellobiose solution used in this work did contain some amount of glucose for the enzymatic electrode without BglA to show some activity, the synergistic effect of immobilizing both GOx and BglA onto the DNA scaffold was evident.

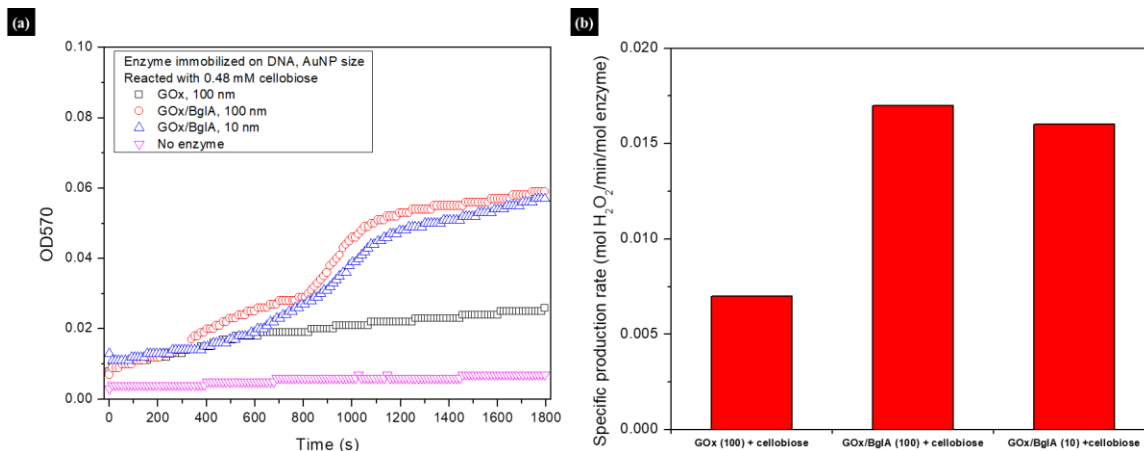


Figure 4.9 (a) Time-dependent absorbance and (b) specific production rate of GOx-BglA system immobilized by DNA conjugation over time. DNA-immobilized enzyme cascade was anchored down with 10- or 100-nm gold nanoparticles.

Stability of the DNA-immobilized bienzyme cascade with AuNP anchors was briefly studied by conducting CV under same conditions 7 days after fabrication. Each electrode had been stored at 4 °C in pH7.4 PBS without any light. Cathodic current at approximately $E = -0.7$ V, where GOx electroactivity was likely detected, decreased by 15 and 13% for 10- and 100-nm AuNP anchors, respectively. Before repeating the experiment for longer period of time, it would be difficult to determine whether or not the AuNPs were effective anchors for long-term applications.

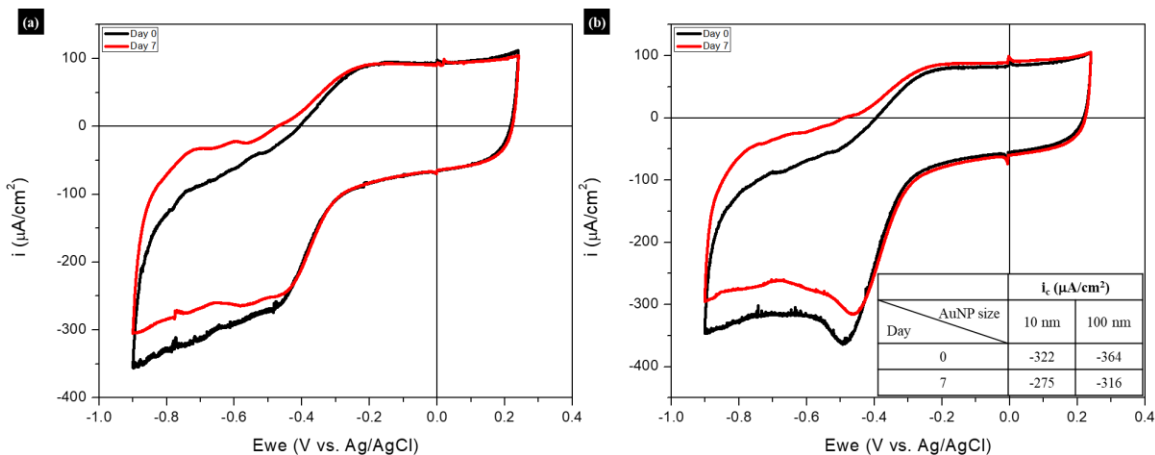


Figure 4.10 Cyclic voltammogram of electrode with GOx-BglA system immobilized by DNA conjugation over time. DNA-immobilized enzyme cascade was anchored down onto the electrode with (a) 10-nm and (b) 100-nm gold nanoparticles. CV was conducted in aerated PBS, pH7.4, with scan rate of 50 mV/s.

4.5 Conclusion

The concept of multienzyme cascade reaction was applied to enzymatic electrode fabrication. Electroactivity of GOx was first studied with a simple physisorbed electrode combined with MWNT and Nafion for facilitating electron transfer and preventing leaching, respectively. Electrode fabrication conditions such as GOx, MWNT and Nafion loading to optimize the electroactivity were systematically studied via two sets of design of experiment. As a demonstration of the multienzyme cascade system on an electrode surface, two enzymes consisting of one cellulase and one oxidoreductase were immobilized on a customized DNA template, which was covalently bound to AuNPs of various sizes as an anchor. Synergistic effect of the two enzymes organized for sequential hydrolysis followed by oxidation was confirmed by enzyme activity assay and cellobiose concentration-dependent cyclic voltammetry. With the successful implementation of the 2-enzyme system as a biocatalyst, this work could be a potential platform for electrodes

or even enzymatic fuel cells functionalized with multienzyme cascade systems, which could accommodate for much wider range of molecules to be used as fuels such as the naturally abundant cellulose.

4.6 References

1. Xu, S. & Minteer, S. D. Enzymatic Biofuel Cell for Oxidation of Glucose to CO₂. *ACS Catal.* **2**, 91–94 (2012).
2. Satomura, T. *et al.* Construction of a novel bioanode for amino acid powered fuel cells through an artificial enzyme cascade pathway. *Biotechnol. Lett.* **41**, 605–611 (2019).
3. Tasca, F. *et al.* Increasing the coulombic efficiency of glucose biofuel cell anodes by combination of redox enzymes. *Biosens. Bioelectron.* **25**, 1710–1716 (2010).
4. Sokic-Lazic, D., De Andrade, A. R. & Minteer, S. D. Utilization of enzyme cascades for complete oxidation of lactate in an enzymatic biofuel cell. in *Electrochimica Acta* vol. 56 10772–10775 (Pergamon, 2011).
5. Kim, Y. H., Campbell, E., Yu, J., Minteer, S. D. & Banta, S. Complete Oxidation of Methanol in Biobattery Devices Using a Hydrogel Created from Three Modified Dehydrogenases. *Angew. Chemie Int. Ed.* **52**, 1437–1440 (2013).
6. Zhu, Z., Kin Tam, T., Sun, F., You, C. & Percival Zhang, Y. H. A high-energy-density sugar biobattery based on a synthetic enzymatic pathway. *Nat. Commun.* **5**, 1–8 (2014).
7. Szczupak, A. *et al.* The electroosome: A surface-displayed enzymatic cascade in a biofuel cell's anode and a high-density surface-displayed biocathodic enzyme. *Nanomaterials* **7**, (2017).
8. Mazurenko, I. *et al.* Pore size effect of MgO-templated carbon on enzymatic H₂ oxidation by the hyperthermophilic hydrogenase from *Aquifex aeolicus*. *J. Electroanal. Chem.* **812**, 221–226 (2018).
9. Sugimoto, Y., Kitazumi, Y., Shirai, O. & Kano, K. Effects of mesoporous structures on direct electron transfer-Type bioelectrocatalysis: Facts and simulation on a three-dimensional model of random orientation of enzymes. *Electrochemistry* **85**, 82–87 (2017).
10. Brena, B. M. & Batista-viera, F. Immobilization of Enzymes A Literature Survey. in *Methods in Biotechnology: Immobilization of Enzymes and Cells* 15–30.
11. Chen, Q., Yu, S., Myung, N. & Chen, W. DNA-guided assembly of a five-component enzyme cascade for enhanced conversion of cellulose to gluconic acid and H₂O₂. *J. Biotechnol.* **263**, 30–35 (2017).

12. Liu, Y., Zhang, J., Cheng, Y. & Jiang, S. P. Effect of Carbon Nanotubes on Direct Electron Transfer and Electrocatalytic Activity of Immobilized Glucose Oxidase. *ACS Omega* **3**, 667–676 (2018).
13. Daraghmeh, A. *et al.* A Study of Carbon Nanofibers and Active Carbon as Symmetric Supercapacitor in Aqueous Electrolyte: A Comparative Study. *Nanoscale Res. Lett.* **12**, (2017).
14. Prabakaran, S. R. S., Vimala, R. & Zainal, Z. Nanostructured mesoporous carbon as electrodes for supercapacitors. *J. Power Sources* **161**, 730–736 (2006).

5 Summary and Perspective

This work focused on two applications of nanofibers in energy harvesting and generation: piezoelectrics and enzymatic fuel cell electrodes.

In Chapter 2, detailed study on size- and temperature dependent piezoelectric properties of polyacrylonitrile (PAN), data of which was limited in the literature possibly due to relatively low piezoelectric charge constant, was conducted for the very first time. By utilizing the effect of electrospinning, during which the high electric field induced further molecular alignment along the nanofiber, as well as controlling the dimensions and crystallinity, the piezoelectric properties of PAN nanofibers was significantly enhanced, exhibiting voltage response of up to 16 times that of literature values. In addition, design of experiment was used to elucidate the effect of operating conditions and precisely control the dimensions, morphology, and various properties of PAN-based pristine and composite nanofibers, which yielded porous carbonaceous nanofibers with high electroactive area and electrical conductivity, showing good potential as enzymatic fuel cell electrode materials.

The concept of enzymatic fuel cell with multienzyme cascade on a DNA scaffold was demonstrated with a two-enzyme system in Chapter 4. The use of gold nanoparticles as an effective anchor for the relatively large biocatalyst system was highlighted. For the fully cellulolytic enzymatic fuel cell application, up to five-enzyme assembly was developed on a DNA scaffold and its synergistic effect during sequential cellulose hydrolysis and subsequent glucose oxidation was established (Chapter 3).

Overall, the two applications studied in this work were a part of energy generation methods that potentially use renewable source of energy such as motion (i.e. vibration, kinematics, etc.) and biomass. With further optimizations ahead, the cellulolytic enzymatic fuel cell could be a device that generates electricity by consuming pre-treated cellulosic waste with power density high enough to power watches or cell phone chargers. The investigation of piezoelectric properties of polyacrylonitrile could expand the range of piezoelectric polymers to be implemented for real-life applications such as self-powered wearable sensors and devices that are typically studied with PVDF or PVDF-TrFE.

Looking ahead, material characterization of PAN-derived nanofibers would be beneficial in correlating with and explaining the change in piezoelectric properties as a function of nanofiber dimensions and crystallinity. Optimizations in the enzyme ratio of the multienzyme cascade system could account for the rate-limiting components to maximize the efficiency. The DNA scaffold could also be engineered to investigate its role on providing a stable platform onto which the enzymes are immobilized, such as increasing the number of base pairs to increase the melting point. Finally, the porous multiwalled carbon nanotube-embedded carbonaceous nanofiber could be employed as the electrode for the cellulolytic enzymatic fuel cell once assembled.